Wirelessly controlled micro- and nanostructures for bioapplications

ANDRÉ MACHADO LINDO

Tese de doutoramento em Biologia Básica e Aplicada

2015

ANDRÉ MACHADO LINDO

Wirelessly controlled micro- and nanostructures for bioapplications

Tese de Candidatura ao grau de Doutor em Biologia Básica e Aplicada submetida ao Instituto de Ciências Biomédicas Abel Salazar da Universidade do Porto.

Orientador – Prof. Dr. Bradley Nelson

Categoria – Full Professor

Afiliação – Swiss Federal Institute of Technology (ETH Zürich)

Co-orientador – Dr. Salvador Pané i Vidal

Categoria – Senior Research Scientist

Afiliação – Swiss Federal Institute of Technology (ETH Zürich)

Co-orientadora – Dra. Ana Paula Pêgo

Categoria – Investigadora Principal

Afiliação – Instituto de Ciências Biomédicas Abel Salazar da Universidade do Porto

Acknowledgements

Abstract

The first objective of this thesis was the development of a biocompatible magnetic nanocomposite with potential for various biomedical applications. Imagine a device that combines a biocompatible, mechanically and chemically stable substrate, with other materials that allow sensing and external triggering, while avoiding cells to obstruct it or an immune response to be triggered. This type of device was achieved by the development of a nanocomposite consisting of iron nanowires coated with carbon embedded in a porous alumina matrix (Fe@C NWs / AAO). Iron nanowires were obtained by template-assisted electrodeposition after producing the porous alumina templates by anodization (AAO). A high quality graphitic coating around the Fe NWs is achieved by a chemical vapor deposition (CVD) process at 900 ºC. This process also increases the mechanical and chemical resistance of the alumina by the formation of θ- and δ-Al_2O_3 crystalline phases. It was found that this nanocomposite is bioinert, non-cytotoxic and anti-biofouling to fibroblasts. The surface properties change from bioactive into bioinert by converting the porous alumina into a non-porous nanocomposite. Furthermore, the carbon coating enables biomolecules to be anchored at the surface of the nanocomposite. The multiple features of this nanocomposite make it a good candidate for applications ranging from implantable cardiac patches to on-demand collectors of residual nanoparticles. Magnetic nanocarriers were also developed using a very similar protocol, which involved doing CVD at 750 ºC with subsequent etching of the alumina template. The Fe@C NWs that were produced were functionalized with polyethylene glycol (PEG) obtaining PEG-functionalized biocompatible core-multishell magnetic Fe@C NWs (f-CMSN). This framework

allows wireless magnetic manipulation, as well as drug transportation (e.g., Doxorubicin), multimodal traceability (MRI or Raman) and the release of therapeutic drugs or hyperthermia/phototherapy can be achieved by using IR stimulation or oscillating magnetic fields. Potential biomedical applications range from targeted drug delivery to biosensing.

Imagine this time being a passenger on a tiny submarine capable of exploring a biological cell from the inside. What if you could manipulate, probe, and measure the various parts that make up a cell while the cell is still alive and functioning? What could you learn and what new knowledge could be derived? The development of biocompatible magnetic micro/nano-probes for cellular investigation was the second objective of this thesis. We report for the first time the pH sensing and rheological measurements performed inside single pollen tubes using a magnetic nanoprobe. Different micro/nano-probes were fabricated using template-assisted CoNi electrodeposition using porous alumina templates (AAO) or using 3D photolithography. The micro/nano-probes were coated either with silica using a sol-gel method or with a polymer coating (PAH:FITC-PSS) using layer-by-layer deposition (CoNi-(PAH:FITC-PSS)$_4$), rendering them functional and biocompatible. In the polymer-coated framework, FITC comes embedded in PAH allowing pH sensing to be performed. In the silica-coated framework, biomolecules (e.g., FITC) are added to the surface after silanization (CoNi-SiO$_2$-FITC). The micro/nano-probes were introduced into the pollen tubes through microinjection. Intracellular pH (pH$_i$) measurements performed in *Lilium longiflorum* (lily) pollen tubes revealed pH values between 6.5 and 8. Rheological measurements were taken with the polymer-coated nanoprobes using magnetic manipulation. The cytoplasmic streaming velocity was determined to be 11.6 ± 0.4 μm/s and the value obtained for the cytosolic viscosity was 6.0 ± 0.5 mPa·s. The developed wireless magnetic micro/nano-probes allow, virtually, the measurement of intracellular chemical and mechanical properties in a broad range of cell types other than plant cells.

Resumo

O primeiro objectivo desta dissertação foi o desenvolvimento de um nanocompósito magnético biocompatível com potencial para diversas aplicações biomédicas. Imagine-se um dispositivo que combina um substrato biocompatível, mecânica e quimicamente estável, com outros materiais que permitem detecção e activação externa, e que ao mesmo evita a sua obstrucção por células ou que uma resposta do sistema imunitário seja despoletada. Este tipo de dispositivo foi obtido através do desenvolvimento de um nanocompósito baseado em nanofios de ferro revestidos com carbono inseridos numa matriz de alumina porosa (Fe@C NWs / AAO). Os nanofios de ferro foram obtidos através electrodeposição em moldes de alumina depois de produzidos moldes porosos por anodização (AAO). Um revestimento dos nanofios com grafite de alta qualidade é atingido através de um processo de deposição química em fase de vapor (CVD) a 900 ºC. Este processo leva também a um aumento da resistência mecânica e química da alumina pela formação das fases cristalinas θ- e δ-Al_2O_3. Foi observado que este nanocompósito é bioinerte, não-citotóxico e não promove a adesão de fibroblastos. As propriedades de superfície alteram-se de bioactivo para bioinerte através da conversão de alumina porosa num nanocompósito não-poroso. Adicionalmente, o revestimento de carbono permite a imobilização de biomoléculas na superfície do nanocompósito. As múltiplas características deste nanocompósito tornam-no num bom candidato para aplicações que vão desde implantes de estimulação cardíaca até colectores *on-demand* de nanopartículas residuais. Nanovectores magnéticos foram também desenvolvidos utilizando um protocolo muito semelhante, que consistiu em realizar CVD a 750 ºC e subsequente dissolução do molde de

alumina. Através da funcionalização com polietilenoglicol (PEG), foram obtidos nanofios magnéticos biocompatíveis de Fe@C (núcleo-multicamada) funcionalizados com PEG (*f*-CMSN). Este tipo de dispositivo permite além da manipulação magnética, o transporte de drogas (e.g., Doxorubicina), a sua detecção multimodal (ressonância magnética ou Raman) e a libertação de drogas ou hipertermia/fototerapia pode ser feita através de estimulação por infravermelhos ou campos magnéticos oscilantes. Potenciais aplicações biomédicas vão desde quimioterapia localizada até biosensores.

Imagine-se agora como sendo um passageiro num pequeno submarino capaz de explorar o interior de uma célula biológica. E se pudesse manipular, sondar e medir as várias partes que compõem uma célula enquanto a célula está viva e em funcionamento? O que poderia ser aprendido e que novo conhecimento poderia daí advir? O desenvolvimento de micro/nano-sondas magnéticas biocompatíveis para investigação celular foi o segundo objectivo desta dissertação. Neste trabalho são reportados pela primeira vez a medição de pH e medições reológicas no interior de tubos de pólen usando uma nanosonda magnética. Diferentes micro/nano-sondas foram fabricadas utilizando electrodeposição de CoNi em moldes de alumina porosa (AAO) ou usando fotolitografia 3D. As micro/nano-sondas foram revestidas com silica usando um método de sol-gel ou com um revestimento polimérico (PAH:FITC-PSS) usando deposição de camada-por-camada (*layer-by-layer*), tornando-as funcionais e biocompatíveis. Nas sondas que contêm revestimento de polímero (CoNi-(PAH:FITC-PSS)$_4$), FITC está inserido no PAH permitindo a medição de pH. Nas sondas que contém revestimento de silica, biomoléculas (e.g., FITC) foram adicionadas à superfície depois de silanização (CoNi-SiO$_2$-FITC). As micro/nano-sondas foram introduzidas nos tubos de pólen através de microinjecção. Medições de pH intracelular (pH$_i$) feitas em tubos de pólen de *Lilium longiflorum* (lily) revelaram valores de pH entre 6.5 e 8. Medições reológicas foram realizadas com as nano-sondas revestidas com polímero usando manipulação magnética. A velocidade da corrente citoplasmática foi determinada como tendo o valor de 11.6 $\pm$ 0.4 μm/s e o valor obtido para a viscosidade do citosol foi de 6.0 $\pm$ 0.5 mPa·s. As micro/nano-sondas magnéticas sem fios desenvolvidas permitem, virtualmente, a medição de propriedades químicas e mecânicas intracelulares numa larga gama de tipos de células para além das células vegetais.

Table of Contents

List of Tables

List of Figures

List of Acronyms

AAO	anodic aluminum oxide
ABP	actin-binding protein
AFM	atomic force microscopy
Arabidopsis	*Arabidopsis thaliana*
CMSN	core-multishell nanowire
CNT	carbon nanotube
CSNW	core-shell nanowire
CVD	chemical vapor deposition
DI-H$_2$O	deionised water
DOX	doxorubicin
ECM	extracellular matrix
EtOH	ethanol
IPA	isopropanol
IR	infrared
ITO	indium tin oxide
FITC	fluorescein isothiocyanate
LbL	layer-by-layer
Lily	*Lilium longiflorum*
LPCVD	low-pressure chemical vapor deposition
MRI	magnetic resonance imaging
NW	nanowire
PBS	phosphate buffer solution
PED	pulsed electrodeposition

PEG	polyethylene glycol
pH$_i$	intracellular pH
PL-PEG	phospholipid- polyethylene glycol
PMEs	pectin methyl esterases
PVP	polyvinylpyrrolidone
RhoB	rhodamine B
RT	room-temperature
SEM	scanning electron microscopy
TEM	transmission electron microscopy
TEOS	tetraethyl orthosilicate
tobacco	*Nicotiana tabacum*

xx

Chapter 1

Scope of the Thesis

Nanotechnology is revolutionizing our everyday life: it is transforming many scientific domains and slowly changing the way we interact with the world.[1.1] Nanorobotics, for instance, will revolutionize medicine in the future, and it may take only a few years to become a reality.[1.2-1.6] Most of the developments in nanotechnology are still happening only in laboratories and not in industry. Nanotechnological products available in the market are so far mostly limited to some form of nanotechnology-enabled material (such as carbon nanotubes, nanocomposites, nanoparticles, etc.) or nanotechnological process (surface nanopatterning, nanocoating, etc.) that are used in manufacturing process.[1.1,1.7-1.9] Scientific works such as the one presented in this dissertation are vital for the development of future nanotechnology-based industrial applications.

The work reported in this thesis relies on the use of micro/nano-scale devices. The benefit of using such small scale devices, as opposed to macroscale devices, relies mostly on the size limitations that certain applications present. As an example, microscale devices can go through human veins and capillary vessels but only nanoscale devices can penetrate into tumor cells.[1.10-1.13] Small scale devices have several other advantages when compared to macroscale, such as a higher surface-to-volume ratio. This means that they possess higher conjugation and reactivity yields of molecular compounds on their surface (e.g., drugs, antibodies, etc.).[1.14] Nanoscale is the scale at which a lot of biology happens: proteins, antibodies, virus and DNA are all nanosized.[1.15] For instance, haemoglobin has 5.5 nm in diameter[1.16] while single-stranded DNA is only

about 2 nm in diameter.[1.17] Nanosized structures also behave in different ways as opposed to macroscale objects, for instance, displaying quantized properties (quantum size effects) and moving in different ways when immersed in fluids (low Reynolds number regime).[1.2]

The first part of the thesis is devoted to the development of biomedical applications using nanoporous alumina either as a substrate/interface or as a template/mold. Extensive literature can be found on anodic aluminum oxide (AAO) templates for nanofabrication, especially one-dimensional structures such as nanowires, nanotubes and quantum rods.[1.18] The motivation for the research presented was that oppositely, literature is lacking when it comes to the surface properties of porous alumina and about alumina as a biomaterial. In this sense, porous alumina as-produced and in the form of filled alumina nanocomposites were tested and their mechanical and surface properties are presented in this thesis. The fabrication techniques used (anodization, electrodeposition, etc.) were selected because of their low cost, ease of use, reproducibility and versatility of available materials. The combination of porous alumina with embedded core-shell magnetic materials provides the basis for several biomedical applications such as wirelessly controllable implantable devices with biosensing or drug release capabilities.

The second part of this thesis reports the acquisition of intracellular mechanical and biochemical properties of pollen tubes following the implementation of an innovative nanotechnological methodology. Plant biology has much less literature available when compared to animal biology. This gap is quite evident when we look at the field of mechanobiology. Mechanotransduction, for instance, is quite unexplored in plants. The gap between the amount of research from animal biology and plant biology is mostly due to the non-immediate implications for humans that derivate from the research on plant biology. Another reason is that the amount of tools available to plant biologists is also more limited because of the existence of a rigid cell wall which limits, for instance, the feasibility of potential transformation methods. The study of the mechanical properties of plants is important for humans for the optimization of crops as well as to find clues about mechanisms that are similar in animals (e.g., neuronal cells and pollen tubes). In this sense, this thesis explores the acquisition of biomechanical properties of plants and presents the value obtained. Several different plant

2

transformation methods were tested, from more common methods (e.g., particle bombardment) to not so common ones (e.g., microinjection). This allowed experiencing some of their advantages and disadvantages regarding the internalization of micro/nano-sized structures. Wireless magnetic micro/nano-probes were developed in order to fill the gap in plant mechanobiology of micron-sized single cells.

In chapter 2, biomedical applications of different magnetic micro/nano-structures are presented. A biocompatible magnetic nanocomposite was developed and its mechanical and chemical characterization is shown complemented with *in vitro* cytotoxicity/biocompatibility tests. The development of magnetic nanocarriers for drug delivery applications using a very similar fabrication procedure is also shown. Upscaling options were also tested and results are presented.

In chapter 3, the development and testing of two biological applications of magnetic micro/nano-probes are described, namely, intracellular pH probing and cytoplasmic nanorheology. The internalization of the micro/nano-probes using different plant transformation methods is also explored in this chapter. Biomechanical parameters were measured and calculated and their values are presented.

In chapter 4, a summary of the major contributions from this thesis is presented as well as an outlook on the future work.

The references used in each chapter are listed at the end of the corresponding chapter.

1.1 Bibliography

[1.1] G.M. Whitesides, 2005, "Nanoscience, Nanotechnology, and Chemistry", *Small*, 1(2), 172-179;

[1.2] F. Qiu and B.J. Nelson, 2015, "Magnetic Helical Micro- and Nanorobots: Toward Their Biomedical Applications", *Engineering*, 1(1), 21-26;

[1.3] M.A. Zeeshan et al., 2012, "Graphite Coating of Iron Nanowires for Nanorobotic Applications: Synthesis, Characterization and Magnetic Wireless Manipulation", *Adv. Funct. Mat.*, 23, 823–831;

[1.4] R. Saini et al., 2010, "Nanotechnology: The future medicine", *J. Cutan. Aesthet. Surg.*, 3, 32-3;

[1.5] H. Wang and M. Pumera, 2015, "Fabrication of Micro/Nanoscale Motors", *Chemical Reviews*, DOI: 10.1021/acs.chemrev.5b00047;

[1.6] A.S. Bhat, 2014, "Nanobots: The Future of Medicine", *International Journal of Engineering and Management Sciences*, 5(1), 44-49;

[1.7] T. Tsuzuki, 2009, "Commercial scale production of inorganic nanoparticles", *International Journal of Nanotechnology*, 6(5/6), 567-578;

[1.8] H. Chen et al., 2008, "Trends in nanotechnology patents", *Nature Nanotechnology*, 3, 123-125;

[1.9] F. Piccinno et al., 2012, "Industrial production quantities and uses of ten engineered nanomaterials in Europe and the world", *J. Nanopart. Res.*, 14, 1109;

[1.10] B.J. Nelson et al., 2010, "Microrobots for Minimally Invasive Medicine", *Annu. Rev. Biomed. Eng.*, 12, 55-85;

[1.11] D. Cai et al., 2005, "Highly efficient molecular delivery into mammalian cells using carbon nanotube spearing", *Nature Methods*, 2(6), 449-454;

[1.12] C. Wong et al., 2010, "Multistage nanoparticle delivery system for deep penetration into tumor tissue", *PNAS*, 108(6), 2426-2431;

[1.13] Y.H. Bae and K. Park, 2011, "Targeted drug delivery to tumors: Myths, reality and possibility", *Journal of Controlled Release*, 153, 198-205;

[1.14] C. Baker et al., 2005, "Synthesis and Antibacterial Properties of Silver Nanoparticles", *J. Nanosci. Nanotech.*, 5, 244-249;

[1.15] A. Vaseashta and D. Dimova-Malinovska, 2005, "Nanostructured and nanoscale devices, sensors and detectors", *Science and Technology of Advanced Materials*, 6, 312-318;

[1.16] H. Xu et al., 1999, "Spectroscopy of Single Hemoglobin Molecules by Surface Enhanced Raman Scattering", *Physical Review Letters*, 83(21), 4357-4360;

[1.17] H.G. Hansma et al., 1995, "Applications for Atomic Force Microscopy of DNA", Biophysical Journal, 68, 1672-1677;

[1.18] G.E.J. Poinern et al., 2011, "Progress in Nano-Engineered Anodic Aluminum Oxide Membrane Development", *Materials*, 4, 487-526.

Chapter 2

Development of magnetic biocompatible nanocomposites and nanocarriers for biomedical applications

The work from this chapter was started as a follow-up of the EU-funded project "Nano-Actuators and Nano-sensors for Medical Applications" (NANOMA). Part of this work was done in collaboration with Dr. M. Arif Zeeshan, during his doctoral studies at IRIS-MSRL, ETH Zürich. The work reported in this chapter has been published in references Lindo et al.[2.1] and Zeeshan et al.[2.2].

2.1 Introduction

Nanocomposites consisting of a matrix containing well-organized zero or one-dimensional nanostructures (nanoparticles, nanowires (NWs) or nanotubes) exhibit unique properties, which can be advantageous for several applications such as catalysis, data storage, magnetic actuation, optical sensing or biomedical implanting.[2.1,2.3,2.4] The organization of nanostructures in matrices can be accomplished by suitable chemical procedures, or by producing or incorporating particles in pre-existing templates. For example, nanoscopic one-, two-, or three-dimensional arrangements of nanoparticles can be obtained using block copolymers-based supramolecules after solvent annealing.[2.5] Nanostructures can also be programmed to occupy spaces in arrays or templates. Maxit et al. have shown a facile method to selectively arrange ceria nanoparticles in the

sheets of a polymer in a long-range ordered diblock polymer template.[2.6] Anodized aluminum oxide (AAO) templates have been also used to fabricate long-range ordered nanocomposites. Gösele and co-workers,[2.7] for instance, have fabricated flow-through nanoporous gold nanowire/AAO composite membranes. The use of AAO arrays in the production of nanocomposites is advantageous in several aspects. First, AAO templates constitute mechanically robust platforms to grow materials that otherwise exhibit brittle fracture, such as metallic foams.[2.8] AAO template nanochannels can present very high aspect ratios and wide pore-size tunability which is an outstanding feature when compared to conventional lithographic techniques.[2.9] This is of particular interest, especially when anisotropic properties are desired in the composite. AAO have higher pore density compared to its competitors, which consequently allows a higher device fabrication yield for the same area.[2.10] Furthermore, several techniques such as electrodeposition, sol-gel or capillary filling can be used to grow materials of different nature or combinations thereof in AAO channels. AAO template-assisted electrodeposition has several advantages such as low-cost, simplicity of operation, and the ability to deposit different types of materials and alloys with high aspect ratios onto different types of substrates. Electrodeposition is a fabrication method that is regarded as providing a remarkably high degree of reproducibility.[2.11]

Besides the advantage of having anodized alumina (AAO), alumina itself is regarded as a bioinert material and it is resistant to corrosion in an *in vivo* environment. It remains stable for many years, eliciting a minimal response from tissues: a feature that makes it a very good candidate for biomedical applications.[2.8,2.12] Alumina has more than 15 intermediate metastable crystallographic phases, including γ-, δ-, θ- and α-Al_2O_3 depending on the processing temperature.[2.13] AAO templates have been widely used as implantable platforms for biomedical applications such as cell-interface studies, drug delivery, immunoisolation or biosensing.[2.14-2.17] The advantage of using these membranes in biomedical devices is that they exhibit excellent chemical stability in the presence of biomolecules. Moreover, the surface of AAO can be chemically modified to change its surface polarity. This feature is particularly important, especially for devices in which cell adhesion must be enhanced, such as in cell culturing, or in which biofouling must be avoided, e.g. in sensing, drug delivery applications or anti-biocontaminants.[2.17-2.20]

6

Magnetic nanoarchitectures have been expansively investigated for their potential usage in miniaturized electronic and magnetic devices such as energy storage systems, magnetomechanical systems or memory devices.[2.21-2.23] Likewise, the possibility of wireless maneuvering magnetic nanostructures has triggered an extensive research in their use as targeted drug-delivery platforms, magnetic resonance imaging agents, hyperthermia or thermal ablation therapy.[2.24-2.26] Among all the nanostructures, nanowires (NWs) or nanorods are particularly appealing as their shape anisotropy gives rise to enhanced physical properties such as magnetic, optical or electrical. To increase their functionalities, NWs can consist of segments made of different materials, core-shell assemblies or combinations thereof.[2.27,2.28]

Another example of extensive research done on nanoarchitectures is the case of the carbon nanotubes (CNTs). CNTs are unique materials that possess several interesting characteristics such as a high mechanical strength, high electrical and thermal conductivity, high surface area and others.[2.29] Diverse biomedical applications have been developed with CNTs ranging from sensing/detection of molecular abnormalities, to composites for tissue regeneration, and as delivery and therapeutic systems.[2.30-2.32]

CNTs can't be utilized for biomedical applications when they are in the as-prepared non-functionalized form. Their use is not suitable for this kind of applications because of their inherent hydrophobicity and therefore lack of solubility in aqueous-based biological fluids. For successful biomedical applications, the surface of CNTs has to be functionalized with appropriate chemistries to render it more hydrophilic. Functionalization can be achieved by adsorption, electrostatic interaction (non-covalent) or covalent bonding of molecules on the surface of the CNT. Similar strategies can be used to load bioactive ligands and/or therapeutic drugs for targeted drug delivery.[2.33,2.34] Covalent bonding allows strong attachment of molecules with the downside of weakening the CNT structure. Typically, this is achieved by oxidation of CNTs with strong acids, which often causes serious damages in their framework structures. Another disadvantage of this functionalization method is the loss of the characteristic Raman sp^2 signature.[2.30,2.35,2.36] On the other hand, electrostatic and adsorption functionalization methods prevent the disruption of the carbon sp^2 structure, which is the source of the CNTs' high strength. Electrostatic

bonding allows, for instance, aromatic molecules (e.g., Rhodamine B and Doxorubicin) to be easily loaded onto the surface while preserving the optical properties of the CNTs.[2.34,2.37] Despite not forming a bond as strong as a covalent bond, these molecules can line up and conjugate with the CNT surface by π-π stacking. The last strategy to load molecules on the CNT surface is by adsorption. Polymers or phospholipids can be attached irreversibly on the surface of the CNTs by adsorption.[2.38] A common polymer used in the pharmaceutical industry to enhance solubility is the polyethylene-glycol (PEG). PEG is a hydrophilic surfactant that has several other advantages to make successful biomedical applications. PEG is inexpensive, FDA approved, stealth to the immune system (anti-biofouling), with few side-effects/disadvantages.[2.35] CNTs can also have PEG conjugated to enhance its water solubility. This can be achieved, for instance, through adsorption of phospholipid-polyethylene-glycol (PL-PEG). CNTs also absorb radiation efficiently in the near infrared region. By irradiating CNTs with infrared light they can be used to selectively destroy cancer cells by local heating or trigger drug release.[2.35,2.36,2.39] Moreover, solid tumors are an easy target for CNTs and nanostructures. Because of their "leaky" vasculature, tumors uptake nanostructures with diameters less than 300 nm: this is known as the enhanced permeability and retention effect (EPR effect).[2.40,2.41]

Here, we present an ordered magnetic composite consisting of core-multishell iron-carbon NWs trapped in thermally treated AAO nanochannels. These composites are produced by aluminum anodization combined with electrodeposition and posterior chemical vapor deposition (CVD). The fabrication flow is depicted in figure 2.2. These changes enable the fabrication of chemically stable magnetic nanocomposites for biomedical applications with anti-bioufouling attributes. Furthermore, the core-multishell iron-carbon NWs were explored as potential nanocarriers for targeted drug delivery.

2.1.1 Aluminum anodization

Anodization is an electrochemical oxidation process employed to increase the thickness of the oxide layer on the surface of metals / semiconductors such as

Al, Ti, Sn, Si, InP, GaAs, among others. Anodization of aluminum, partially due to its commercial significance, has become one of the most important and widespread methods used for surface modification. Anodization can provide improved surface features such as hardness, corrosion resistance, and higher wear and abrasion resistance.[2.9]

Aluminum anodization consists on the oxidation of aluminum (anode) immersed in an electrolyte by applying a defined voltage with a counter electrode (cathode), as depicted in figure 2.1. Two forms of anodic aluminum oxide exist:

(i)   "Barrier-type": obtained with neutral or basic electrolytes (pH > 5);

(ii)   "Porous-type": obtained with acidic electrolytes.

The "barrier-type" oxide is a flat, nonporous, featureless insulating aluminum oxide form. On the other hand, when Al is anodized in an acid, such as sulfuric (H_2SO_4), oxalic ($H_2C_2O_4$), or phosphoric (H_3PO_4) acids, deep pores with nearly cylindrical channels can be formed.[2.42-2.44]

The pore formation arises from a delicate balance between two processes:

(i)   Growth of aluminum oxide;

(ii)   Dissolution of aluminum oxide.
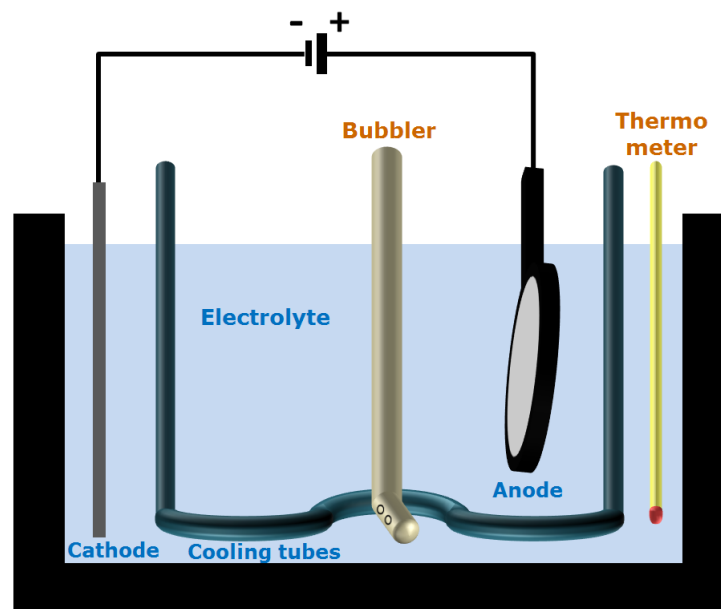
Figure 2.1 Schematics depicting an anodization setup containing a cathode (counter electrode), an anode (sample) and a suitable electrolyte. It also contains a thermometer to monitor the temperature and a bubbler to homogenize the electrolyte and distribute the cooling more uniformly.

The growth of aluminum oxide at the interface between aluminum and aluminum oxide is due to electrical field-enhanced diffusion of Al^{3+}, OH^- and O^{2-} ions. At the same time, dissolution of aluminum oxide is also occurring because of the acidic electrolyte. The pores are believed to self-order because of mechanical stress at the aluminum-alumina interface due to expansion during the anodization. This stress produces a repulsive force between the pores, causing them to arrange in a hexagonal lattice.[2.45] Depending on the anodization conditions, the obtained pores can have a diameter starting from below 10nm up to 400nm with a pore density in the range of 10^8-10^{10} pores/cm^2.[2.10]

The arrangement and shape of alumina pores are determined by the applied voltage, temperature, and also by the type and concentration of the electrolyte. The anodization voltage also controls the interpore spacing and the barrier layer thickness, and they are proportional to the voltage employed. The diameter of the pores is specifically related to the electrolyte but it can be further widened by post-anodization wet etching.[2.43] The pore shape and ordering can be significantly improved by using a two-step anodization technique.[2.46]

2.1.2 Electrodeposition
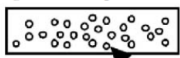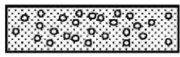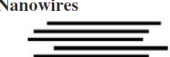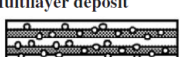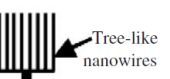
Electrochemical deposition, or electrodeposition, is an electrochemical process used for depositing a layer of a material onto another by means of electrolysis. Regarding the electrodeposition of metals (called electroplating), the cathode (working electrode) is the electrode to receive the deposit and the anode (counter electrode) is either a sacrificial anode or an inert anode (such as platinum or graphite). These electrodes are immersed in an electrolyte containing the metal salt species to be deposited through an electrical current. In the case of aqueous electrolytes, hydrolysis is also present and can affect the deposit properties due to hydrogen formation at the cathode/sample (hydrogen evolution). In electrodeposition, the amount of deposited material is directly proportional to the total charge provided. One can estimate the size of a nanostructure to be deposited by using the Faraday's laws of electrolysis.[2.47]

Electrodeposition possesses many advantages over other nanoprocessing techniques, including: (1) large number of pure metals, alloys and composite systems which can be deposited with grain sizes less than 100 nm, (2) low initial capital investment required to synthesize these materials (low technology required), (3) high yield, (4) few size and shape limitations, and (5) relatively minor "technological barriers" to overcome in transferring this technology from the research laboratory to an industrial setting.[2.11]

To produce nanocrystalline materials by electrodeposition (table 2.1), there are two main possibilities: by the addition of organic additives (such as saccharin and sodium citrate) or using pulsed electrodeposition (PED).[2.48] In PED, a cyclic current waveform (pulsating) is used instead of constant current as in direct current (DC) electrodeposition. The rest phase (current off time) allows the metal ions in the solution to be regenerated and therefore, uniform deposition conditions can be produced for each deposition pulse.[2.43] PED is especially useful for depositing materials into narrow cavities (such as in AAO), where it is very important to minimize the hydrogen evolution that can easily block the ion diffusion. Through the use of PED instead of DC plating, the deposits can be formed with improved properties like high wear resistance, corrosion resistance and hardness, low magnetic coercivity, reduced porosity, lower internal stress, lower impurity level, lower hydrogen content and better surface finish.[2.48,2.49]

Several different additives can be included in the electrolyte to modify the structure, morphology and properties of the deposit, namely: wetting agents or surfactants, grain refiners, leveling agents, etc.[2.50] In the case of iron (II) aqueous electrolytes it is common to add, for instance, ascorbic acid. Fe (II) has the tendency to be converted to Fe (III) by oxidation and to form ferric hydroxide precipitates. By adding ascorbic acid it prevents the oxidation of iron and therefore avoids precipitate formation. Another additive commonly added in iron baths is glycine, which acts not only as a pH buffer but also as a complexing agent.[2.47]

Table 2.1 Diverse nanostructured materials produced by different electrodeposition techniques.(table from Low et al.[2.51)

Methods of electrodeposition	Types of nanostructure materials			
	Nanoparticles in a metal deposit	Nanomultilayers	Nanotubes/nanowires	Nanocrystalline materials
Direct current (DC)	**Single metal deposit**	Metal type 1 e.g. Ni layer	**Nanotubes**	**Single metal**
Pulsed direct current (PDC)	Nanoparticles			
Pulsed reverse current (PRC)	**Alloy deposit**		**Nanowires**	**Alloy**
Potentiostatic (P)		Metal type 2 e.g. Cu layer		
Pulsed potentiostatic (PP)	**Multilayer deposit**		Tree-like nanowires	Fe Co

2.1.3 Chemical vapor deposition (CVD)

The three most common techniques to produce CNTs are the arc-discharge, laser-ablation and catalytic. The most popular and widely used nowadays is the chemical vapor deposition (CVD) because of its low set-up cost, high production yield (and large area), high purity and ease of scale-up.[2.52] The CVD method consists of the decomposition of hydrocarbons in the presence of a catalyst (catalytic method).[2.53] One of the most common strategies to produce CNTs by CVD is to use metallic precursors. This technique typically involves the thermal decomposition of the hydrocarbons at high temperature (also called thermal CVD). The process flow can be briefly described as follows. The sample/catalyst is placed inside the reactor on top of a support material (e.g. alumina or quartz).[2.52] The hydrocarbon is injected in the reactor with an inert gas at high temperatures and when it decomposes carbon is deposited onto the catalyst. Carbon has a low solubility in these metals at high temperatures which makes it precipitate and form nanotubes.[2.53-2.55] The most common hydrocarbons used as deposition gases are ethylene (C_2H_4), acetylene (C_2H_2) or methane (CH_4). As a catalyst, typically iron, nickel or cobalt are used. The operation temperature ranges from 500 ºC to 1000 ºC. The inert gases used are usually argon and/or nitrogen. CVD presents several advantages compared to other deposition techniques such as physical vapor deposition namely, conformal coating of surfaces, selective deposition and also the possibility of using low-temperature deposition processes (< 500 ºC).[2.55]

2.2 Materials and Methods
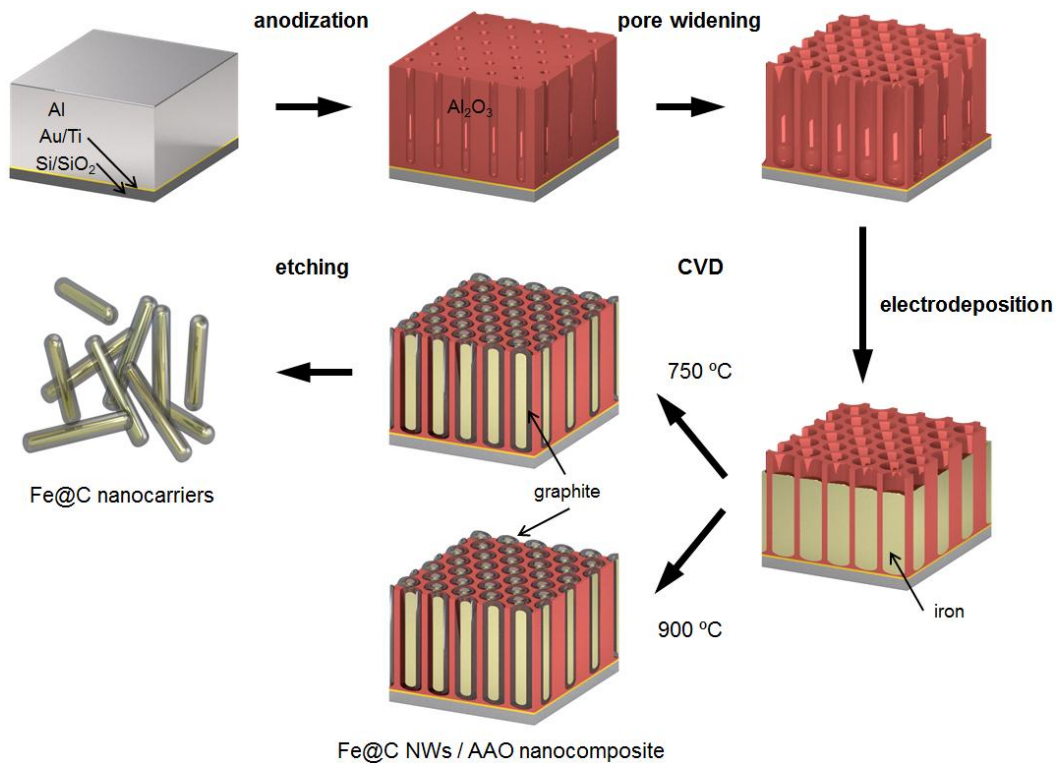
Figure 2.2 Schematics of the fabrication steps used to obtain nanocomposites or nanocarriers. A conductive layer (Au/Ti) and an Al layer are evaporated on the insulating substrate (Si/SiO$_2$). Porous AAO is obtained after anodization of the Al layer. The pore diameter is widened and the barrier layer is thinned by etching. Fe is electrodeposited into the pores of the AAO. The Fe NWs are coated conformally with carbon by CVD at 750 ºC or 900 ºC. If the CVD temperature is 900 ºC, the AAO becomes hardened and Fe@C NWs/AAO nanocomposites are obtained. If the CVD temperature is 750 ºC, the AAO can later be etched and Fe@C nanocarriers are obtained instead.(adapted from Lindo et al.[2.1])

2.2.1 Wafer preparation

Low-resistivity silicon wafers were used as rigid substrates for preparing anodizable aluminum samples. The wafers used had the following specifications: 4 inch Si wafers, crystal orientation: 111 ± 1 º, p-type, resistivity: 0.005 - 0.2 Ω·cm, single side polished, thickness: 500 ± 25 μm (Prolog Semicor LTD).

A 1.5 μm-thick layer of silicon dioxide (SiO$_2$) was deposited on the non-polished side (backside) of the Si wafers using plasma-enhanced chemical vapor deposition (PECVD 80+, Oxford Instruments). The silane precursor gas used was 2.5% SiH$_4$ in N$_2$ and the process temperature was 300 ºC. This layer will function as an insulation layer to avoid current leakage during the anodization process.

After the PECVD process the Si wafers were cleaned in order to remove contaminants. The cleaning process involved the following steps:

1. Ultrasonication in acetone, 10 min;
2. Ultrasonication in isopropanol (IPA), 10 min;
3. Ultrasonication in deionized water (DI-H$_2$O), 10 min;
4. Rinsing in DI-H$_2$O;
5. Ultrasonication in piranha solution, 10 min, H$_2$SO$_4$:H$_2$O$_2$ 3:1 ratio;
6. Rinsing in DI-H$_2$O;
7. CMOS quick dump rinse (QDR) water cleaning process;
8. Rinse drying;
9. O$_2$ plasma cleaning, 5min, 600 W.

Physical vapor deposition was done on the cleaned Si wafers using an e-beam evaporator (Univex 500, Leybold) under vacuum at a 10^{-7} Torr chamber pressure. The layers that were deposited on the Si wafers were the following:

1. Adhesion layer: Titanium,   6 nm
2. Conductive layer: Gold,   12 nm
3. Anodization layer: Aluminum,   1.5 μm

Before dicing the wafer into chips, a layer with 1.8 μm of AZ 1518 photoresist (MicroChemicals) was deposited by spin coating, to protect the substrates from dust and scratches. The wafer was diced into 1 x 1 cm chips by using a dicing saw. Prior to the anodization, the photoresist was removed by sequential ultrasonication in acetone, IPA and DI-H$_2$O for a few minutes.

2.2.2 Anodization of aluminum

Single step anodization was performed on the previously prepared substrates in order to fabricate AAO templates. The anodization setup (figs. 2.1 & 2.3) consisted of a two-electrode system using the following components:

i.	Anode:	sample (chip or wafer)
ii.	Cathode:	lead sheet
iii.	Electrolyte:	oxalic acid
iv.	Container:	polypropylene tank
v.	Cryostat:	lead tubes with ethylene glycol (F-25, Julabo)
vi.	Purging gas:	nitrogen (N_2)
vii.	Power supply:	Agilent N7977a
viii.	Graphical interface:	LabVIEW (National Instruments)
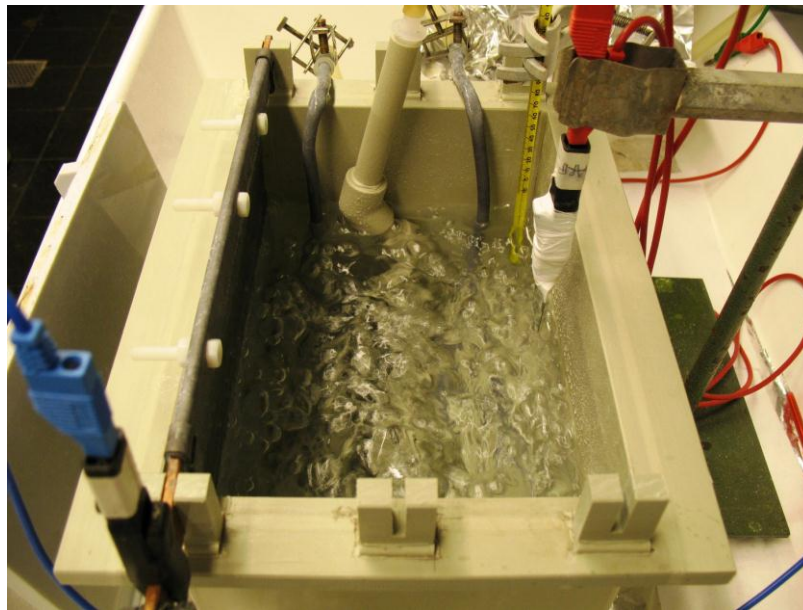
Figure 2.3 Anodization setup used consisting of a sample (anode), lead sheet (cathode), acid electrolyte bath in a container, purger/bubbler, lead cooling tubes and thermometer. The red cable is connected to the anode, and the blue cable is connected to the cathode. These cables are connected to the potentiostat which is controlled by a GUI in a computer.

The anodization conditions used for the fabrication of the nanocomposite were the following:

- Electrolyte concentration: 0.3 M
- Electrolyte temperature: 5 ºC
- Anodizing voltage: + 60 V
- Stopping current: + 200 mA

The anodization process was controlled using a LabVIEW interface. A GPIB controller allowed the connection between the LabVIEW interface and the power supply. This interface allowed precise control of the anodizing voltage and stopping current, as well as receiving and recording the measured current between the two electrodes immersed in the electrolyte. Anodization was performed at constant electrolyte temperature with continuous agitation from N_2 bubbling. The anodized chip area was 0.5 cm^2, leaving another 0.5 cm^2 to make an electrical connection to the power supply. This connection is insulated from the electrolyte by taping it with teflon tape. After anodization was completed the samples were rinsed thoroughly with DI-H_2O and blow-dried with N_2.

2.2.3 AAO pore widening

Pore widening was performed on the AAO samples using acid etching to enlarge and make the pores more uniform but also to reduce the barrier layer allowing electrodeposition to be performed. Samples were immersed in a 5.5 wt% phosphoric acid solution (Sigma-Aldrich) for 45 min while stirring in low speed at RT. Samples were washed thoroughly with DI-H_2O to remove any traces of acid and blow-dried with N_2 afterwards.

2.2.4 Iron electrodeposition

Iron electrodeposition was performed on the porous AAO samples after pore widening.

The setup used consisted of a two-electrode system containing the following elements:

i. Working electrode: sample (chip or wafer)
ii. Counter/Reference electrode: platinized titanium (10 x 10 cm)
iii. Electrolyte: iron bath
iv. Container: glass beaker
v. Purging gas: nitrogen (N_2)
vi. Stirrer: magnetic bar
vii. Potentiostat/Galvanostat: Autolab PGSTAT302N, Metrohm
viii. Graphical interface: NOVA 1.8 software, Metrohm

No wetting step was performed on the AAO samples before the electrodeposition. The composition of the iron electrolyte is listed on table 2.2. All chemicals were purchased from Sigma-Aldrich. After immersing the sample and the counter electrode in the electrolyte the current pulses applied by the galvanostat were programmed using the NOVA software. The parameters used for iron PED are listed on table 2.3. The samples were rinsed thoroughly with DI-H_2O and blow-dried with N_2 after electrodeposition.

Table 2.2 Composition of the iron bath used for electrodeposition.

Chemicals	Concentration (M)	
Iron (II) sulphate heptahydrate	0.2	
Glycine	0.1	pH buffer, complexant
Ascorbic acid	0.0028	complexant

Table 2.3 Operation parameters for iron electrodeposition.

Operating parameters	Condition
t_{ON}, t_{OFF}	8, 600 ms
Current density	-125 mA·cm^{-2}
Charge density	900 mC·cm^{-2}
Temperature	RT
Stirring speed	300 rpm
pH	4

2.2.5 Carbon coating using CVD

To grow the carbonaceous coating on the iron NWs, a low-pressure chemical vapor deposition (LPCVD) process was used. Before placing the electrodeposited samples inside the CVD chamber, the electrical connection side of the chips (non-anodized) was removed to avoid the melting of aluminum. Additionally, the CVD chamber was pre-cleaned by running an air plasma recipe. AAO templates filled with Fe NWs were placed on a heater inside a commercial CVD system (Black Magic 6", Aixtron) equipped with a showerhead gas system, which allowed a vertical laminar flow with a uniform supply of gases. The heating was provided by a heated graphite stage and the temperature was monitored with an infrared sensor. The temperature was increased at a ramp rate of 300 ºC/min under a H_2 / Ar flow of 160 and 240 sccm, respectively. The nitrogen flow was fixed at 80 sccm. The growth temperature was set between 600 ºC and 900 ºC. Before the carbon growth step, to stabilize the growth temperature and further reduce the native oxide layer, the chamber temperature was stabilized at the growth temperature for 5 min. The growth is achieved by then adding a flow of 4 sccm acetylene (C_2H_2) for 5 min. The total gas pressure was 3.31 mbar and the partial pressure of C_2H_2 was 0.028 mbar. The partial pressure ratio of C_2H_2 to H_2 was maintained at 1:40. After growth, the CVD chamber was cooled by quenching in an Ar environment and samples were removed when the temperature was below 400 ºC. The CVD process steps are schematized on table 2.4.

Table 2.4 Carbon coating CVD procedure used. (gas flows are shown in sccm)

Process gases	Phase	Heating	Stabilization / Fe reduction	Deposition	Quenching		
Heater purging	N$_2$	80	80	80	-	-	-
Reducing gas	H$_2$	160	160	160	-	-	-
Inert gas	Ar	240	240	240	2000	4000	8000
Deposition gas	C$_2$H$_2$	-	-	4	-	-	-
Temperature		RT $\rightarrow$	Growth temperature		$\rightarrow$ 400 ºC		

2.2.6 Wet etching of AAO templates

To dissolve the AAO and recover the coated and uncoated Fe NWs the sample was immersed in a 10 wt% solution of sodium hydroxide at 80 ºC for 5 minutes. The samples were afterwards immersed in EtOH to clean the NaOH and avoid reprecipitation of alumina. To obtain NW solutions, ultrasonication at 40 kHz was done in EtOH for 30 minutes with posterior collection into an eppendorf. The NWs were cleaned by separating them with a magnet, and the ethanol from the solution was replaced 5 times.

2.2.7 Sample structural characterization

The thickness of the SiO$_2$ insulation layer deposited by PECVD was characterized by ellipsometry (SE850, SENTECH Instruments). The thickness of

the Al layer was in turn characterized using a surface profilometer (Dektak XT Advanced, Bruker). The morphology of the samples both single NWs and nanocomposites was characterized using a scanning electron microscope (ULTRA 55, Zeiss). The pore diameter distribution was measured using ImageJ. The graphitic coating was observed at 100 kV with a transmission electron microscope (CM12, Philips) by dispersing the NW suspension on a 400-mesh copper grid with an ultrathin carbon layer on a holey carbon support film (Ted Pella Inc.). Raman spectra of the graphitic coating was obtained at room temperature (RT) using a WITec CRM 200 spectrometer equipped with a 532 nm green laser. Cross-sections of the nanocomposite were prepared using a focused ion beam (FIB) with a milling current of 700 pA and imaged by SEM (NVision 40, Zeiss). XRD was carried out on a Philips X'Pert diffractometer using Cu Kα radiation, with 0.03º step size and 10 s holding time. Magnetic hysteresis loops were obtained at room temperature by applying a maximum magnetic field of 1 T on C-coated and uncoated Fe NWs embedded in AAO templates using a vibrating sample magnetometer (VSM 1.2, Oxford Instruments). The wettability of the nanocomposites' surface was assessed by the static sessile drop technique using a drop shape analyzer KRÜSS DSA 100. The contact angle of 5 μL drops of Dulbecco's modified eagle medium supplemented with 10 % fetal bovine serum (DMEM) deposited onto the surface was measured at room temperature.

2.2.8 Drug loading on CMSNs

CMSNs were functionalized with amine terminated polyethylene glycol by dissolving 1 mg of PL-PEG5000-amine (NOF Corporation) in 5 mL of DI-H$_2$O (1:5 mass ratio) into a 20 mL glass scintillation vial. The vial was sonicated in a water bath ultrasonicator for 1 h at room temperature. Water from the bath was changed periodically to avoid overheating. The obtained CMSN suspension was centrifuged at 14.5 krpm for 3 h at room temperature and the supernatant solution was then collected. The PL-PEG functionalized CMSN (f-CMSN) suspension was placed into a 0.5 mL-Amicon centrifugal filter device (Merck Millipore) with a molecular weight cutoff (MWCO) of 100 kDa. The solution was centrifuged at 14.5 krpm for 10 min at room temperature. The excess of PL-PEG in suspension was removed

by successive washing and centrifugation cycles. Afterwards, 0.5 mL of the *ƒ*-CMSN solution was mixed with 30 μL of a 1 mM Rhodamine B solution and 50 μL of DI-H$_2$O. The mixture was stored at 4 °C for 24 h. The excess RhoB was then removed using the centrifugal filter device with subsequent washing / resuspension in DI-H$_2$O, for at least 10 cycles. After intensive filtration the RhoB conjugated *ƒ*-CMSNs were finally resuspended in 0.5 mL DI-H$_2$O. Absorption and emission were recorded using a UV-VIS-NIR spectrometer (TECAN Infinite M 200). The same conjugation procedure was used for Doxorubicin using a 10 mM DOX solution. For the control experiments, samples containing only dye or drug were applied the same filtration / washing procedure.

2.2.9 Cytotoxicity and biocompatibility nanocomposite tests

3T3 fibroblasts (ATCC) were cultured in Dulbecco's minimal essential medium supplemented with 10 % fetal bovine serum (DMEM) and 1 % penicillin / streptomycin with 10 % CO$_2$ at 37 °C. The Fe@C NWs/AAO nanocomposites were washed by multiple immersions in EtOH and DI-H$_2$O and subsequently sterilized with UV light.

To evaluate the cytotoxicity, samples were submerged in culture medium in a 12-well plate. After 24 hours of incubation, the gel-conditioned medium was transferred to the cultured cells. Cells seeded in fresh media were used as a control. After incubation for 48 h, WST-1 reagent (Roche) was added to each well according to the manufacturer's instructions. Three hours later, 50 μL of each solution was transferred into a 96-well plate, and the absorbance was measured at 435 nm. Ten parallel experiments were performed for every sample. Absorbance values were obtained using a UV-VIS-NIR spectrometer.

To assess the biocompatibility of the samples, the materials were tested for cell adhesion and proliferation. Cells were cultured on top of the samples for 48 hours in culture medium. Cell density and morphology were visually characterized from images taken with an inverted fluorescence microscope (IX 81, Olympus). For electron microscopy imaging purposes, the samples that showed cell proliferation were first immersed in 4% paraformaldehyde in phosphate buffer solution (PBS) for chemical fixation during 1 h. The fixed cells were then rinsed

with fresh PBS and gradually dehydrated by immersing the sample in 10%, 25%, 50%, 75%, 90% and 100% EtOH, and each step maintained during 5 minutes. Next, the samples were dried by critical point drying (CPD 030, Bal-Tec) and a thin film of platinum (about 10 nm) was sputtered onto the sample as a conductive layer before SEM inspection (Zeiss ULTRA 55).

2.3 Results and Discussion

2.3.1 Upscaling of fabrication procedure

A common problem in micro/nano-fabrication processes is the time demand. Typically, micro/nano-fabrication involves multistep processes and their successful completion requires both skill and precise control of several equipments and parameters, to the extent that, in some cases, several days are needed to produce a functional working sample. To develop a successful industrial application the time demand and the product working volume/quantity have to be optimized. The same applies to develop a biomedical application such as a drug delivery carrier: a sufficiently large amount of a working sample is needed to withstand multistep preparation processes that typically involve product losses, such as filtration, separation, among others.

The micro/nano-fabrication protocol described in this chapter requires around one week (5 days) to obtain a working sample, from wafer preparation to carbon CVD coating. The previously used working samples consisted in 0.5 cm by 1 cm chips (0.5 cm^2 area). This chip size is suitable for testing new parameters but not suitable for an industrial or biomedical application. Using this chip size, the weight of carbon-coated iron nanowires obtained was less than 0.2 mg per chip.

The starting point for the micro/nano-fabrication protocol described in this chapter is the 4-inch wafer preparation. Therefore, we tried to upscale the process from a 0.5 cm^2 chip working area to use the total anodizable area of the 4-inch wafer (~60 cm^2). The followed procedure was to anodize the whole 4-inch wafer using a wafer holder, instead of dicing it in several chips. For these experiments a graphite counter electrode (cathode) was used. The sample conditions that were tested are listed in table 2.5.

The current measured during anodization showed a normal evolution (fig. 2.4) and a cross-sectional analysis of the samples did not reveal any abnormal pore formation (fig. 2.5). However, from these experiments it was not possible to obtain any uniformly anodized 4-inch wafer. This was confirmed by further iron electrodeposition on the anodized wafers. Only certain areas had iron successfully electrodeposited, and this was visible to the naked eye from having different areas with different colors (fig. 2.6). The nanowires grown on the successful electrodeposited areas showed normal size and morphology.
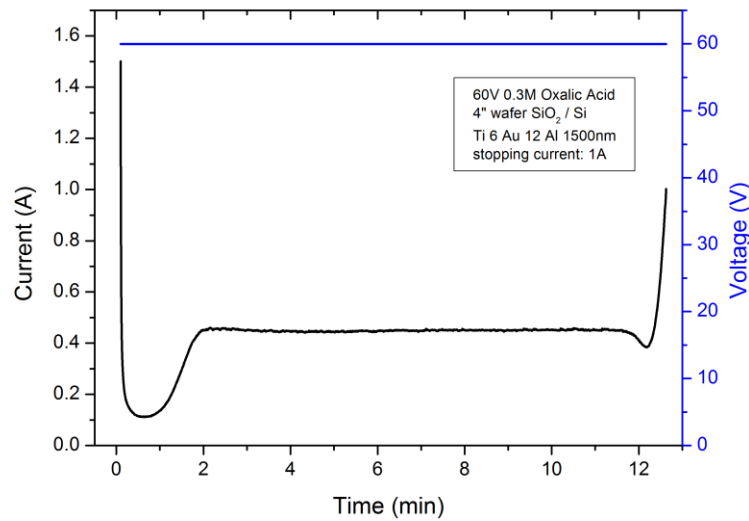
Figure 2.4 Plot of the current evolution (in black) measured for anodization at 60 V of a 4-inch wafer keeping a constant temperature of 5 ⁰C. The voltage applied is plotted in blue.

Table 2.5 List of anodization conditions tested using 4-inch wafers

Anodizing voltage	Temperature	SiO$_2$ insulation layer	Other
60 V	0 º C, 5 ⁰C	Yes	-
40 V	0 ⁰C, 5 ⁰C	Yes	-
60 V, 40 V	5 ⁰C	No	copper tape contacting the whole backside

The first hypothesis that we thought of, regarding this upscaling problem, was the fact that the wafer holder used does not allow the wafer to cool down from the backside during the anodization process. A major difference between the chip

and wafer anodization is that the chip is cooled more efficiently because it is fully immersed in the cold electrolyte. Whereas the wafer holder does not allow the wafer to contact the electrolyte on the backside and even has an air gap which decreases the thermal conductivity. In order to minimize this potential problem we tried to decrease the electrolyte temperature and also to reduce the anodizing voltage, which should help decreasing the wafer temperature (table 2.5). These experiments did not improve the anodization results.

a)   b)
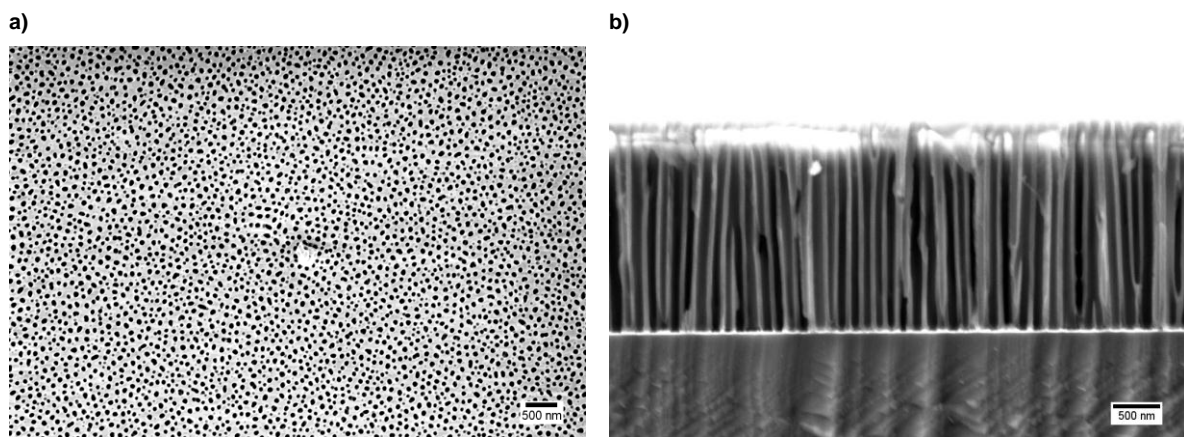
Figure 2.5 SEM images of the AAO template after anodization (60 V, 5 ⁰C) and pore widening. a) Top view and b) cross-sectional view.(adapted from Lindo et al.[2.1])

Supporting the first hypothesis, indeed precise control of the electrolyte temperature is crucial for a homogeneous pore growth.[2.42] If there is not an efficient heat transfer out of the wafer this can lead to local heating at the bottom of the pores. This local heating can cause an inhomogeneous electric field distribution at the bottom which can lead to cracks, plastic deformations or unordered pore distribution of the AAO film.[2.56]

The second hypothesis to this issue was that inhomogeneities in the aluminum evaporation and / or inefficient electrical connection to the wafer could be causing a non-uniform current distribution. To minimize this possible source of problems, first we removed the SiO_2 insulation layer on the backside. This insulation layer was not necessary for wafer anodization because only in chip anodization the chip is fully immersed in the electrolyte. Second, we used copper tape distributed along the whole wafer backside to make an electrical connection (table 2.5). The wafer holder has just three electrical connection points to the

wafer, and so with this last test we aimed to distribute the current more uniformly along each point of the wafer.One fact that supports our second hypothesis is that it is common for aluminum foil anodization either to include an electropolishing or an annealing step prior to the anodization, which is absent from our protocol. Electropolishing is claimed to be required for aluminum surface flattening and to promote uniform pore distribution.[2.45] The annealing step is referred to enhance the grain size in the aluminum and to contribute to homogeneous pore growth over large areas. [2.45] Still, at this point the impossibility of homogeneous anodization of our 4-inch wafers was not fully understood by us. Nevertheless, difficulties in upscaling the anodization process to larger sizes have been reported in literature.[2.56]
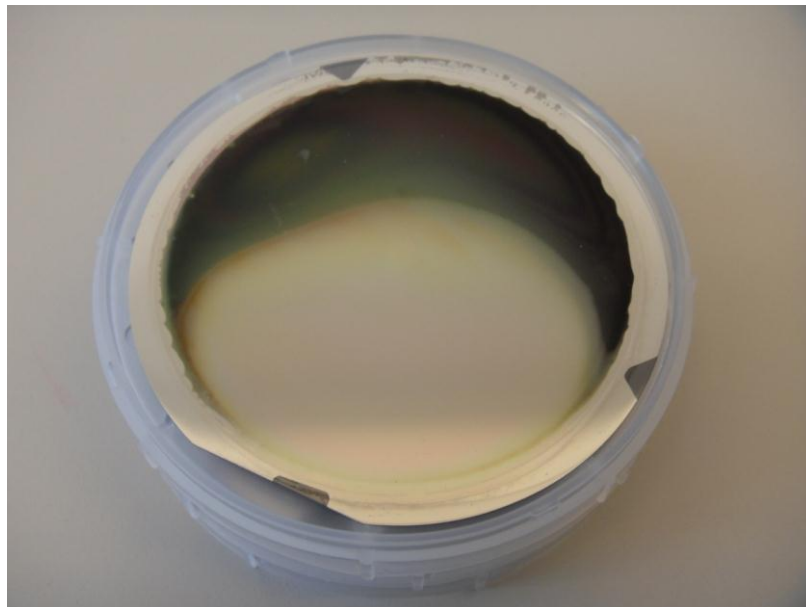
Figure 2.6 Picture of a 4-inch wafer after anodization and iron electrodeposition. It is visible two areas with different colors denoting non-uniform anodization: the dark one contains iron nanowires whereas the light one does not.

Going back to chip anodization we have found out that we could still upscale the fabrication process by 8 times. 2 by 2 cm chips were the highest chip dimensions exhibiting good anodization uniformity (fig. 2.7). For this chip size, the weight of carbon-coated iron nanowires obtained after etching was around 1 mg per chip.
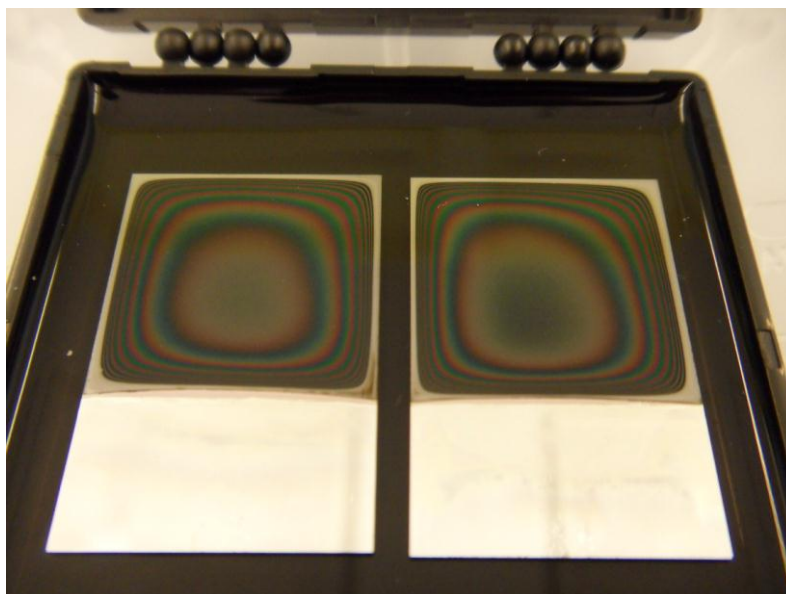
Figure 2.7 Two sample chips after anodization and iron electrodeposition processes. The anodized part (upper part) is the one displaying colors (2 x 2 cm), while the rest of the chip (lower part) was used for the electrical connection (1 x 2 cm).

2.3.2 Magnetic nanocarriers for drug delivery

Magnetic nanocarriers for wireless targeted drug delivery were fabricated combining protocols from Zeeshan et al.[2.2] and Zhuang et al.[2.35] The fabricated devices (fig. 2.11) consist of four different components, listed on table 2.6.

Table 2.6 Component list from the magnetic nanocarriers.

Component	Material	Method
Core	Iron	electrodeposition
Multishell	Graphite	CVD
Surfactant	PL-PEG-NH$_2$	adsorption
Drug loading	Doxorubicin (and Rhodamine B)	π-π stacking

The iron core was grown by template-assisted electrodeposition using the widened porous AAO as templates. The iron bath was kept with constant N_2 purging because of the iron's fast oxidation which was noticeable at the end of the day by the bath color change. Therefore, a new bath was prepared every day to avoid the formation of Fe(III). The obtained iron nanowires before CVD had a diameter around 77 ± 6 nm (fig. 2.8a)).

a)

b)
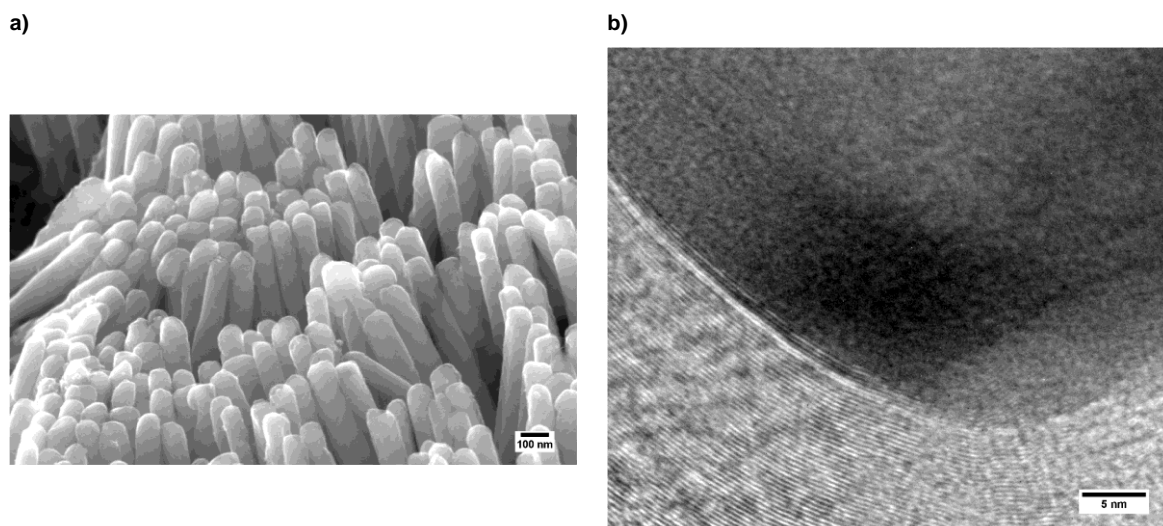
Figure 2.8 a) SEM and b) HRTEM pictures displaying the Fe@C CMSNs. In b), it is clearly visible the iron core (darker color) and the graphitic multishell structure around it.(adapted from Lindo et al.[2.1])

The samples were washed and blown with N_2 before placing them inside the CVD chamber to minimize contaminations. The CVD chamber was also plasma cleaned every 2-3 runs to remove amorphous carbon accumulation. A carbon coating was grown around the iron nanowires (core) by LPCVD at 750 ºC. After etching the AAO, the nanowires can be recovered magnetically in solution. The carbon layer is visible under TEM, displaying a lighter color than the core, and also displaying multiple shells (fig. 2.8b)). The observation of shells denotes the formation of high quality graphitic carbon (crystalline). The obtained core-multishell nanowires (CMSNs) have a length of around 1 μm with a diameter of 86 ± 25 nm.

To be able to measure the concentration of CMSNs after the functionalization/conjugation experiments, a calibration was made using the absorbance of the CMSN by UV-VIS-NIR spectroscopy before

functionalization/conjugation (fig. 2.9). The UV-VIS-NIR absorption spectra were obtained from CMSN solutions in DI-H_2O with different concentrations (100, 50, 10, 5 and 1 mg/L).
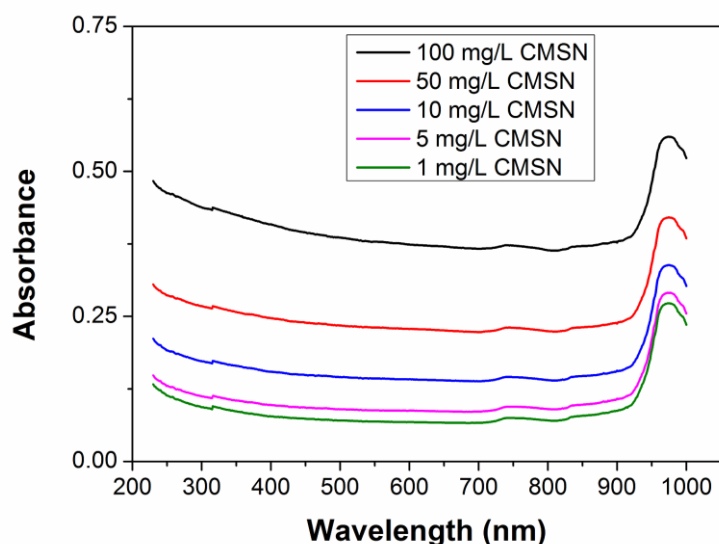
Figure 2.9 Calibration plot of the absorption of CMSNs in solution at different concentrations before functionalization/conjugation. A linear relationship was obtained for the absorption measured at 743, 803 and 808 nm using this data.

The mass extinction coefficient of the CMSN was determined using the Beer-Lambert law:

$$A = \varepsilon \cdot c \cdot l$$ (equation 2.1)

A - absorbance

ε - mass extinction coefficient ($mL \cdot mg^{-1} \cdot cm^{-1}$)

c - concentration ($mg \cdot mL^{-1}$)

l - optical path length (cm)

The absorbance data points used to make the calculations were in a location of the spectra that has a characteristic carbon absorption signature that is not located near the absorption peaks of the dye or drug used for conjugation (fig. 2.10) namely, 743, 803 and 808 nm.[2.35] The value obtained for the mass extinction coefficient of the CMSN was 2.175 ± 0.015 mL·mg^{-1}·cm^{-1}.

The CMSNs were first functionalized with PL-PEG-NH$_2$ to make them water-soluble. After functionalization, the excess PEG was removed from the supernatant, and then the ƒ-CMSNs were conjugated with Rhodamine B. Again a filtration procedure was applied to remove excess unbound RhoB from the supernatant, which consists on doing filtration and washing with DI-H$_2$O at least than 10 times. After being resuspended in DI-H$_2$O, at the end of this procedure the RhoB conjugated ƒ-CMSNs (ƒ-CMSN-RhoB) still exhibited a slight pink color, while the RhoB control turned transparent. The same procedures were used to obtain Doxorubicin conjugated ƒ-CMSNs (ƒ-CMSN-DOX), which displayed a slight brownish red color at the end of the filtration procedure.

Loading of RhoB and DOX was confirmed from the UV-VIS-NIR absorption spectra (fig. 2.10a) and c)) where it is possible to see the emergence of prominent absorption "signature" peaks at 554 and 490 nm, respectively, after conjugation, while the respective controls retained no significant absorbance. The absorption "signatures" were retained in the dye / drug conjugated ƒ-CMSN samples after intensive filtration. To determine the dye / drug loading concentration, a calibration was done using the absorption spectra of different dye / drug concentrations. Using Beer-Lambert's law (eq. 2.1), it was possible to calculate the loading concentrations from the subtraction of the ƒ-CMSN-RhoB and ƒ-CMSN-DOX spectra with the ƒ-CMSN absorption spectrum. For a final concentration of around 50 mg/L ƒ-CMSN (determined by the previous calibration), the calculated RhoB loading achieved was in the order of 10^{-5} M and the DOX loading was around 10^{-6} M.

The emission spectra were acquired as a complementary confirmation of the attachment of the dye/drug, given that they both emit fluorescence (fig. 2.10b) and d)). It is possible to see that, even though the controls show almost no absorption, their emission still shows some fluorescent intensity. Interestingly, it is possible to see that for DOX (fig. 2.10 c) and d)), the fluorescent intensity from the DOX control is close to the intensity of the ƒ-CMSN-DOX even though the difference in their absorption is quite pronounced. There is a decrease in fluorescent intensity happening due to quenching of the DOX when bound to the graphitic coating. This has been reported in literature for other aromatic molecules such as RhoB.[2.57] The detection of quenching is a second proof that the Doxorubicin was indeed attached to the surface of the ƒ-CMSNs.
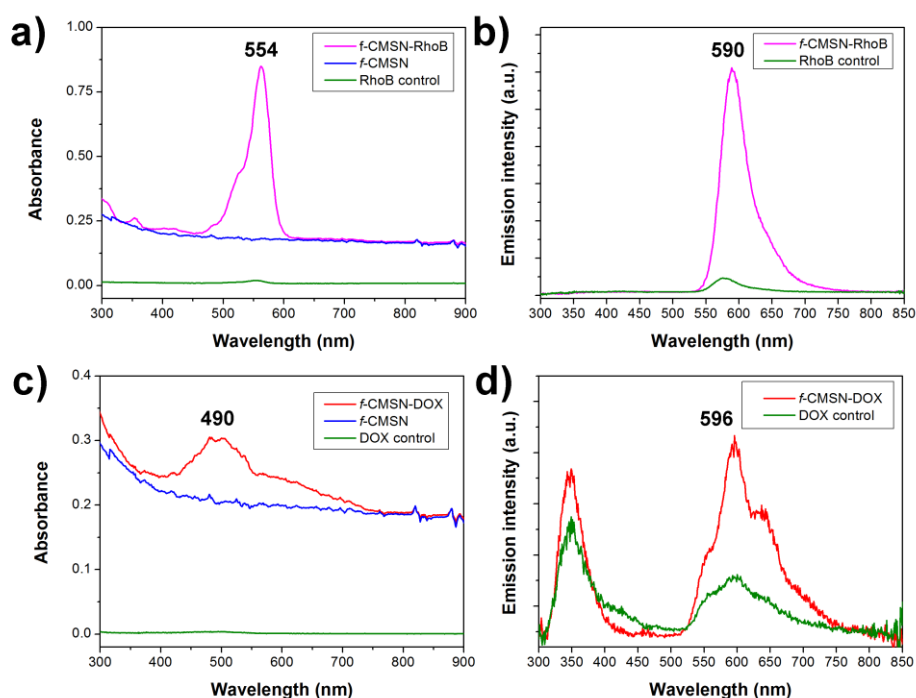
Figure 2.10 Absorption and emission spectra of a), b) Rhodamine B and c), d) Doxorubicin conjugated ƒ-CMSNs. The spectra of the respective ƒ-CMSN and RhoB / DOX controls are also shown. All the spectra were subtracted with the DI-H$_2$O spectrum. The wavelength of each peak of interest is highlighted.

The developed nanostructure (ƒ-CMSN) presents the possibility of using it as a vehicle for wirelessly controllable targeted delivery. A schematic of the developed framework is depicted in figure 2.11. It has a ferromagnetic core consisting of iron that is controllable using magnetic fields. Its high quality graphitic coating (sp^2 hybridized) allows the loading onto the surface of aromatic compounds, such as Rhodamine B, Doxorubicin or even DNA and other oligonucleotides[2.58,2.59], through non-covalent π-π stacking. The carbon coating also provides a rigid and stable protection against the degradation of the magnetic core, or against the release of toxic metal ions.[2.30] The PEG chain provides the necessary water solubility to avoid agglomerations of this framework and to make it biocompatible, for instance, to circulate in the blood stream. The developed framework also provides *in vitro* and *in vivo* tracking multimodality: the iron core can be traced by magnetic resonance imaging (MRI)[2.60], and the carbon coating is active in Raman. Because the diameter of ƒ-CMSN is below 100

nm, penetration into leaky tumor cells is enhanced through the EPR effect.[2.40] Given the high optical absorbance of the graphitic carbon, the release of therapeutic drugs or hyperthermia/phototherapy can be induced by using IR stimulation.[2.36,2.39] Similar release / therapy effects can be achieved through the use of oscillating magnetic fields.[2.61] Additionally, this framework provides further conjugation through the NH_2 PL-PEG termination of a plethora of other biomolecules such as ligands (peptides, antibodies) for cell recognition, radioactive labels, etc., to enhance other biomedical functionalities.[2.35]
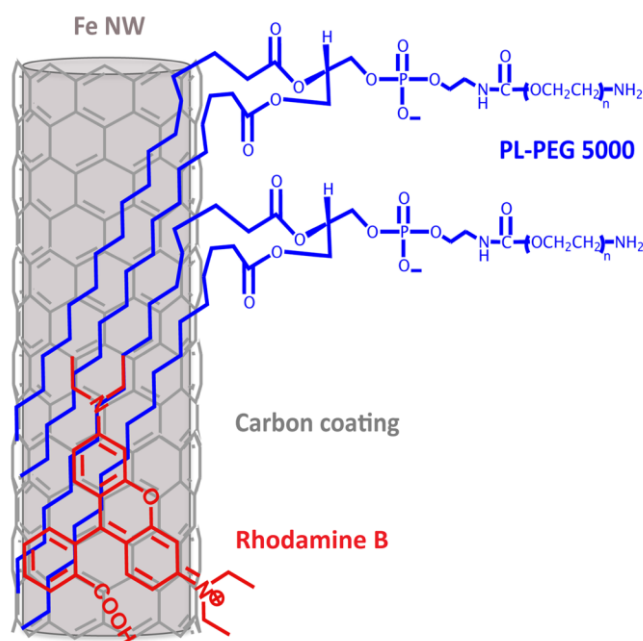
Figure 2.11 Schematics depicting the structure of the Rhodamine B conjugated f-CSMN. The PL-PEG-NH_2 is adsorbed on the surface of the CSMN and enhances water solubility. The Rhodamine B is attached by π-π stacking onto the carbon aromatic rings, in a similar way to what happens with Doxorubicin.(from Zeeshan et al.[2.2)

The magnetic properties, Raman modes and the quality of the carbon coating from the CMSNs are further investigated in the next sub-chapter (2.3.3).

2.3.3 Biocompatible magnetic AAO nanocomposite

A magnetic AAO nanocomposite was developed using the process depicted in the schematics of figure 2.2.[2.1] The nancomposite consists of AAO as a rigid

substrate with embedded Fe@C NWs produced at 900 °C as the nanocomposite filler. The AAO template used for the fabrication of the nanocomposite was shown in figure 2.5. The thickness of the template after the phosphoric acid treatment was 1.67 ± 0.14 μm. Figure 2.8 b) shows a HRTEM image of the obtained carbon-coated Fe NWs after the AAO template removal. This picture shows that by performing CVD at 750 °C a conformal carbon coating with crystalline graphene layers is achieved. The carbon coating was further optimized by varying the CVD carbon growth temperature in the range of 600 to 800 °C.[2.2,2.62] The runs were conducted with an interval of 50 °C. A low pressure CVD system was used to maintain a total pressure around 3.31 mbar for all the runs. To evaluate the quality of the carbon coating that was synthesized at different CVD temperatures, Raman spectra were acquired using a green laser. Figure 2.12a), shows the Raman spectra of the graphite coated Fe NWs after the CVD process. These spectra were recorded after dissolving the AAO template. The resolved G band shows that using the CVD at temperatures from 600 °C to 800 °C it was possible to grow graphitic carbon on the Fe NWs. The position of this G band (~1580 cm^{-1}) is a signature of sp^2 carbon hybridization which confirms the formation of graphene layers. Alongside with the G band there is also the D band present in our samples (fig. 2.12a)). The D band is common in CVD-grown graphene and is due to structural defects such as the formation of amorphous carbon or sp^3 hybridized carbon. Typically, the I_D / I_G ratio from the intensity of these two peaks is used as a measure of the carbon structural quality.[2.37,2.63] By comparing the G band with the D band, we can observe that increasing the CVD carbon growth temperature as the effect of decreasing the number of defects (fig. 2.12a)). Additional information about the structural quality and number of graphene layers can be extracted from the second order harmonic G' band (or 2D). The G' band intensity increases with the CVD temperature, which suggests an increase in the number of layers and again a higher quality of the graphene structure around the Fe NWs. Similar Raman behaviour is detected in multiwalled carbon nanotubes (MWCNTs) when increasing the number of layers.[2.63,2.64] Low defect graphene layers were achieved at 750 °C or higher temperature. The results from both D and G' bands agree in that the highest quality graphitic coating was achieved at 800 °C.
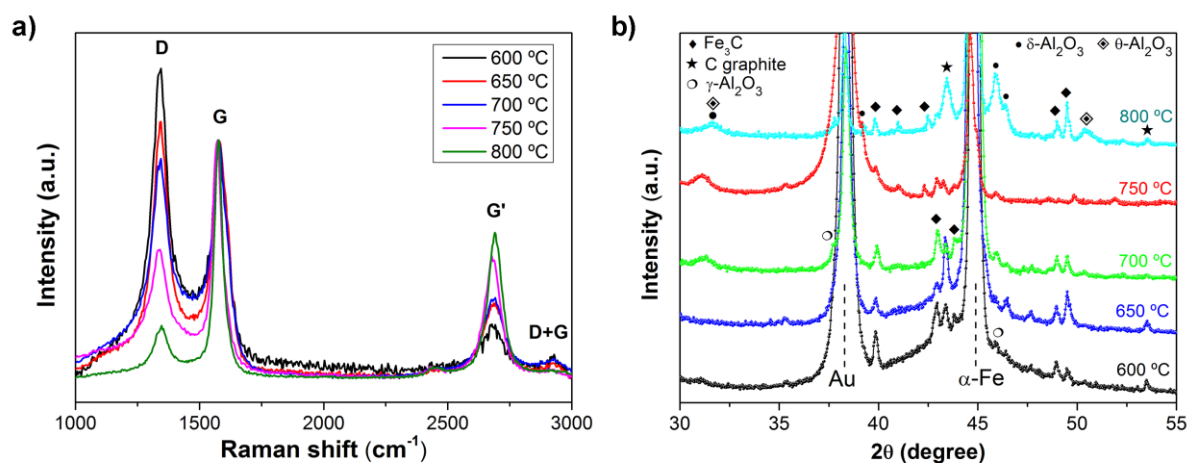
Figure 2.12 a) Raman spectra of carbon coated Fe NWs that were produced using different CVD temperatures. The intensities were normalized using the 1st order vibration harmonics (G band) as reference. The 1st order vibrational modes were found at 1344 cm^{-1} (D band) and at 1576 cm^{-1} (G band). The 2nd order vibrational modes (overtones) were found around 2689 cm^{-1} (G' band) and around 2929 cm^{-1} (D+G band). b) Zoomed detail in the 30-55º 2θ region of the XRD patterns of carbon coated Fe NWs at different CVD temperatures. The main diffraction peaks belonging to iron and alumina phases are highlighted, as well as the other detected materials.(from Lindo et al.[2.1])

The increase in carbon quality with temperature is also confirmed from XRD (figs. 2.12b) and 2.15a)) that shows decreased Fe$_3$C formation at higher temperatures (peak around 45º). The XRD patterns of Fe NWs embedded in AAO and coated with carbon by CVD at temperatures ranging from 600 ºC to 800 ºC are displayed in figure 2.12b). The patterns show the presence of α-Fe, C graphite, and some reflections attributed to the cementite phase (Fe$_3$C), suggesting that carbon diffuses into the body-centered cubic (bcc) structure of Fe to some extent, as observed in other works.[2.65] The presence of hexagonal graphite is clear at 800 ºC. Besides these phases, other peaks related to the crystallization of amorphous AAO template are detected. Namely, several phases, including γ-, θ- and δ-Al$_2$O$_3$ are detected upon increasing the CVD temperature.[2.13,2.66,2.67] Interestingly, it was noticed that at 800 ºC the AAO template starts to be difficult to etch with a solution of 10 wt% NaOH. This can be explained by the transition of alumina to the more stable θ- and δ-Al$_2$O$_3$ phases, as shown in figure 2.12b). Concerning the magnetic properties, the normalized room-temperature hysteresis

loops of nanocomposites filled with C-coated Fe NWs at different CVD temperatures are shown in figure 2.13.
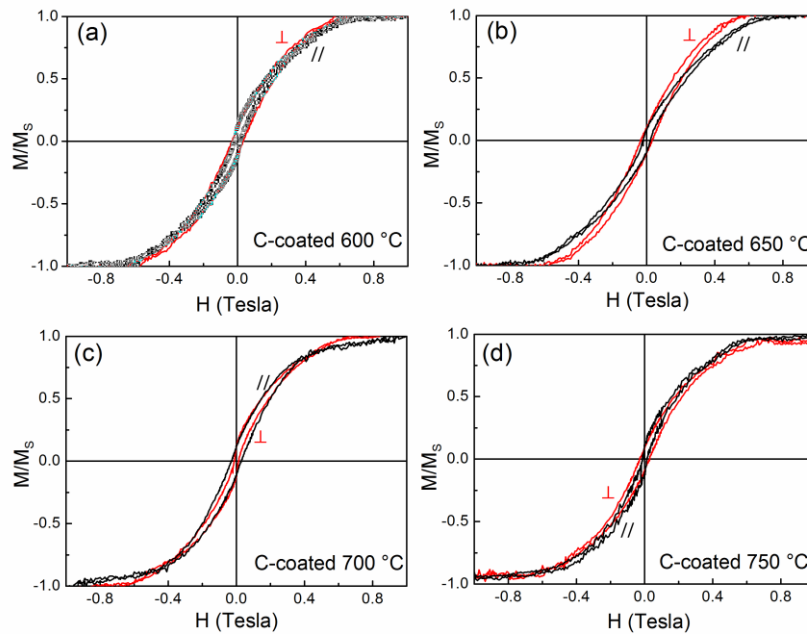
Figure 2.13 Normalized room-temperature hysteresis loops of Fe@C by using different CVD temperatures: (a) 600 ºC, (b) 650 ºC, (c) 700 ºC and (d) 750 ºC. Symbol || means that the field was applied parallel to the NWs axis whereas ⊥ means that the field was applied perpendicular to the NWs axis.(from Lindo et al.[2.1])

When the NWs are CVD-treated an inner shell of magnetic Fe_3C is formed. In this case, the overall shape of the loops does not drastically change, in spite of the expected reduction of saturation magnetization (figs. 2.13 and 2.15b)). A soft-magnetic behaviour with coercivity, H_C, values ranging from 95 to 320 Oe depending on the direction of measurement (along or perpendicular to the NWs axis) and CVD temperature, was encountered. No clear effective magnetic easy axis is observed. This is due to the competition between the magnetic shape anisotropy and the interwire dipolar interactions, as observed in other works.[2.2,2.67]

During the synthesis of the nanocomposites, the AAO templates become more resistant to chemical etching with increasing temperature. Taking advantage of this phenomenon, magnetic nanocomposites were developed at a higher CVD temperature (900 ºC). The nanocomposites were fabricated in 2 x 2 cm chips

which have the potential for faster fabrication of multiple devices. The quality of the graphitic multishell structure in the nanocomposite was not evaluated by Raman given that the Al_2O_3 from the nanocomposite was not chemically etchable. SEM images from the nanocomposite after attempting etching are shown in figure 2.14. A list of all the etchants tested is provided in table 2.7, which was combined with tip sonication. The Al_2O_3 showed a remarkable chemical resistance to both strong acids and bases and a high mechanical resistance to high power tip sonication.
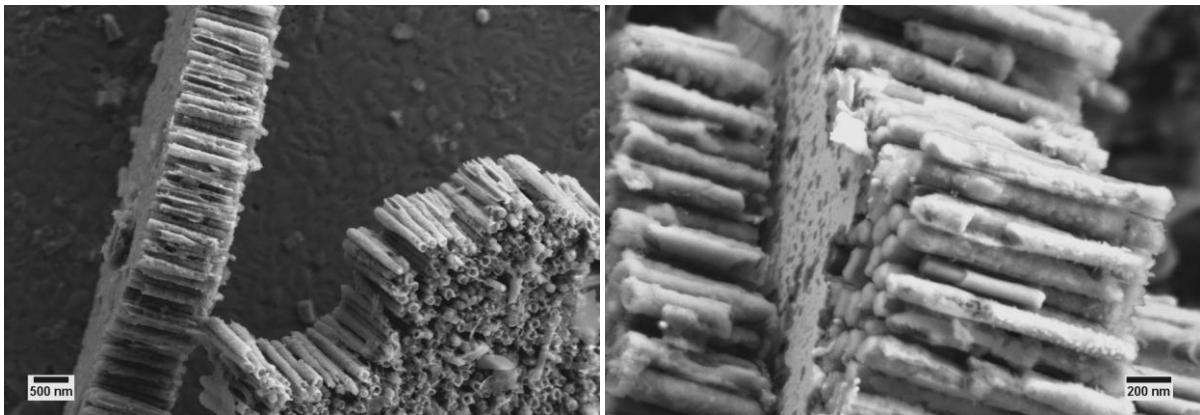
Figure 2.14 SEM images of the remaining AAO template after attempting its dissolution using the etchants listed on table 2.7 combined with high power tip sonication.

Table 2.7 List of etchants tested to dissolve the AAO from the nanocomposite.

Chemical	Temperature
10 M NaOH	80 ºC
0.5% HF (wt%)	RT
1.8% H_2CrO_4 + 6% H3PO4 (wt%)	65 ºC
Gold etchant, Nickel compatible	RT
+ tip sonication	

The structural composition of the nanocomposites was analysed by XRD. From figure 2.15a), we observe that the phases present at 900 ºC are similar to those observed at 800 ºC (figure 2.12b)). The relative intensity of θ- and δ-Al_2O_3

phases are slightly higher, which explains the increase in both chemical resistance and mechanical strength of the nanocomposite.[2.68,2.69] In addition, the pattern shows the presence of Fe_3C and C graphite phases, which are absent in the uncoated Fe NWs annealed at 900 ºC. Moreover, Fe oxides / hydroxides are detected in the latter, which further prove that the C coating protects the Fe core from intermixing between Fe and AAO template (i.e., oxygen diffusion).
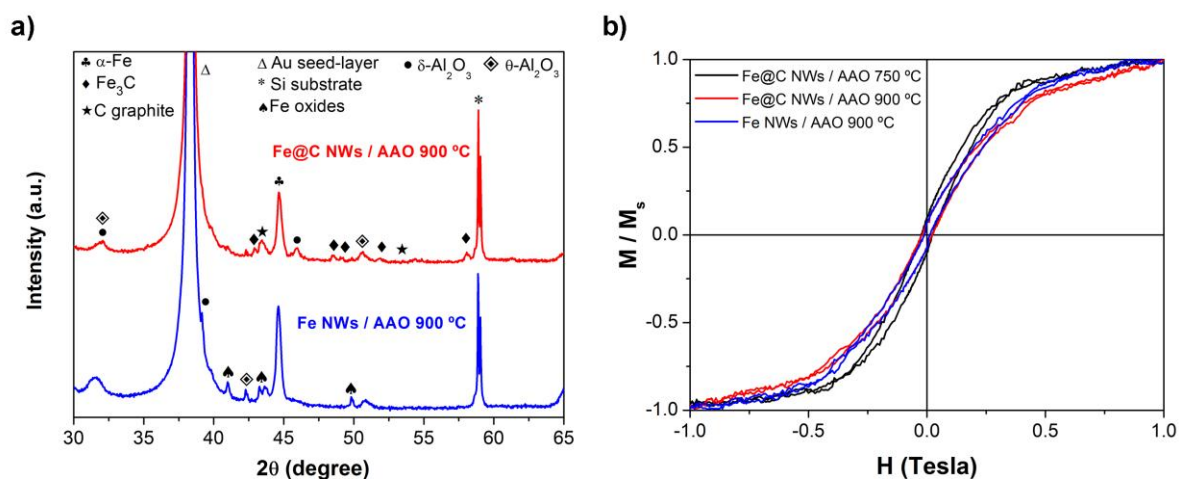
Figure 2.15 a) Comparison of XRD spectra from as-produced nanocomposites filled with uncoated Fe NWs annealed at 900 ºC and C-coated Fe NWs fabricated at 900 ºC. b) Normalized room-temperature hysteresis loops of nanocomposites filled with uncoated Fe NWs annealed at 900 ºC and C-coated Fe NWs at 750 ºC and 900 ºC. (adapted from Lindo et al.[2.1])

Further tests were done to characterize the surface properties of the nanocomposite in order to evaluate its suitability for biomedical applications. The surface wettability of our samples was determined by the sessile drop method. The contact angle of drops of culture medium on the surface were measured for different fabrication conditions and listed in table 2.8. Nanocomposites bearing uncoated Fe NWs (room temperature and annealed at 900 ºC) and others bearing carbon coated Fe NWs (750 ºC and 900 ºC), all displayed hydrophobic behavior as opposed to the unfilled nanocomposites. C-coated samples showed higher contact angles, which corresponds to a higher hydrophobicity. The C-coated samples grown at 750 ºC can be considered on the transition to the superhydrophobic regime (>150 º). In general, the increase in temperature led to a

decrease of the hydrophobic behavior. As an example, two images of some of the measured drops are shown in figure 2.16.

a)

b)
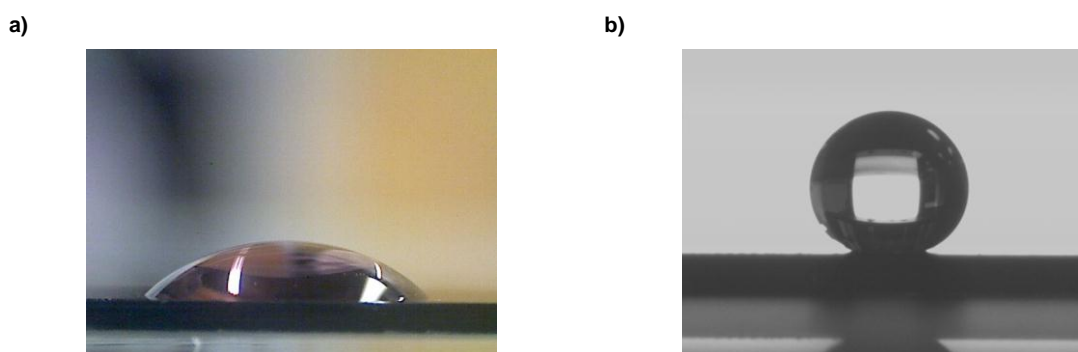
Figure 2.16 Images from DMEM culture medium drops used to measure the wettability of the nanocomposite's surface. a) AAO widened RT and b) Fe@C NWs / AAO 750 °C.

Table 2.8 List of the measured surface contact angles obtained with different nanocomposite fillers.

Sample	Young-Laplace	Standard Method
AAO non-widened RT	-	52.1 ± 0.4 º
AAO widened RT	-	46.8 ± 0.1 º
Fe NWs / AAO RT	104.7 ± 1.5 º	100.4 ± 1.0 º
Fe NWs / AAO 900 ºC	94.6 ± 1.6 º	92.4 ± 0.3 º
Fe@C NWs / AAO 750 ºC	160.7 ± 2.4 º	143.5 ± 1.9 º
Fe@C NWs / AAO 900 ºC	114.7 ± 5.2 º	111.1 ± 3.0 º

Cytotoxicity tests were performed using the WST-1 cell proliferation assay kit. Fibroblasts showed confluence with normal cell morphology after being exposed to culture medium that was incubated with nanocomposites containing either carbon coated or uncoated Fe NWs fabricated at 900 ºC (cf. Materials and Methods). The absorbance measurements showed equal levels of cell proliferation (fig. 2.17a)) which confirms that toxic ions were not released from the nanocomposite samples at significant levels. Figure 2.17b) shows fibroblast confluence in culture medium that was in contact previously with nanocomposites. This result shows that the nanocomposite is non-cytotoxic. For the case of the

carbon-containing nanocomposite, the carbon coating additionally protects the iron from corrosion over time.[2.30]
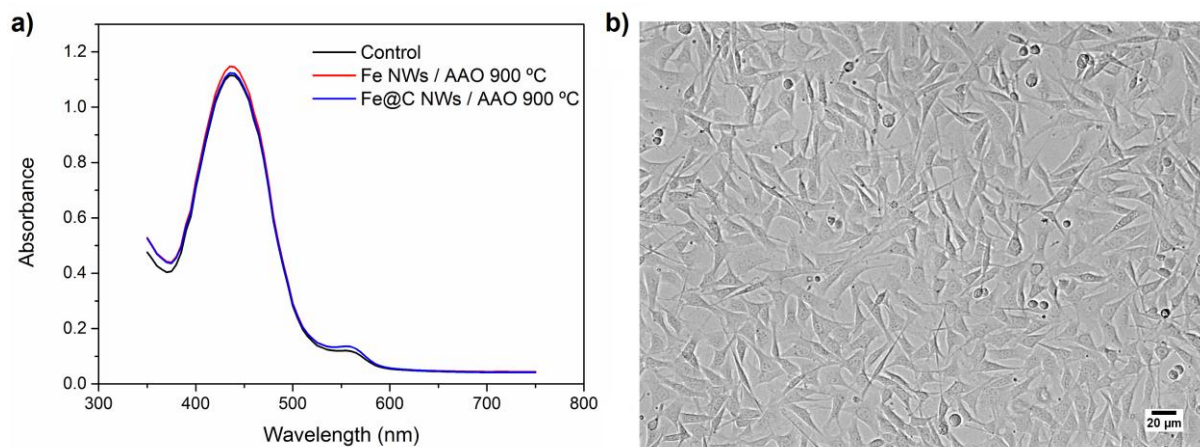
Figure 2.17 Results from the cytotoxicity test. a) Absorption spectra obtained from the WST-1 test for cells incubated in culture medium that was previously in contact with nanocomposites filled with uncoated Fe NWs and with C-coated Fe NWs at 900 ºC. b) Fibroblast confluence in culture medium that was incubated previously with different AAO templates.(from Lindo et al.[2.1]

Nanocomposite samples were also evaluated in terms of cell adhesion and proliferation on the samples' surface after different fabrication steps. Cell adhesion and proliferation was observed only on unfilled AAO templates (fig. 2.19). As listed in table 2.9, from the unfilled AAO only the widened AAO without any heat treatment (RT) did not show any cell proliferation. This is not fully understood by us because: first, before widening cells proliferate; second, the widened samples after heat treatment (750 ºC and 900 ºC) also display cell proliferation. This means that phosphoric acid etching is changing the AAO surface properties, such as adding phosphate groups[2.15], but any surface modification is being suppressed by the heat treatment. Our experiments show that porous alumina, amorphous and crystalline (heat-treated), is a bioactive material.[2.15,2.70] On the other hand, cells did not proliferate on the nanocomposite containing both carbon coated and uncoated Fe NWs fabricated at 750 ºC and 900 ºC. Furthermore, no cells were found on the surface of the filled nanocomposites but still they were proliferating on the well plate around these samples (fig. 2.18). These results indicate that cells did not adhere to the nanocomposite's surface due to the lack of anchoring points on the nanocomposite and not from cytotoxicity, which is in agreement with the

results from the cytotoxicity tests. This also shows that the filled nanocomposites (non-porous) are anti-biofouling to fibroblasts.
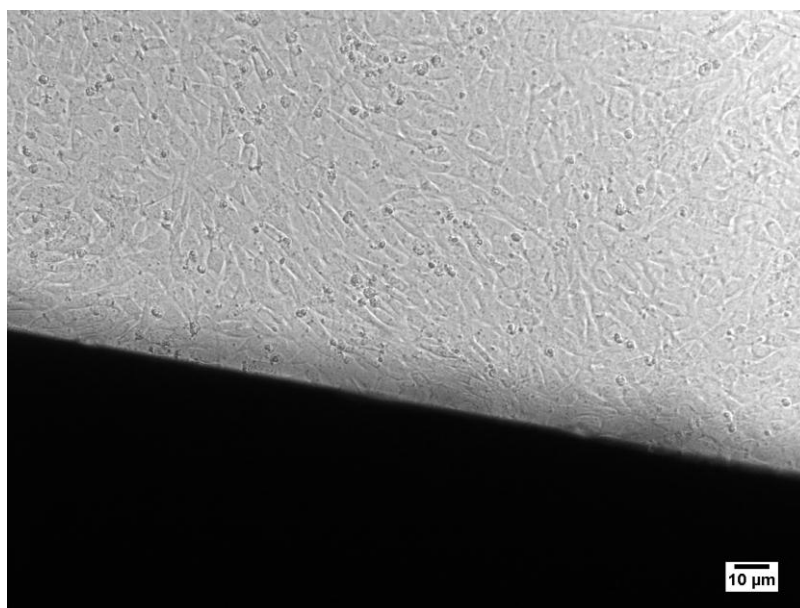
Figure 2.18 Cell biocompatibility/proliferation assay using the Fe@C NWs / AAO 900 ºC nanocomposite. Cell proliferation was observed outside of the nanocomposite (bottom of the well plate) but not on its surface. In this bright-field picture it is visible the interface between the nanocomposite (dark) and the bottom of the well plate where cells proliferate. This confirms again that even though the nanocomposites' surface doesn't allow cell proliferation, the nanocomposites do not show any toxic effect to fibroblasts. Supporting this conclusion there is also the fact that no dead cells were found on the nanocomposites' surface. (from Lindo et al.[2.1])

Table 2.9 List of AAO samples analyzed for cell proliferation.

Substrate	Filler	Temperature	Pore Widening	Cell proliferation
AAO	None	RT	No	Yes
			Yes	No
		750 ºC		Yes
		900 ºC		Yes
	Fe NWs	RT	Yes	No
		750 ºC		
		900 ºC		
	Fe@C NWs	750 ºC	Yes	No
		900 ºC		

Some modifications can be suggested to improve features of the developed nanocomposite. Two-step anodization can be done to improve the spatial distribution and uniformity of the nanocomposite filler.[2.46] Increasing the CVD temperature to 1000 °C or slightly higher improves the graphitic shell quality but, also the chemical resistance and mechanical strength of Al$_2$O$_3$ would be improved.[2.13] Decreasing the pore diameter increases the magnetic shape anisotropy of the nanocomposite magnetic filler.[2.67] Nevertheless, the developed nanocomposite showed to possess structural, chemical and magnetic properties suitable for biomedical applications.
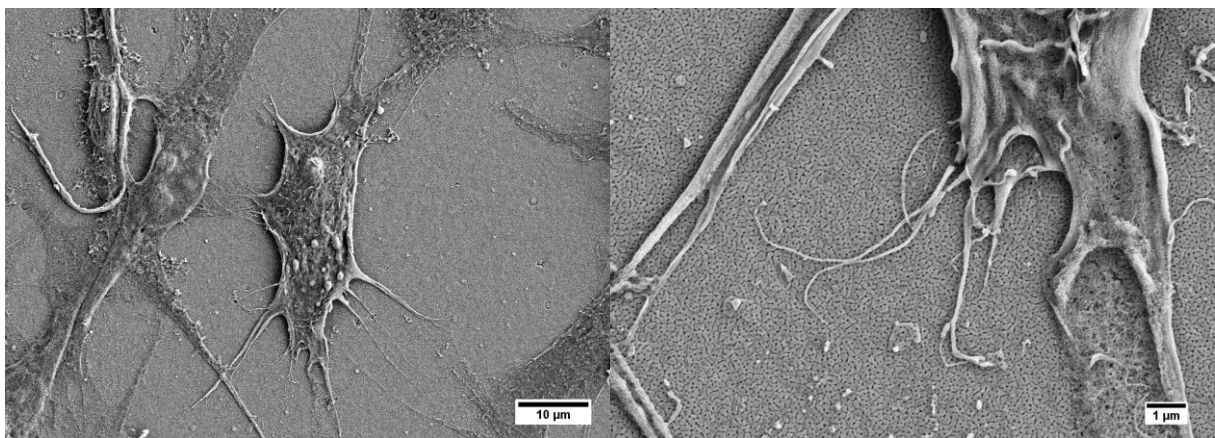
Figure 2.19 SEM images of fibroblasts proliferating on the surface of an AAO template without pore widening at room temperature. On the picture on the right, it is possible to see the pore openings from the AAO. Cells display normal morphology with visible filopodia.(adapted from Lindo et al.[2.1])

Porous alumina anodized in oxalic acid has been reported as being hydrophilic in several studies.[2.71-2.73] Our results indicate that porous alumina is hydrophilic and bioactive to fibroblasts but once the pores are filled with Fe@C NWs the nanocomposite becomes hydrophobic and does not promote fibroblast proliferation. There is a compromise between surface wettability and porosity regarding the biological properties of the nanocomposite surface: hydrophilicity and porosity promote fibroblast growth, whereas hydrophobicity and lack of porosity enhance anti-biofouling. Hydrophobicity can be a desirable feature in some biomedical events, especially for certain implants where the attachment of cells (biofouling) would damage their structure or obstruct their action/functioning. For this purpose it is important to elicit a minimal response from the tissues and

40

from the immune system. Magnetic implants with similar features have been widely employed in reconstructive surgery, dentistry[2.74], and also as micro/nano-robotic platforms for biomedical applications.[2.75] For the case where the transition to superhydrophobicity was achieved (embedded Fe@C NWs at 750 ⁰C), this feature can be used to enhance the surface with properties such as: self-cleaning, reduced viscous drag when subject to fluid flows, or once again improved prevention of surface fouling.[2.73,2.76]
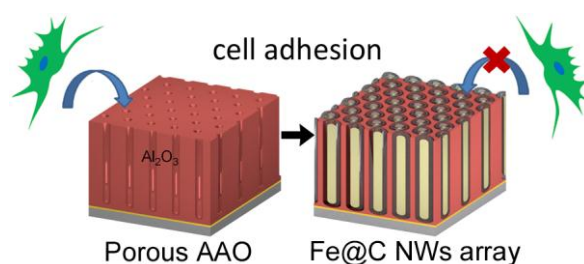
Figure 2.20 Schematics depicting the surface properties of the magnetic nanocomposites regarding cell adhesion. Cell adhesion and proliferation is only observed in unfilled porous AAO templates. Porous unfilled AAO is bioactive while the obtained Fe@C NW-filled AAO nanocomposite is bioinert and anti-biofouling.(from Lindo et al.[2.1])

2.4 Conclusions

We have demonstrated that PEG-functionalized core-multishell magnetic Fe@C NWs can be fabricated as a drug delivery carrier of therapeutic drugs such as Doxorubicin. This framework can be fabricated making use of anodization and electrodeposition which are low cost fabrication methods. The developed carrier possesses a ferromagnetic iron core covered by a high quality (sp^2 hybridized) graphitic coating. This structure not only allows wireless magnetic manipulation but also enables it to be traceable through the use of MRI or Raman (multimodality). The release of therapeutic drugs or hyperthermia/phototherapy can be achieved by using IR stimulation or oscillating magnetic fields. Furthermore, the PEG moiety provides biocompatibility to the carrier from water solubility and a minimal immune response. The developed framework enables the loading of other biomolecules through an amine group (-NH_2) and it is a suitable candidate for *in vivo* animal tests (e.g. using mouse models). Applications ranging from controlled target drug

delivery and gene therapy to tissue repair, biosensing and diagnosis, can be envisaged using this framework.

A Fe@C NWs / AAO magnetic nanocomposite was also synthesized by template-assisted electrodeposition followed by CVD at 900 °C. The porous AAO matrix offers a high chemical and mechanical resistance. This has been attributed to the formation of θ- and δ-Al_2O_3 at high temperature. The embedded Fe NWs are covered by very high quality graphitic carbon. The carbon quality allows long-term stability over corrosion of the iron core and provides a framework for reliable linker chemistry. These carbon nanospots can be functionalized to provide anchor points for cells to adhere, for biosensing or triggered drug release. Magnetic measurements reveal a soft ferromagnetic behaviour in all the investigated samples. The produced nanocomposite is bioinert, non-cytotoxic and anti-biofouling to fibroblasts. We can conclude that by changing the nanostructured surface properties of the material, from porous alumina to filled AAO nanocomposite, one can turn a bioactive material into a bioinert one. The multiple properties of the developed nanocomposite make it a suitable candidate for implementation in several distinct applications. In the field of electronics, it can be used for data storage as magnetic recording media. In medicine, it can be used for electrical or magnetic cell stimulation as an implant or cardiac patch. Also, they can be used as building blocks in a more complex implantable biosensor transducer or as micro-motor/robot with high anti-fouling ability. Our nanocomposites may be employed also as on-demand collectors of residual magnetic nanoparticles in biological environments or in microfluidic devices (lab-on-a-chip) or other applications in which anti-biofouling is desired.

2.5 Bibliography

[2.1] A.M. Lindo et al., 2015, "The biocompatibility and anti-biofouling properties of magnetic core–multishell Fe@C NWs–AAO nanocomposites", *Phys. Chem. Chem. Phys.*,17, 13274;

[2.2] M.A. Zeeshan et al., 2012, "Graphite Coating of Iron Nanowires for Nanorobotic Applications: Synthesis, Characterization and Magnetic Wireless Manipulation", *Adv. Funct. Mat.*, 23, 823–831;

[2.3] T. Dvir et al., 2010, "Nanotechnological strategies for engineering complex tissues", *Nat. Nanotechnology*, 6, 13-22;

[2.4] K.S. Napolsky, et al., 2003, "Preparation of ordered magnetic iron nanowires in the mesoporous silica matrix", *Materials Science and Engineering C*, 23, 151–154;

[2.5] J. Kao et al., 2014, "Rapid fabrication of hierarchically structured supramolecular nanocomposite thin films in one minute", *Nat. Commun.*, 5, 4053;

[2.6] B. Maxit et al., 2012, "Facile formulation of high density well-ordered nanoparticle–copolymer nanocomposites", *Soft Matter*, 8, 1317–1320;

[2.7] L. Liu et al., 2008, "Fabrication and characterization of a flow-through nanoporous gold nanowire/AAO composite membrane", *Nanotechnology*, 19, 335604;

[2.8] T.V. Thamaraiselvi and S. Rajeswari, 2004, "Biological Evaluation of Bioceramic Materials - A Review", *Trends Biomater. Artif. Organs*, 18(1), 9–17;

[2.9] W. Lee, 2010, "The Anodization of Aluminum for Nanotechnology Applications", *The Journal of The Minerals, Metals & Materials Society*, 62(6), 57-63;

[2.10] a) M. Darder et al., 2006, "Encapsulation of enzymes in alumina membranes of controlled pore size", *Thin Solid Films*, 495, 321–326. b) W. Lee and S.-J. Park, 2014, "Porous Anodic Aluminum Oxide: Anodization and Templated Synthesis of Functional Nanostructures", *Chem. Rev.*, 114, 7487-7556;

[2.11] A.M. El-Sherik and U. Erb, 1995, "Synthesis of bulk nanocrystalline nickel by pulsed electrodeposition", *Journal of Materials Science*, 30, 5743-5749;

[2.12] K. Schickle et al., 2012, "Towards osseointegration of bioinert ceramics: Introducing functional groups to alumina surface by tailored self assembled monolayer technique", *Journal of the European Ceramic Society*, 32, 3063–3071;

[2.13] L. Fernández-Romero et al., 2008, "Assessment of the thermal stability of anodic alumina membranes at high temperatures", *Materials Chemistry and Physics*, 111, 542–547;

[2.14] D. Brüggemann, 2013, "Nanoporous aluminium oxide membranes as cell interfaces", *J. Nanomater.*, 2013, 1–18.

[2.15] M. Karlsson et al., 2003, "Initial in vitro interaction of osteoblasts with nano-porous alumina", *Biomaterials*, 24, 3039–3046;

[2.16] D. Gong et al., 2003, "Controlled Molecular Release using Nanoporous Alumina Capsules", *Biomedical Microdevices*, 5(1), 75-80;

[2.17] A. Santos et al., 2012, "Nanoporous anodic aluminum oxide for chemical sensing and biosensors", *Trends in Analytical Chemistry*, 44, 25-38;

[2.18] T.A. Desaiet al., 2000, "Nanoporous anti-fouling silicon membranes for biosensor applications", *Biosens. Bioelectron.*, 15, 453–462;

[2.19] D. Losic and S. Simovic, 2009, "Self-ordered nanopore and nanotube platforms for drug delivery applications", *Expert Opin. Drug Deliv.*, 6(12), 1363-1381;

[2.20] I. Banerjee et al., 2011, "Antifouling Coatings: Recent Developments in the Design of Surfaces That Prevent Fouling by Proteins, Bacteria, and Marine Organisms", *Adv. Mater.*, 23, 690–718;

[2.21] D.R. Rolison et al., 2009, "Multifunctional 3D nanoarchitectures for energy storage and conversion", *Chem. Soc. Rev.*, 38, 226–252;

[2.22] E. Pellicer et al., 2010, "Nanocrystalline Electroplated Cu–Ni: Metallic Thin Films with Enhanced Mechanical Properties and Tunable Magnetic Behavior", *Adv. Funct. Mater.*, 20, 983–991;

[2.23] R. Malik et al., 2014, "Magnetic memory effects in nickel ferrite/polymer nanocomposites", *Applied Physics Letters*, 104, 122407;

[2.24] D.-L. Zhao et al., 2006, "Inductive heat property of Fe3O4/polymer composite nanoparticles in an ac magnetic field for localized hyperthermia", *Biomed. Mater.*,1,198–201;

[2.25] R. Hao et al., 2010, "Synthesis, Functionalization, and Biomedical Applications
of Multifunctional Magnetic Nanoparticles", *Adv. Mater.*, 22, 2729–2742;

[2.26] C.C. Berry and A.S.G. Curtis, 2003, "Functionalisation of magnetic nanoparticles for applications in biomedicine", *J. Phys. D: Appl. Phys.*, 36, R198–R206;

[2.27] B. Jang et al., 2015, "Undulatory Locomotion of Magnetic Multilink Nanoswimmers", *Nano Lett.*, 15(7), 4829–4833;

[2.28] R.M. Hernández et al., 2004, "Template Fabrication of Protein-Functionalized Gold-Polypyrrole-Gold Segmented Nanowires", *Chem. Mater.*, 16, 3431-3438;

[2.29] L. Lacerda et al., 2006, "Carbon nanotubes as nanomedicines: From toxicology to pharmacology", *Advanced Drug Delivery Reviews*, 58, 1460–1470;

[2.30] I.K. Herrmann et al., 2009, "High-strength metal nanomagnets for diagnostics and medicine: carbon shells allow long-term stability and reliable linker chemistry", *Nanomedicine*, 4(7), 787-798;

[2.31] A. Vaseashta and D. Dimova-Malinovska, 2005, "Nanostructured and nanoscale devices, sensors and detectors", *Science and Technology of Advanced Materials*, 6, 312–318;

[2.32] J.H. Sakamoto et al., 2010, "Enabling individualized therapy through nanotechnology", *Pharmacological Research*, 62, 57–89;

[2.33] S. Ji et al., 2010, "Carbon nanotubes in cancer diagnosis and therapy", *Biochimica et Biophysica Acta*, 1806, 29–35;

[2.34] A.-M.J. Haque et al., 2012, "An Electrochemically Reduced Graphene Oxide-Based Electrochemical Immunosensing Platform for Ultrasensitive Antigen Detection", *Anal. Chem.*, 84, 1871−1878;

[2.35] Z. Liu et al., 2009, "Preparation of carbon nanotube bioconjugates for biomedical applications", *Nat. Protocols*, 4(9), 1372-1382;

[2.36] Y. Liu and H. Wang, 2007, "Nanotechnology tackles tumours", *Nat. Nanotechnology*, 2, 20-21;

[2.37] A.C. Ferrari and D.M. Basko, 2013, "Raman spectroscopy as a versatile tool for studying the properties of graphene", *Nat. Nanotechnology*, 8, 235-246;

[2.38] M.J. O'Connell et al., 2001, "Reversible water-solubilization of single-walled carbon nanotubes by polymer wrapping", *Chemical Physics Letters*, 342, 265-271;

[2.39] N.W.S. Kam et al., 2005, "Carbon nanotubes as multifunctional biological transporters and near-infrared agents for selective cancer cell destruction", *Proc. Natl. Acad. Sci. USA*, 102, 11600–11605;

[2.40] Y.H. Bae and K. Park, 2011, "Targeted drug delivery to tumors: Myths, reality and possibility", *Journal of Controlled Release*, 153, 198–205;

[2.41] R.M. Reilly, 2007, "Carbon Nanotubes: Potential Benefits and Risks of Nanotechnology in Nuclear Medicine", *The Journal of Nuclear Medicine*, 48(7), 1039-1042;

[2.42] F. Li et al., 1998, "On the Growth of Highly Ordered Pores in Anodized Aluminum Oxide", *Chem. Mater.*, 10, 2470-2480;

[2.43] M.S. Dresselhaus et al., 2003, "Nanowires and Nanotubes", *Materials Science and Engineering C*, 23,129 – 140;

[2.44] N. Taşaltın et al., 2009, "Simple fabrication of hexagonally well-ordered AAO template on silicon substrate in two dimensions", *Appl. Phys. A,* 95, 781-7;

[2.45] O. Jessensky et al., 1998, "Self-organized formation of hexagonal pore arrays in anodic alumina", *Applied Physics Letters*, 72(10), 1173-1175;

[2.46] H. Masuda and K. Fukuda, 1995, "Ordered Metal Nanohole Arrays Made by a Two-Step Replication of Honeycomb Structures of Anodic Alumina", *Science*, 268(5216), 1466-1468;

[2.47] M. Paunovic and M. Schlensinger (eds.), 1998, Fundamentals of Electrochemical Deposition, Wiley-Interscience, ISBN: 978-0-471-71221-3;

[2.48] M. Bhardwaj et al., 2011, "Effect of current density and grain refining agents on pulsed electrodeposition of nanocrystalline nickel", *Surface Engineering*, 27(9), 642-648;

[2.49] M.S. Chandrasekar and M. Pushpavanam, 2008, "Pulse and pulse reverse plating - Conceptual, advantages and applications", *Electrochimica Acta*, 53, 3313–3322;

[2.50] E. Pellicer et al., 2011, "A comparison between fine-grained and nanocrystalline electrodeposited Cu–Ni films. Insights on mechanical and corrosion performance", *Surface & Coatings Technology*, 205, 5285–5293;

[2.51] C.T.J. Low et al., 2006, "Electrodeposition of composite coatings containing nanoparticles in a metal deposit", *Surface & Coatings Technology*, 201, 371–383;

[2.52] M. Kumar and Y. Ando, 2010, "Chemical Vapor Deposition of Carbon Nanotubes: A Review on Growth Mechanism and Mass Production", *Journal of Nanoscience and Nanotechnology*, 10, 3739–3758;

[2.53] C.E. Baddour and C. Briens, 2005, "Carbon Nanotube Synthesis: A Review", International Journal of Chemical Reactor Engineering, 3, 1542-6580;

[2.54] M.S. Dresselhaus, G. Dresselhaus and P. Avouris (eds.), 2001, "Carbon nanotubes: synthesis, structure, properties and applications", Springer, ISBN 978-3-540-39947-6;

[2.55] M.J. Hampden-Smith and T.T. Kodas, 1995, "Chemical Vapor Deposition of Metals: Part 1. An Overview of CVD Processes", *Chem. Vap. Deposition*, 1(1), 8-23;

[2.56] Y. Ren and K. Zhang, 2009, "How structure changes in fabrication of large size ordered anodic alumina film?", *Materials Letters*, 63, 1925–1927;

[2.57] A. Ahmad et al., 2009, "Applications of the Static Quenching of Rhodamine B by Carbon Nanotubes", *ChemPhysChem*, 10, 2251 – 2255;

[2.58] D.L. Kirkpatrick et al., 2012, "Carbon Nanotubes: Solution for the Therapeutic Delivery of siRNA?", *Materials*, 5, 278-301;

[2.59] N.W.S. Kam et al., 2006, "Carbon Nanotubes as Intracellular Transporters for Proteins and DNA: An Investigation of the Uptake Mechanism and Pathway", *Angew. Chem. Int. Ed.*, 45, 577 –581;

[2.60] S.M.C. Berman et al., 2011, "Tracking stem cells using magnetic nanoparticles", *Wiley Interdisciplinary Reviews: Nanomedicine and Nanobiotechnology*, 3(4), 343–355;

[2.61] R. Thomas et al., 2013, "Magnetic Iron Oxide Nanoparticles for Multimodal Imaging and Therapy of Cancer", *Int. J. Mol. Sci.*, 14, 15910-15930;

[2.62] J. Deng et al., "Highly active and durable non-precious-metal catalysts encapsulated in carbon nanotubes for hydrogen evolution reaction", *Energy Environ. Sci.*, 7, 1919–1923.

[2.63] A. Gupta et al., 2006, "Raman Scattering from High-Frequency Phonons in Supported n-Graphene Layer Films", *Nano Lett.*, 6(12), 2667-2673;

[2.64] S.-H. Jeong et al., 2004, "Carbon nanotubes based on anodic aluminum oxide nano-template", *Carbon*, 42, 2073–2080;

[2.65] J. Zhu et al., 2013, "Magnetic carbon nanostructures: microwave energy-assisted pyrolysis vs. conventional pyrolysis", *Chem. Commun.*, 49, 258–260;

[2.66] M.I.F. Macedo et al., 2007, "Kinetics of the $\gamma \rightarrow \alpha$-alumina phase transformation by quantitative X-ray diffraction", *J. Mater. Sci.*, 42, 2830-2836;

[2.67] J. Escrig et al., 2008, "Geometry dependence of coercivity in Ni nanowire arrays", *Nanotechnology*, 19, 075713;

[2.68] M.R. Gallas and G.J. Piermarini, 1994, "Bulk Modulus and Young's Modulus of Nanocrystalline γ-Alumina", *J. Am. Chem. Soc.*, 77(11), 2917–2920;

[2.69] T. Van Gestel et al., 2002, "Alumina and titania multilayer membranes for nanofiltration: preparation, characterization and chemical stability", *J. Membr. Sci.*, 207, 73–89;

[2.70] B. Su et al., 2007, "Porous and Bioactive Alumina Ceramics for Bone Grafts and Tissue Engineering Scaffolds", *Bioceramics*, 19, 975-978;

[2.71] H. Leese et al., 2013, "Wetting behaviour of hydrophilic and hydrophobic nanostructured porous anodic alumina", *Colloids and Surfaces A: Physicochem. Eng. Aspects*, 420, 53– 58;

[2.72] R. Redón et al., 2005, "Contact angle studies on anodic porous alumina", *Journal of Colloid and Interface Science*, 287, 664–670;

[2.73] N. Tasaltin et al., 2011, "Preparation and characterization of superhydrophobic surfaces based on hexamethyldisilazane-modified nanoporous alumina", *Nanoscale Research Letters*, 6, 487;

[2.74] I. Turkyilmaz (ed.), 2011, "Facial Prosthesis, Implant Dentistry - A Rapidly Evolving Practice", InTech, ISBN: 978-953-307-658-4;

[2.75] O. Ergeneman et al., 2010, "In vitro oxygen sensing using intraocular microrobots", *IEEE Trans Biomed Eng.*, 59, 3104-3109;

[2.76] M. Nosonovsky and B. Bhushan, 2009, "Superhydrophobic Surfaces and Emerging Applications: non-adhesion, energy, green engineering"*, Current Opinion in Colloid & Interface Science*, 14, 270–280.

Chapter 3

Measurement of intracellular pollen tube properties using micro/nano-probes

The work of this chapter was done as part of the SNSF (Swiss National Science Foundation) funded project "Wireless Magnetic Nanoprobes: a Tool for Characterizing and Modeling Cell Biomechanics". This work was done in collaboration with Mr. Bumjin Jang from Prof. Bradley Nelson's group, as well as Dr. Hannes Vogler and Dr. Ulrike Nienhaus from Prof. Ueli Grossniklaus' group, Institute of Plant Biology - University of Zürich (UZH).

3.1 Introduction

Plant biodiversity is fundamental for the maintenance of life on Earth. The study of plants is important not only because they provide food, climate control and raw materials, but also because they provide medicinal compounds and help in understanding certain processes happening in the animals.[3.1] Mendel's studies of peas, for instance, revealed the laws of inheritance, which helped understanding human diseases originating from a genetic background. By comparing the development of the plant *Arabidopsis thaliana* (Arabidopsis) and the animal *Drosophila melanogaster*, similar pattern formation processes are seen in both species.[3.2]

Plant and animal cells have many structural similarities because they are both eukaryotic cells (fig. 3.1). Membrane-bound organelles such as the nucleus, mitochondria, endoplasmic reticulum, Golgi apparatus, lysosomes, and peroxisomes

can be found in both cell types. Both also contain similar membranes, cytosol and several common cytoskeletal elements. Nevertheless, few but very significant differences exist between plant and animal cells. Plant cells are typically larger than animal cells, ranging from 10 up to 100 micrometers in size. Beyond size, the main structural differences between plant and animal cells lie in the additional structures found in plant cells. These structures include chloroplasts, vacuoles and the cell wall. Plant cells have a rigid cell wall formed of cellulose that surrounds the cell membrane. This simple difference produces fixed rectangular cell shapes in plants whereas animal cells are round and irregular in shape.[3.3] Given the lack of a rigid cell wall, animal cells were able to develop a greater diversity of cell types, tissues and organs. Animal cells can also move through the use of structures such as cilia or flagella.[3.4]
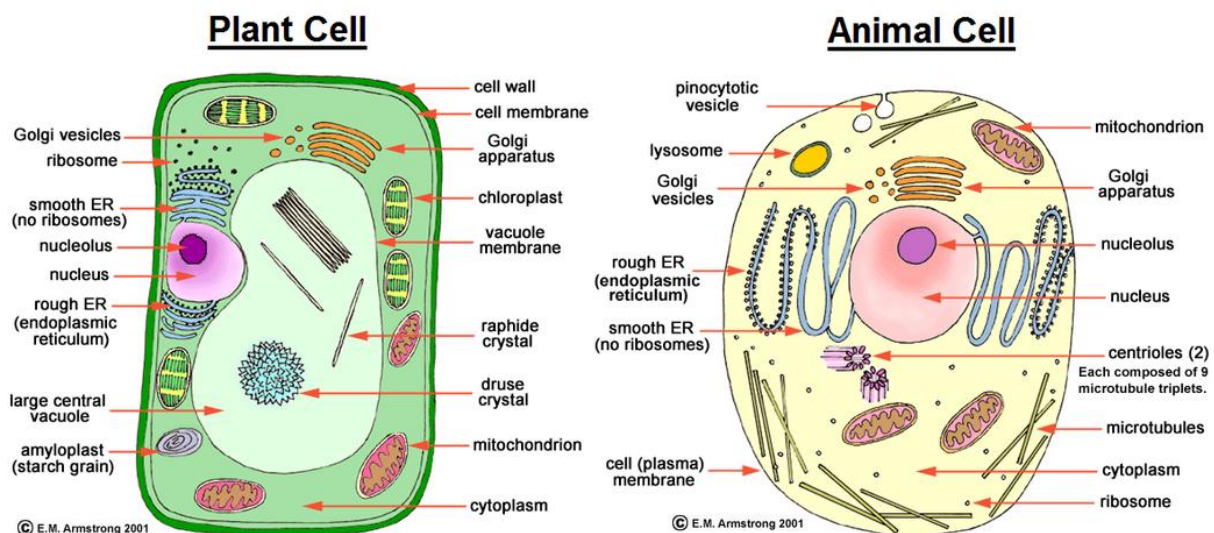
Figure 3.1 Cross-section of different eukaryotic cells, namely, plant and animal cells. Plant and animal cells share many common structures as depicted in this figure. Nevertheless, the existence of a rigid cell wall in plants makes the major structural difference between them. These cell types also possess a few structures that are not shared between them, namely, plant cells have chloroplasts and large vacuoles while animal cells have centrioles, cilia or flagella and small vacuoles. (Image taken from Armstrong [3.4])

Increasing evidence shows that physical factors and mechanical properties regulate biological functions. Mechanical forces acting on a cell can influence gene expression, cellular differentiation, cellular physiology, cell-cell communication, and

cell migration. Different cell types and tissues react in a distinct manner to mechanical stimuli, which can result in specific functional changes identical to many of those induced by biochemical factors.[3.5] It has recently been recognized that local mechanical stimuli impact, for instance, stem cell differentiation. Such stimuli could be used to treat a variety of diseases in the near future.[3.6] The nature and effect of mechanical forces on biological systems such as cells and tissues is still largely unknown. The investigation of biomechanical processes promises novel insights that are not only of great importance for fundamental biology but also have significant near-term applications.[3.7] Insights gained from these processes are of relevance for plant stress response, for instance, where mechanical forces at the cellular level change upon water loss or pathogen attack[3.8] as well as for tissue engineering and the microrobotic manipulation of tissues for biomedical applications.[3.9]

The characterization of the mechanical properties of biological entities can be useful to detect, for instance, disease states of a cell.[3.10] Recent studies show that certain pathological processes are associated with specific mechanical signatures of the affected tissues: as an example, cultured cancer cells exhibit higher elasticity relative to healthy ones.[3.11] Microelectronic devices and microrobotic systems allow the measurement and manipulation of mechanical forces on biological systems ranging from the molecular level to the tissue level.[3.12-14] As an example, manipulation of cells using microelectromechanical systems (MEMS)-based force feedback with an injection micropipette combined with vision feedback was used to investigate the mechanical hardening of the *zona pellucida* - the extracellular membrane of oocytes - after fertilization.[3.15] Studies of this kind demonstrate the advantages that precise microrobotic manipulation of individual cells presents for investigating changes in their cellular behavior.

The work reported in this chapter focuses on the development of a new engineering approach for measuring and manipulating the biochemical and mechanical properties, such as viscoelasticity, pH or calcium levels, of cell membranes and their intracellular media (i.e. cytoplasm and organelles). The wireless manipulation of magnetic micro/nano-probes along three translational axes (3D), and additional rotational axes, enables new types of measurements at both extra- and intracellular levels. The miniaturized probes are precisely and wirelessly controlled by a microrobotic system consisting of a multiple-degree-of-freedom

electromagnetic platform combined with a fluorescence microscope for the visual tracking of the probes.[3.16] Furthermore, different fabrication and functionalization approaches to the micro/nano-probes were explored to enable their use as precise instruments to manipulate internal structures of a cell. The application of this technology enables the measurement and manipulation of internal properties of living cells as well as simultaneously monitoring the cellular responses in real-time. In particular, this work focused on the intracellular properties of growing pollen tubes, which are cells with a clear polar axis and unidirectional growth.[3.12]

In pollen tubes, external probing can only account for wall and turgor properties which are not sufficient to explain polarized tip growth. In order to better understand the mechanisms behind this unidirectional growth, cytoplasmic properties need to be assessed using intracellular probes. For animal cells there is a plethora of available literature regarding different nanoparticle types (magnetic and non-magnetic) for intracellular probing, such as oligonucleotide-modified gold nanoparticles [3.17] or magnetic fluorescent Fe_3O_4-CdSe nanoparticles [3.18]. There are fewer articles available on nanowires/nanorods which is most likely due to the size-related uptake difficulties. Some examples are CdSe/CdS/ZnS as biolabeling probes[3.19] and gold nanorods providing intracellular 3D tracking.[3.20] For plants there is much less literature available on intracellular probes and it essentially comprises gold or tungsten micro/nano-particles[3.21], with the transformation methods limited mainly to protoplast transformation[3.22] or particle bombardment[3.23]. There are also a few reports on nanoparticle penetration[3.24] or endocytosis[3.25] in plant cells, but these processes typically require a few days to occur. We report the first magnetic nanowires used as intracellular probes in pollen tubes.

3.1.1 Pollen tube growth

Pollen tube growth is a fascinating and essential phenomenon in the life cycle of flowering plants (angiosperms). Pollen tube growth is the process by which flowering plants accomplish the transport of the male gametes to the female ovule. Pollen tubes are among the fastest growing cells. They can grow at speeds up to 1 cm/h *in vivo* even though *in vitro* their growth rate can be 90% less.[3.26] Their

length can reach a few centimeters while their diameter is only 5 μm in Arabidopsis and 20 μm in *Lilium longiflorum* (lily) - figure 3.2.[3.26] Their fast growth rate is only possible due to a highly polarized structure. To accomplish polarized growth and successful delivery of the sperm cells, many cellular functions must be orchestrated spatially and temporally. The main cellular functions involved in pollen tube growth include exocytosis and endocytosis, cytoplasmic streaming, ionic gradients and currents, wall synthesis, and the generation of turgor pressure.[3.27]
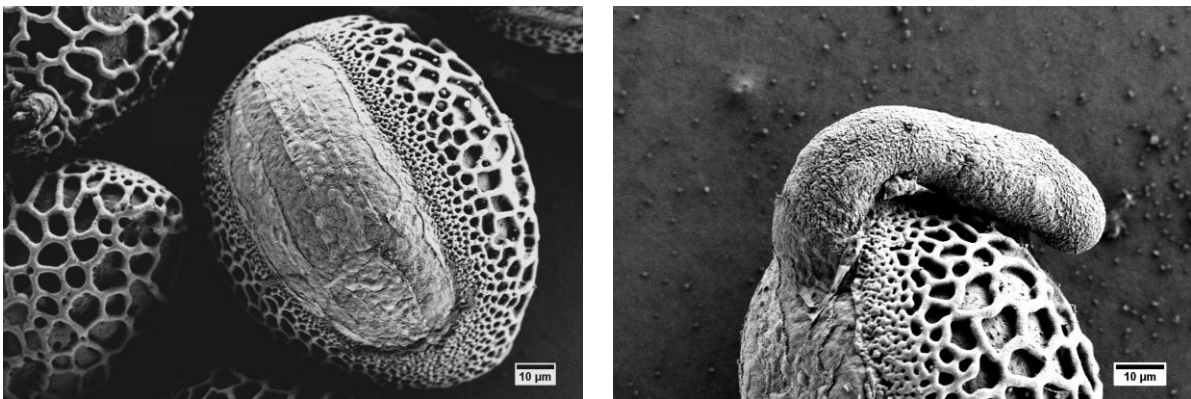
Figure 3.2 SEM images taken from lily pollen tubes and grains. It is possible to see the highly sculpted exine and other fine features of the pollen's surface.

Pollen grain formation in angiosperms

Pollen grains are produced by meiosis of microspore mother cells which are located on the inner side of the anther sacs (microsporangia).[3.28] Sexual reproduction in flowering plants begins with the deposition of a pollen grain, delivered by an insect, the wind or other means, on the female stigmatic tissue. Upon landing and adhering on the stigmatic surface of the pistil, if the pollen-stigma interaction is compatible, the pollen grain will hydrate and germinate, extruding a polarized protuberance to form a pollen tube. The pollen tube elongates and penetrates into female pistil tissues, targeting the ovules that are often located at distances thousands of times larger than the diameter of the grain (fig. 3.2).[3.29,3.30] Growth is restricted to the tube apex; as the tip advances, periodic callose deposition ("callose plugs") occurs distal to the migrating cell front, compartmentalizing the vegetative nucleus and two sperm cells to the most proximal region of the elongating tube. The tube must grow through the style and then take a

sharp turn toward the ovule to finally deliver the sperm cells.[3.31] When the pollen tube enters the ovule it releases its cargo onto the degenerating synergid cells by bursting at the tip. At this point, double fertilization occurs: one sperm cell fuses with the egg cell to form the embryo while the second sperm cell fertilizes the central cell to generate the endosperm.[3.32,3.33]

Polarized tip-growth: similarities in animals and plants

In both animals and plants, guidance cues from the female tissues are critical to accomplish fertilization. Only a few systems use polarized tip growth: pollen tubes, fern and moss protonemata, and root hairs in plants; hyphae in fungi; and neurites in animals.[3.29] In all these systems, cells grow towards a molecular gradient, which is defined as chemotropism.[3.34] In neural cells a calcium gradient is fundamental for synaptic activity and vesicle exocytosis regulation, events that are parallel to what happens in pollen tubes. Other small molecules, such as gamma-aminobutyric acid (GABA), are also involved in cell guidance in both systems.[3.28,3.31] Adhesion molecules are implicated as well in guidance events during reproduction and development in both plants and animals, including neuron guidance. Due to these considerable similarities, pollen tubes are regarded as models for axon polarized growth.[3.35,3.36]

L. longiflorum pollen and germination

The plant model used in this work was Easter lily pollen (*L. longiflorum*) - figures 3.2 and 3.3. The lily pollen tube is one of fastest-growing plant cells and is easily grown *in vitro* when germinated from frozen pollen. One of the major disadvantages of lily is that, unlike in Arabidopsis or *N. tabacum* (tobacco), it is difficult to perform stable transformations, such as genetic modifications.[3.31] Also unlike Arabidopsis and tobacco, in which pollen tubes must penetrate the stigma, lily pollen germinates and grows on a broad stigmatic surface covered with a secretory extracellular matrix (ECM) and enters the style by three narrow openings that converge at the center of the open stigma (figs. 3.2 & 3.3). Lily pollen tubes accomplish the amazing feat of travelling through a 10-cm stylar channel to succeed in fertilization.[3.37] Pollen of most species will germinate and grow a tube *in vitro* when placed in a solution containing calcium, boron, and an osmoticant (such as sucrose or PEG, e.g.). However, even with highly optimized germination media, *in*

vitro tubes reach only 30 to 40 % of the *in vivo* length, and structural anomalies are frequently observed. Nevertheless, *in vitro* germination provides a controlled experimental system with a high degree of reproducibility.[3.38]
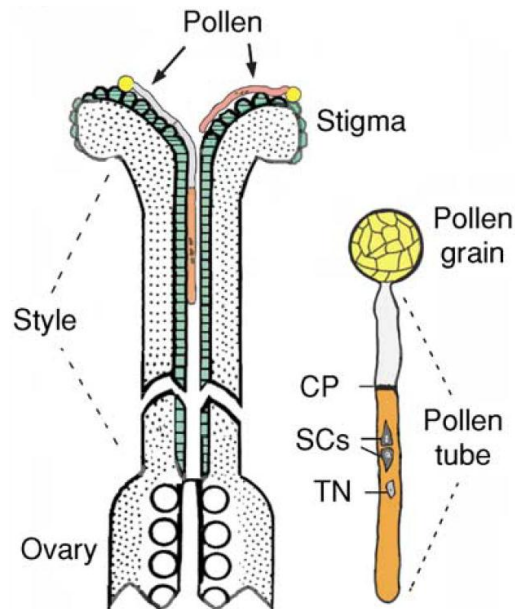
Figure 3.3 Pollination and pollen tube guidance in lily. Schematic drawings depicting a longitudinally sectioned pollinated lily pistil (stigma, style and ovary). In the schematics it is possible to see pollen grains (yellow) that landed on the stigma surface, where they adhere, hydrate and germinate to form pollen tubes. The pollen tube grows through the style to deliver two sperm cells (SCs) to the ovary. The tube nucleus (TN) and the two sperm cells are kept at the tip region by the formation of a series of callose plugs (CP) along the way. (Image taken from Lord et al.[3.37])

General architecture and cytoplasmic streaming

In the tip growing region of the pollen tube, within 50 μm from the tip, this cellular domain is commonly subdivided into four regions: apex, apical flank (or shoulder), subapical region, and shank of the tube (fig. 3.4).[3.14,3.38]

The apex and apical flank regions are clear of large organelles but full of secretory vesicles from the Golgi apparatus. This creates a "clear zone" that typically occupies 5-20 μm from the tube tip (larger in Lily than in Arabidopsis or tobacco) forming an inverted cone-shaped domain. The name is derived from the fact that this zone lacks the starch-containing amyloplasts that cause strong light scattering.[3.39]

Behind the apical region there is the subapical region. In this zone not only secretory vesicles are found but also many organelles such as the endoplasmatic

reticulum, plastids, mitochondria and Golgi stacks. The subapical region is mainly a passage zone for endo/exocytic vesicles. In lily, mitochondria are positioned in the subapical region, presumably supplying the energy demand for cell growth.[3.29,3.31] Further back, in the shank region, larger organelles such as plastids and vacuoles can be found. The main function of the vacuoles is to store water and maintain the turgor pressure inside the tube.[3.27,3.39]

The organellar distribution in pollen tubes is evolutionarily optimized for the targeted secretion of new cell wall material to the apex, promoting cell growth. Cytoplasmic streaming contributes to their fast growth rates but the growth itself is not dependent on it.[3.31] Organelles such as mitochondria and the endoplasmic reticulum move in a "reverse-fountain" cytoplasmic streaming pattern. In this sense, the organelles move from the shank near the cell walls toward the apex before turning inward at the subapical region (before the clear zone) and flowing back in the center of the tube toward its base (fig. 3.4).[3.32,3.40,3.41]

Vesicles flow in a different manner and with different speeds than organelles. In lily pollen tubes, exocytic vesicles flow toward the apex where they fuse with the plasma membrane releasing arabinogalactan proteins and esterified pectins.[3.31] The vesicles that do not penetrate the apex follow the same reverse direction path as organelles and are later recycled together with endocytic vesicles.[3.41] Endocytic vesicles uptake ECM components secreted from the female tissues at the extreme apex but also recycle excess membrane resources at the subapical and shank regions (fig. 3.4).[3.39,3.41,3.42] The endocytic vesicles flow toward the base of the tube and are later degraded. Exocytosis is mediated by vesicles of around 400nm[3.43] in size while endocytic vesicles never exceed 100 nm in size.[3.44] In the extreme apex itself the vesicle motion is random and chaotic and streaming is not present. The cytoplasm can be modeled as a "fluid-filled sponge".[3.45] It consists of a porous matrix with a contractile elastic network (with cytoskeletal filaments, organelles and ribosomes) and is infiltrated with a cytosolic interstitial fluid (containing water, ions and soluble proteins).[3.45] The cytoplasm of virtually all living cells, from bacteria to mammals, is a highly crowded and structured fluid with up to 40% of the total mass attributed to dissolved macromolecules.[3.46] What is known is that plant cells generally have a higher viscosity and more spatial variability than animal cells.[3.47]
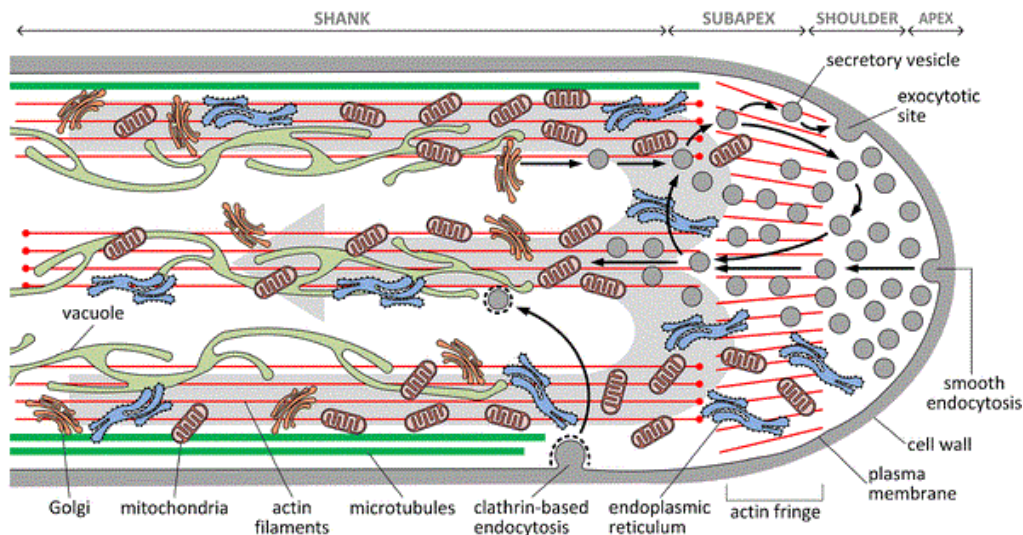
Figure 3.4 Schematics showing the different zones of the pollen tube and a general overview of the organelle trafficking and cytoplasmic streaming. The pollen tube is commonly divided into four segments: the apex, where most of the secretory vesicles accumulate; the shoulder (or apical flank), which is likely to be the site of exocytosis; the sub-apex, where an actin fringe is located and where larger organelles reverse their motion; the shank, where mostly organelles flow towards the tip. The *double-tailed arrow* indicates the general flow of the organelles ("reverse-fountain"). Actin filaments are drawn in red. (Image taken from Cai et al.[3.48])

Cell wall composition

The pollen grain cell wall consists of two layers: one delicate inner pectic-cellulosic layer called intine, and one resistant and highly sculpted outer layer containing sporopollenin called exine.[3.38]

Tip growth in pollen tubes occurs through a delicate balance between loosening of the apical cell wall while maintaining sufficient cell wall rigidity to withstand the considerable turgor pressure without losing cell integrity.[3.34] The pollen tube forms its own cell wall during growth. It generically also contains two layers, an inner sheath consisting of callose and an outer coating containing three main crosslinked polysaccharide polymers: pectin, cellulose and hemicellulose.[3.31]

At the extreme apex, where tube growth is happening, the newly formed cell wall is much thinner and mainly composed of methyl esterified pectins. Pectin methyl esterase inhibitors are accumulated at the extreme apex blocking the de-esterification of pectin. This thin and delicate pectin wall provides enough stiffness to maintain cellular integrity and enough plasticity to allow tube elongation.[3.30,

3.31,3.49,3.50] In lily, the thickness of the cell wall at the extreme apex is around 500 nm.[3.51]

The cell wall modifying enzymes pectin methyl esterases (PMEs), callose and cellulose synthases produce de-esterified pectin, callose and cellulose microfibrils at the plasma membrane in the apical flank region. Once de-esterified, pectins are then crosslinked with Ca^{2+} promoting cell wall stiffening.[3.52] In pollen tubes, cellulose has a low abundance in the cell wall even though it has an important function in maintaining cell shape. In lily pollen tubes, callose has a negligible presence in the cell wall structure. Arabinogalactan and other glycoproteins have also been identified in the cell wall.[3.30,3.37,3.49,3.53]

Apical growth and cytoskeleton

Turgor pressure, i.e. intracellular hydrostatic pressure, is a necessary requirement for plant growth but it is not sufficient to explain the fast growth rates or long tube lengths in pollen tubes. In lily pollen tubes, stable turgor pressure measured *in vitro* is in the range between 0.1 and 0.4 MPa.[3.54,3.55] A minimal turgor pressure is required to generate stress at the pollen tube tip that drives tip wall expansion and tube elongation.[3.56,3.57] Nevertheless, the cytoskeleton and its motor molecules are possibly the main driving force of tube growth via directed exocytic delivery of cell wall materials.[3.29,3.32]

The two major cytoskeletal elements that are present in pollen tubes are actin microfilaments (F-actin) and microtubules, which have a highly organized and dynamic distribution through interactions with several actin-binding and microtubule-associated proteins.[3.58] The main role of actin and microtubules is distinct in plant and animal cells. While they regulate cellular shape in animals, in plants the cell shape is static and determined by the existence of a cell wall.

A dynamic actin network is responsible for the spatio-temporal coordination of the complex vesicle/organelle trafficking (cytoplasmic streaming) involved in apical growth. Actin microfilaments generate cytoplasmic streaming by working together with the motor protein myosin (and others) that is present on the surface of organelles. Myosin contains calmodulin light chains which dissociate from the heavy chain in the presence of high Ca^{2+} and inactivate the myosin.[3.41] Long actin cables present in the tube shank transport vesicles to the subapical region (peripherally) and also backwards (along the central axis), in a "reverse-fountain" streaming

mechanism. The subapical region contains a network of shorter and loosely organized actin cables that constitute the "actin fringe". The "actin fringe" is responsible for the accumulation of vesicles in the "clear zone". An even finer mesh of actin filaments is found at the apex. Small GTPases of the Rho family were proposed as promoters of actin polymerization or stabilization in the "actin fringe" and also regulate microtubule activity.[3.48,3.52]

The roles of the microtubules and microtubule-associated proteins are still not well known and under debate. Accumulating evidence is suggesting that microtubules are involved in organelle movement and may functionally cooperate with actin.[3.14,3.30,3.48] Microtubules were found in different regions of pollen tubes, especially in the shank organized as bundles. There is evidence that microtubules are associated with kinesin-like motor proteins in the clear zone which suggests a putative role for microtubules in short-range vesicle transport.[3.50,3.59]

Ionic gradients and currents

Actin-binding proteins (ABPs) regulate actin dynamics, but their action is regulated by multiple cytoplasmic conditions that influence pollen tube growth, such as Ca^{2+} concentration, pH and phosphoinositides.[3.29]

Calcium ions are required for pollen germination and elongation. It has been demonstrated that pollen tubes follow Ca^{2+} gradients by changing their growth direction.[3.58,3.60] Ca^{2+} enters at the tip of the pollen tube, thus creating a tip-focused Ca^{2+} gradient. The high concentration of Ca^{2+} at the apex promotes actin depolymerization which in turn causes the accumulation of vesicles at the tip and promotes exocytosis.[3.58]

Ca^{2+} and protons (H^+) are both intimately linked to dynamic properties of the cell wall. The concentration of these ions shows oscillatory sinusoidal levels (phase-shifted) that regulate the myosin-based organelle movement and vesicle trafficking.[3.32,3.41,3.58] The pollen tube growth rate is thus intimately related to these ionic oscillatory patterns. It has been demonstrated that high concentrations of protons in the apex (i.e., low pH) are correlated with faster growth rates.[3.61] Pollen tubes display a slightly acidic tip with a pH value around 6.5 (fig 3.5) while the subapical region is slightly alkaline with pH around 7.5. The cytoplasm at the shank has a slowly increasing pH value (from around pH 7) until the subapical region. [3.32,3.61] A polarized H^+ influx occurs through the extreme apex while an H^+ efflux

occurs through the plasma membrane in the subapical region. These events are oscillatory, regulating actin remodeling and cytoplasmic streaming.[3.29,3.32,3.39]
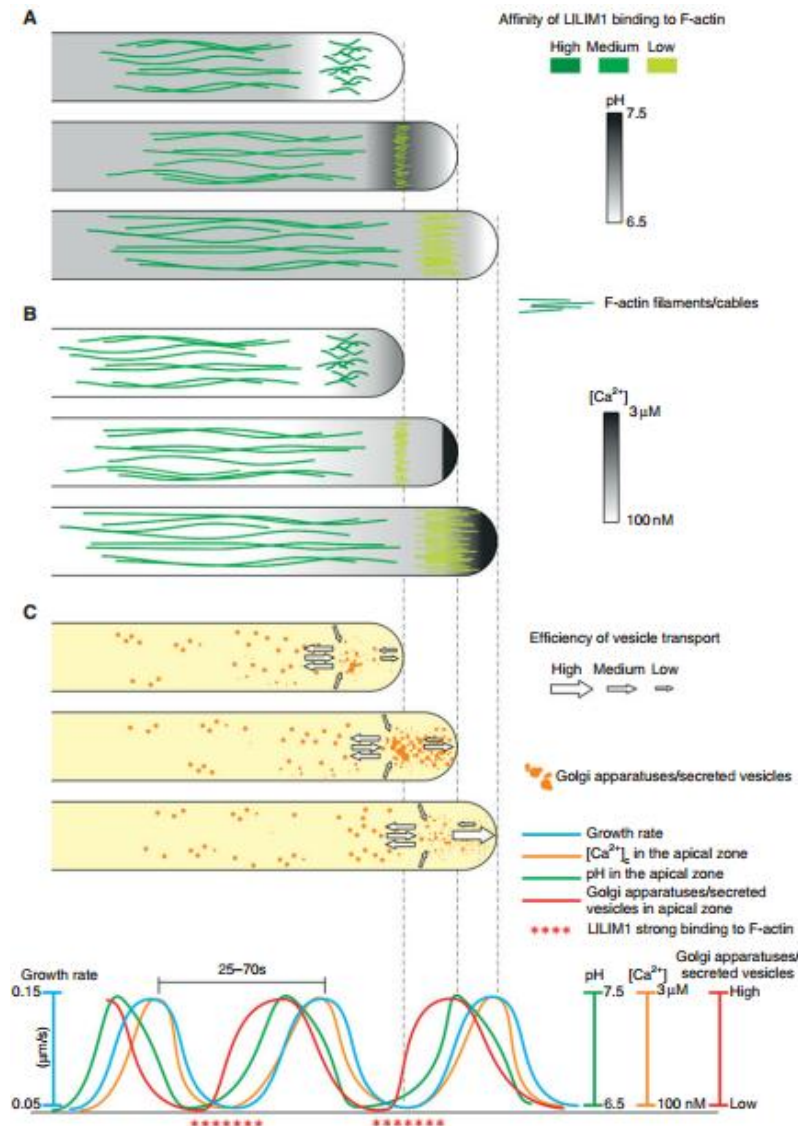
Figure 3.5 Schematics displaying the oscillatory temporal relationships between calcium and proton gradients coupled with the actin dynamics and tube growth. In (A) and (B) it is possible to see the oscillatory proton and calcium gradients coupled with the actin dynamics. In (C) it is depicted that vesicles also follow an oscillatory pattern. At the bottom, the temporal curves of all these events are shown, namely, growth rate, apical pH, apical calcium levels and the apical levels of Golgi apparatuses or secreted vesicles. LILIM1 is an ABP that promotes actin bundling which is promoted by low apical pH and low apical calcium level. (Image taken from Wang et al. [3.32])

The following points summarize the main aspects of pollen tube growth[3.29]:

1. A highly structured intracellular organization of organelles and vesicles orchestrated by a dynamic cytoskeleton network underlie the pollen tip growth process;

2. Polarized ionic conditions - a tip-focused Ca^{2+} gradient, an acidic tip and an alkaline band - are crucial for polarized growth;

3. The plant cell wall is a dynamic composite structure providing high stiffness for maintaining cellular integrity while allowing plastic deformation at the tip;

4. The turgor pressure is the mechanical driving force of tip cell wall elongation;

Pollen tube growth and the underlying cellular and regulatory processes all show oscillatory patterns but with different phase relationships to each other.

3.1.2 Plant transformation methods

Plant transformation methods differ slightly from animal cell transfection methods because of the existence of the cell wall. The most commonly used plant transformation methods are *Agrobacterium*-mediated transformation and particle bombardment.

Through the use of bacteria of the genus *Agrobacterium* a rare inter-kingdom DNA transfer is possible. This unusual plant pathogen (soil bacterium) moves some of its genes into the host's genome. This transformation method has been demonstrated in a large number of species. The advantage of this method is the simplicity of the protocol and the low cost associated with minimal laboratory equipment requirements. This technique was developed in 1983.[3.62,3.63]

The biolistic (biological + ballistic) or particle bombardment method is a physical transfer method that uses microprojectiles to deliver DNA or other molecules into cells (fig. 3.6). The particles and/or DNA are literally fired onto cells using a device called gene gun. This method was first developed to transfer genes into plants and it used gunpowder as the explosive force. Nowadays, the gene gun uses high-pressure helium gas as the accelerating force. Typically gold or tungsten particles with 0.4 to 1.7 μm in diameter are used, even though there are reports of successful internalization of microparticles with up to 5 μm in diameter.[3.64] This method can be used in plants for the transformation of cells, roots, embryos, seeds

or pollen.[3.65] Nevertheless, particle bombardment is the only method capable of delivering DNA into cells of virtually any organism and thus, not limited to plants. This method can be used for the transformation of species that are not susceptible to *Agrobacterium*-infection or not capable of forming protoplast cultures. One disadvantage of this method is the uncontrollable nature of the technique, which creates multiple copies of the gene of interest. Furthermore, this technique requires expensive equipment and there have been reports of inflicted cell damage.[3.66]
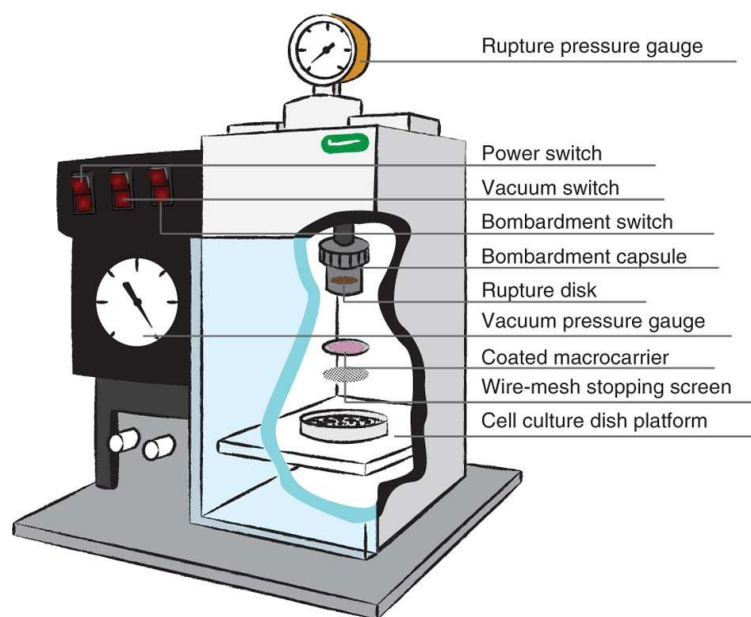
Figure 3.6 Image of the biolistic system from Bio-Rad used to introduce particles into cells. First, particles are placed on the macrocarrier. Upon application of a high gas pressure, the rupture disk breaks at a defined gas pressure, pushing the macrocarrier against the stopping screen (wire mesh). When the stopping screen is reached, the particles are projected onto the cells. (Image taken from Wu et al.[3.67])

Microinjection is a quite famous method for gene transfer in animal cells, dating back to the 19th century.[3.63] It consists of using a micromanipulator to directly introduce DNA into nucleus or cytoplasm using a glass microcapillary. Several different micromanipulator designs are commercially available which makes it a very accessible method, though not one of the cheapest.[3.68] Microinjection is not a common method for plant transformation. The existence of the cell wall in plants again creates some difficulties for the penetration of a microcapillary or

microneedle. A microinjection-based method known as the pressure-probe technique was popular in the 1980s to measure the turgor pressure in plants.[3.69] Microinjection is a time consuming, technically demanding technique and it is unsuitable in many cell types. The efficiency of this technique is not very high, especially in plants, because not all transgenic cells recover from the injection. In protoplasts, for instance, microinjection can cause the release of hydrolases and toxic compounds from the vacuole which leads to protoplast death.[3.66]

Another set of methods often used in plant transformation make use of protoplasts. Protoplasts are cells that had their cell wall removed mechanically or by enzymatic digestion. By having cells surrounded only by the cell membrane it allows other techniques to be used such as PEG/liposome-mediated transformation, which are commonly used in animal cells. Protoplasts can also be transformed using electroporation or microinjection, for instance. Nevertheless, stable transformation has a low efficiency because a protoplast-to-plant regeneration system has not been developed in most plant species.[3.66] Other transformation methods that can be used in plants include electroporation, ultrasonication, electrophoresis and silicon carbide whiskers.[3.62]

3.1.3 Magnetic manipulation at low Reynolds number

Achieving a high level of control for small devices (sub-millimeter) moving in a fluid is far from trivial. An example of the change in the physics governing the motion of bodies can be learned from microorganisms. Locomotion strategies employed by larger organisms at high Reynolds number such as fish, birds or insects, are ineffective at the small scale (micro/nano-scale).[3.70] Microorganisms like bacteria (e.g., *E. coli*) or spermatozoa, use other strategies such as the cork-screw motion or a "run-and-tumble" behavior, because they operate in a low Reynolds number regime (Re << 1).[3.71] A simplified interpretation of the Reynolds number is that it represents the ratio between inertial and viscous forces acting upon a body in a fluid flow. Low Reynolds number means that the motion at small scale is dominated by viscous (frictional) forces.

The Reynolds number (Re) is calculated by taking into account the density of the fluid (ρ), its viscosity (η), the characteristic size of the body (L) and the relative velocity of the flow (v):

$$\mathrm{Re} = \frac{\rho \cdot L \cdot v}{\eta} \sim \frac{F_{inertial}}{F_{viscous}}$$

(eq. 3.1)

Any object when suspended in a fluid is subjected to hydrodynamic forces. At low Reynolds number the inertial forces are assumed to be negligible when compared to the viscous forces.[3.70,3.72] At low Reynolds number, the Navier-Stokes equation for the motion of small objects in viscous fluids can be simplified leading to what is called as the Stokes' law. From the Stokes' law, the viscous resistance or Stokes' drag (drag force, F_{drag}) exerted on a small object[3.73] moving in a fluid at low Reynolds number is given by the equation:

$$F_{drag} = \beta \cdot \eta \cdot v$$

(eq. 3.2)

The drag force depends on the shape of the object (β) and its relative velocity to the fluid (v), and the viscosity of the fluid (η). This equation is only valid for fluids where viscosity is constant regardless of the stress applied, i.e., Newtonian fluids. The geometric coefficient β accounts for the geometry of the object. For an axially translating cylindrical rod with aspect ratio > 2, we consider the approximation of a prolate ellipsoid[3.73] by calculating β from the following equation:

$$\beta = \frac{2\pi \cdot L}{\ln\left(\dfrac{L}{2r}\right) + \gamma_{\parallel}}$$

(eq. 3.3)

The calculation of β accounts for the length (L) and radius of the rod (r), and considers $\gamma_{\parallel}$ as an end correction factor (geometry-dependent). The end correction factor $\gamma_{\parallel}$ for straight circular cylinders was derived by Tirado et al. in reference [3.74].

For swimming at low Reynolds number, microorganisms execute non-reciprocal motion in order to overcome the viscous drag forces. However, small

particles (micro/nano-objects) can be pulled through a fluid with the help of electric or magnetic forces without being constrained to an asymmetric movement. Small particles can thus move while still subjected to viscous drag governed by the Stokes' law (eq. 3.2).[3.72] Ferromagnetic structures (Co, Fe, Ni, alloys and others) are one example of magnetic materials. They naturally align to homogenous magnetic fields and the direction of their motion can be further directed if the structures are anisotropic or non-centrosymmetric (because of an exerted torque).[3.72] This means that the aspect ratio of the structures has to be typically higher than 2. One of the advantages of using magnetic manipulation is that the use of magnetic fields is a non-invasive wireless technique.[3.75]
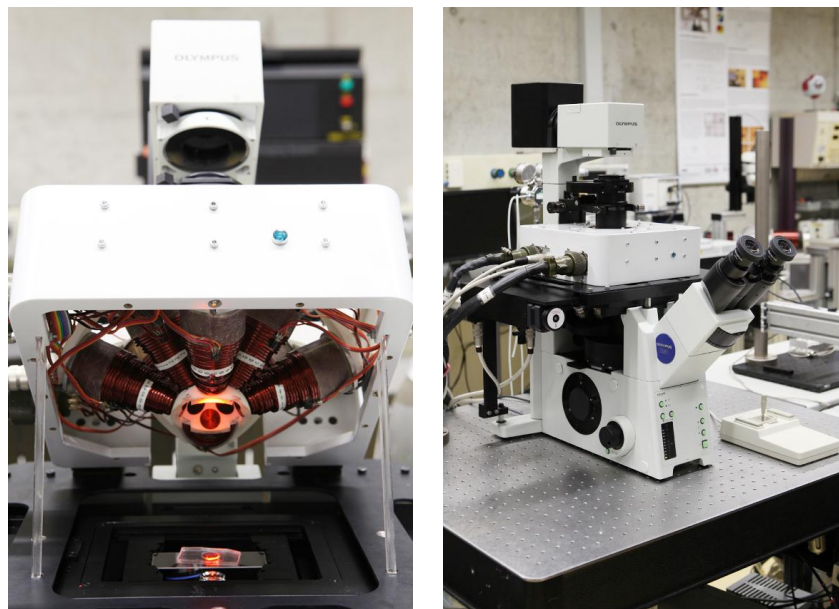
Figure 3.7 Images showing the MFG-100-i magnetic manipulation system (MagnebotiX) integrated in an inverted microscope (Olympus IX 81). It is possible to see the electromagnet coil arrangement in the first picture.

To control and manipulate small magnetic structures, one commercially available magnetic system is the MFG-100-i from MagnebotiX AG (fig. 3.7). It consists of 8 stationary electromagnets (coils) with ferromagnetic cores, thus allowing control with 5 degrees of freedom (5-DOF): 3-DOF position + 2-DOF pointing orientation. This system can generate magnetic fields with strengths up to 50 mT and magnetic gradients with up to 5 T/m, allowing both gradient-based pulling and rotational motion.[3.16] The MFG-100-i was designed to fit an inverted

microscope. This feature allows *in vitro* experiments to be conducted with a high optical resolution (100x objective) together with fluorescence and it can also fit most confocal microscopes.

When a magnetic object is exposed to an applied magnetic field (*B*), its magnetic moment (*m*) experiences a translational force (F_{mag}), described in equation 3.4.[3.72,3.76] The magnetic moment in this case can be either permanent for ferromagnets, or induced as in the case of paramagnets.

$$F_{mag} = \nabla(m \cdot B)$$ (eq. 3.4)

For the case that a magnetic gradient is applied coplanarly to the magnetic object, the object will be pulled along its long axis once its long axis is aligned with the direction of the magnetic field.[3.16] In this case, the magnetic force exerted on the magnetic object (eq. 3.5) can be expressed as a function of the effective magnetization experienced by the object (M_{eff}) and its total magnetic volume (*V*), when subjected to a magnetic field (*B*) with a magnetic gradient (∇B).[3.16,3.76] The magnetic force is then calculated as follows:

$$F_{mag} = V \cdot M_{eff} \cdot \nabla B$$ (eq. 3.5)

3.2 Materials and Methods

3.2.1 Fabrication of CoNi NWs by template-assisted electrodeposition

Nanowires were grown using AAO membranes combined with electrodeposition. The AAO membranes used were either Whatman Anodisc with 200 nm pore size and 47 mm diameter (Sigma-Aldrich) or 400 nm pore size with 25 mm diameter (Shanghai Shangmu Technology Co. Ltd).

The electrochemical setups used consisted of a two-electrode system containing the following elements:

i. Working electrode: sample (AAO membrane)
ii. Counter/Reference electrode: Pt (for Au) and Ni (for CoNi)
iii. Electrolyte: Au or CoNi bath
iv. Container: glass beaker
v. Purging gas: nitrogen (N_2)
vi. Stirrer: magnetic bar
vii. Potentiostat/Galvanostat: Autolab PGSTAT302N, Metrohm
viii. Graphical interface: NOVA 1.8 software, Metrohm

Before electrodeposition, a 200 nm thick layer of Au was evaporated on the filtration side of the AAO membrane, to form a "backside" conductive layer, using an e-beam evaporator (Univex 500, Leybold). The AAO membrane was mounted on a custom-made holder having the conductive side contacting a Cu sheet, making an insulated electrical connection (working electrode). An Au segment was electrodeposited prior to CoNi to work as a "sacrificial plug". This segment avoids current leakage by completely closing the pores on the conductive side. The composition of the Au bath and the DC plating parameters used are listed in tables 3.1 and 3.2, respectively.

Table 3.1 Composition of the Au bath used for electrodeposition

Chemicals	Concentration (g·L^{-1})	
Gold (I) potassium cyanide	0.2	
Potassium citrate	90	
Citric acid	90	complexant
Brightener (containing 0.05 g·L^{-1} Cobalt carbonate)	10 mL·L^{-1}	grain refiner

Table 3.2 Operation parameters for Au electrodeposition

Operating parameters	Condition
Current density	-2 mA·cm^{-2}
Total deposition time	2000 s
Temperature	35 ºC
Stirring speed	300 rpm
pH	4

After the Au "sacrificial plug" was deposited the holder was washed and placed inside the CoNi electrolyte. Pulsed electrodeposition of CoNi NWs (segments) was performed using the bath composition and parameters listed in tables 3.3 and 3.4, respectively.

Table 3.3 Composition of the CoNi bath used for electrodeposition

Chemicals	Concentration (g·L^{-1})	
Nickel (II) sulphate hexahydrate	300	
Nickel (II) chloride hexahydrate	30	
Cobalt (II) sulphate hexahydrate	40	
Boric Acid	20	buffer
Citric acid	40	complexant
Sodium saccharinate	2	stress reducer / refinement agent
Tergitol 08	3 mL·L^{-1}	wetting agent

Table 3.4 Operation parameters for CoNi electrodeposition

Operating parameters	Condition
t_{ON}, t_{OFF}	4, 10 ms
Current density	-100 mA·cm^{-2}
Temperature	55 °C
Stirring speed	300 rpm
pH	5.5

3.2.2 Wet etching of AAO

To dissolve the AAO and recover the CoNi NWs the samples were placed first in a gold etchant solution, nickel-compatible (Sigma-Aldrich), for 30 minutes to remove the gold layers. To remove the AAO, the samples were further immersed in a 5 M solution of sodium hydroxide for 30 minutes. CoNi NWs solutions were obtained by collecting the NWs using a magnet and washing/resuspending them in EtOH 5 times.

3.2.3 Coating of NWs with FITC + polymers using layer-by-layer assembly *(Approach A)*

The first approach used for coating the CoNi NWs consisted of layer-by-layer (LbL) deposition of charged polymers. The polymers used were polyallylamine hydrochloride (PAH) with embedded fluorescein isothiocyanate (FITC) as the cationic polymer (PAH:FITC) and polystyrene sulfonate (PSS) as the anionic polymer.

First, EtOH was evaporated from the CoNi NW solution. CoNi NWs have negative charges on the surface so the first deposited monolayer was PAH:FITC (positively charged), followed by a monolayer of PSS (negatively charged). This cycle was repeated another 3 times thus creating 4 bi-layers. Layer-by-layer deposition was performed by dispersing the NWs first in an aqueous solution of 1 mg/mL PAH:FITC and 0.5 M NaCl, and then in an aqueous solution of 1 mg/mL PSS

and 0.5 M NaCl, each for 30 minutes with continuous shaking. The NWs were suspended between the polyelectrolyte solutions in an alternating way, rinsing the NWs with DI-H_2O between solutions, to remove any unreacted reagents.

3.2.4 Coating of NWs with SiO_2 using sol-gel method (*Approach B*)

The second approach used for coating the CoNi NWs consisted of making a SiO_2 layer using a sol-gel process. Briefly, 0.2 mg of CoNi NWs were first dispersed in 4.5 mL of DI-H_2O using tip sonication (low power) before adding 0.5 mL of an aqueous PVP solution (12 mg/mL). Pulsed tip sonication (t_{ON}: 1 s, t_{OFF}: 5 s) was performed on this solution for 30 min to functionalize the CoNi NWs' surface with surfactant molecules (PVP) and enhance their dispersability. Afterwards, the CoNi NWs were washed five times in EtOH using a magnet to collect them and dried under vacuum for 30min.

PVP-functionalized CoNi NWs were dispersed in a solution containing 5 mL of IPA, 1 mL of DI-H_2O and 180 μL of ammonium hydroxide (NH_4OH, Sigma-Aldrich) in a 15 mL falcon tube (VWR). To start the sol-gel reaction 25 μL of tetraethyl orthosilicate (TEOS, Sigma-Aldrich) were added to the solution. The mixture was allowed to react for 30 min under pulsed tip sonication at low power (t_{ON}: 1 s, t_{OFF}: 5 s). After this time a white solution is formed. The CoNi@SiO_2 core-shell NWs (CSNWs) were washed in DI-H_2O and EtOH several times using a magnet to collect them.

3.2.5 Surface modification of CoNi@SiO_2 CSNWs using APTES silane (*Approach B*)

CoNi@SiO_2 CSNWs were functionalized to acquire amine (-NH_2) functional groups on the surface. For this purpose, ~0.2 mg of CoNi@SiO_2 CSNWs were mixed with 2 mL of EtOH and 10 μL of (3-Aminopropyl)triethoxysilane (APTES, Sigma-Aldrich) and dispersed using pulsed tip sonication at low power (t_{ON}: 1 s, t_{OFF}: 5 s) for 2-3 min. The solution was aged for 20 h in a 15 mL closed falcon tube. The amine-functionalized CoNi@SiO_2 CSNWs were washed in EtOH 2-3 times using a magnet to collect them.

3.2.6 Conjugation of FITC by direct surface attachment (*Approach B*)

The CoNi@SiO$_2$ CSNWs were conjugated with FITC by mixing both in the same solution which promotes direct attachment. For this purpose, ~0.2 mg of amine-functionalized CoNi@SiO$_2$ CSNWs were dispersed in 2 mL of EtOH using pulsed tip sonication at low power (t_{ON}: 1 s, t_{OFF}: 5 s) for 1 minute. This solution was mixed with 0.1 mL of a previously prepared 1 mg/mL FITC in dimethyl sulfoxide (DMSO) solution. The solution was mixed in a vortex mixer for 3 h in the darkness. To remove the unreacted FITC, the CoNi@SiO$_2$-FITC CSNWs were washed in EtOH 2-3 times and then in DI-H$_2$O 5 times, with the help of a magnet.

3.2.7 Growth of CoNi micropillars by 3D photolithography combined with electrodeposition

Transparent round glass slides, 300 μm thick and 30 mm wide (VWR), were used as substrates for making porous templates. After cleaning with acetone and IPA, the substrates were blow-dried with N$_2$ and further dried in an oven for 30 minutes at 200 ºC. A 25 nm ITO layer was evaporated on one side using an e-beam evaporator (Univex 500, Leybold). The substrates were subjected to rapid thermal annealing (JetFirst 100, JIPelec) at 550 ºC for 5 min to make the ITO turn transparent.

After the ITO evaporation the substrates were cleaned again using acetone and IPA, blow-dried with N$_2$ and dried in an oven for 5 minutes at 200 ºC. The substrates were spin-coated with a 10 μm layer of AZ 9260 positive-tone photoresist (MicroChemicals GmbH) and baked at 110 ºC for 2 min.

Micropillar geometries were generated in MATLAB (Mathworks) and a 3D photolithography system (Photonic Professional, Nanoscribe GmbH) was used to expose the photoresist and create microcavities of the desired geometries. The system consists of a direct laser writing system coupled with a three-axis piezo stage and working under two-photon polymerization with a 780 nm laser. The writing speed used was 100 μm/s. After laser exposure, the substrates were developed in AZ 400K (MicroChemicals GmbH) for 15 minutes in a 1:4 dilution with DI-H$_2$O. The substrates

were later immersed in DI-H_2O to remove any developer residues and blow-dried with N_2.

The substrates were mounted on a custom-made holder and an electrical connection was made with the ITO by removing a small area of the photoresist with acetone. The ITO was connected to copper tape (working electrode) and covered with kapton tape (Ted Pella Inc.) for insulation. A wetting step is necessary to remove the air inside the pores and fill them with liquid, thus enabling the electrodeposition process to occur. For this purpose, a drop of DI-H_2O was placed on top of the microcavities and the holder containing the sample was later placed in a desiccator under vacuum for 10 minutes. Pulsed electrodeposition of CoNi micropillars was carried out in a similar way as it was already described for CoNi NWs using the same setup, electrolyte and parameters, which are listed in tables 3.3 and 3.4, respectively.

3.2.8 Characterization of the micro/nano-probes

The morphology of the samples (both NWs and micropillars) was characterized using a scanning electron microscope (ULTRA 55, Zeiss). The thickness of the SiO_2 shell was characterized at 100 kV with a transmission electron microscope (CM12, Philips) by dispersing the NW suspension on a 400-mesh copper grid with an ultrathin carbon layer on a holey carbon support film (Ted Pella Inc.). The fluorescence of the CoNi@SiO_2-FITC NWs was confirmed using a fluorescence microscope (IX81, Olympus).

3.2.9 Preparation of microcapillaries

Microcapillaries were prepared with a micropipette puller (P-2000, Sutter Instrument) using hollow glass capillaries. The capillaries are made of borosilicate thin-wall glass with a length of 100 mm and an outer / inner diameter (OD / ID) of 1 / 0.75 mm (TW100-4, World Precision Instruments). The obtained microcapillaries had an outer diameter of around 2-2.5 μm and the fabrication parameters are listed in table 3.5. The diameter characterization was performed using a scanning electron microscope (ULTRA 55, Zeiss) and an optical microscope (IX81, Olympus).

Table 3.5 Capillary pulling parameters

Heat	Filament	Velocity	Delay	Pull
350		30		
350	4	30	200	0
350		50 – 70		

3.2.10   Pollen germination

Lily anthers were collected three to five days after anthesis, snap-frozen in liquid nitrogen and stored at -80 ⁰C. For germination, an aliquot is taken out of the freezer and placed on ice until it reached RT. Once the pollen was at RT some of the powder was spread on a thin glass slide (Thermo Scientific) using a brush. The pollen grains were allowed to germinate by adding germination medium and keeping them in a humid container. The composition of the germination medium used is listed in table 3.6. After about 1 h the pollen grains started to germinate. The first ones to germinate were selected for further experiments. Lily pollen tubes *in vitro* showed a growth rate of around 20 μm/min.

Table 3.6 Lily germination medium

Chemical component	Concentration
Boric acid	0.16 mM
Calcium nitrate	0.13 mM
Potassium nitrate	1 mM
MES buffer	5 mM
Sucrose	100 mg/mL
pH	5.5 ± 0.1

3.2.11 Centrifugation procedure

Centrifugation was performed using a microcentrifuge at 14.5 krpm (Minispin Plus, VWR). Pollen tubes and grains were placed in separate eppendorfs with germination medium and tested with NWs and micropillars. The centrifugation time used was 60 s for the NWs and 120 s for the micropillars.

3.2.12 Magnetic spearing procedure

For the magnetic spearing experiments we proceeded in a similar way to Cai et al. for mammalian cells[3.77]. A NdFeB permanent magnet was positioned under a sample of germinated pollen tubes. By placing micro/nano-probes in the germination medium on top of the pollen tubes, they were "fired" at the pollen tubes due to the magnetic attraction.

3.2.13 Particle bombardment procedure

Both NWs and micropillars were fired at pollen grains and tubes using the particle bombardment method. The equipment used was a Biolistic PDS-1000/He particle delivery system (Bio-Rad). After 1 h of germination, pollen tubes were labelled with FM 4-64 (Molecular Probes) that works as a stain for the plasma membrane. The dye was added to the germination medium to a final concentration of 0.2 μM. Drops of ethanoic solutions containing the micro/nano-probes (microcarriers) were placed on the macrocarrier and left to dry in air. The optimal quantity of the micro/nano-probes deposited on the macrocarrier was around 0.05 mg. Solutions containing the probes were dispersed using a tip sonicator at low power prior to placing the solution drops on the macrocarriers. Bombardment was tested using rupture disks with 900, 1100 and 1550 psi ratings. Different gap distances between the stopping screen and the target were tested as well, from 6 to 12 cm separation distance. Slides containing germinated pollen grains in germination medium were mounted as the target and received the micro/nano-probes fired at different gas pressures for each sample. Pollen tubes were observed after bombardment using an Olympus IX81 fluorescence microscope. To assess whether

the micro/nano-probes were located inside the pollen tubes, a laser scanning confocal microscope was used (SP2, Leica Microsystems).

3.2.14 Microinjection procedure

A solution of NWs was first cleaned using a magnet and 70 % EtOH. After cleaning, a new NW solution was prepared with germination medium. A few μL of this solution were transferred to a microcapillary using a microloader tip (Eppendorf). The NWs are moved to the tip of the microcapillary by using a permanent magnet to attract them. The injection procedure involved using one capillary to hold the pollen grain (holding capillary) while using the microcapillary (injection capillary) connected to a manual piston pump (CellTram vario, Eppendorf) to inject into the pollen grain. The holding capillary consists of a microcapillary with a broken tip, big enough to hold the pollen grain and small enough not to suck it in. The tube from the peristaltic pump is filled with embryo-tested biocompatible mineral oil (M8410, Sigma-Aldrich) and connected to the microcapillary. Only pollen grains that were recently germinated were selected for microinjection. Once a grain was held with the holding capillary by capillary forces, the grain was perforated using the injection capillary. The pressure from the pump was increased in order to re-inject emerging cytoplasm as well as the NWs into the grain. Simultaneously, the turgor pressure inside the pollen grain was decreased by adding drops of 120 mM mannitol (osmoticant). Once the NWs were inside, the microcapillary was removed and germination medium was added. Injected grains were left to grow overnight whereby tube lengths usually reached above 1 mm.

3.2.15 pH determination experiments

Fluorescence and bright-field images of pollen tubes and FITC conjugated NWs (together and separately) were taken using a fluorescent inverted microscope (IX 81, Olympus) equipped with an illuminating system (xenon lamp) and a charge-coupled device (CCD) camera (C9100-13, Hamamatsu). The software for controlling the microscope and acquiring the images was Olympus xcellence.

For pH measurements inside the pollen tube ratiometric imaging was used. Fluorescent images were taken using a CFP excitation filter (excitation: 418-442 nm) and a FITC excitation filter (excitation: 475-495 nm), while keeping the same emission filter suitable for FITC (emission: 510-540 nm). For calibration, fluorescence images of FITC conjugated NWs in pH buffers ranging from 5 to 8 pH units, with an interval of 0.5 pH units, were taken. To process the fluorescence images and calculate the pH values the Fiji software was used.[3.78] Briefly, the image processing steps to obtain the pH values were as follows: first, an image stack is made with the images from the CFP and FITC excitation channels. Then, a common background area is selected for both images and a background subtraction is performed. To select the fluorescent intensity corresponding only to the NWs' area, an intensity threshold is defined in the channel with the weaker signal and a binary mask made. This mask is then multiplied onto both image channels. The last step involves dividing the FITC channel image by the CFP channel image and collecting the ratio FITC/CFP in the NW area. Once a calibration is obtained from all the FITC/CFP ratios for all the pH buffer measurements, the determination of intracellular pH is done by imaging NWs inside pollen tubes, processing the images as described above and comparing the intensity values to the calibration.

3.2.16   Magnetic poking and manipulation of micro/nano-probes

Magnetic poking and manipulation were performed on micro/nano-probes using a 3D magnetic manipulation system (MFG-100-i, MagnebotiX AG).

To perform magnetic poking, pollen grains were germinated on 1.5% agarose gel to make the pollen tubes grow adherent to the substrate. CoNi micropillars were placed in the germination medium next to a pollen tube. Poking was performed by moving one micropillar against the pollen tube tip using gradient fields of 1 T/m and a magnetic field of 20 mT (B-field).

Magnetic manipulation of intracellularly located micro/nano-probes was accomplished after microinjection. Using the 3D magnetic manipulation system, the micro/nano-probes were moved using gradient fields with 1 T/m and 20 mT (B-field), and alternatively using rotational fields with magnetic field of 20 mT (B-field) and 1-5 Hz. Nanorheological measurements were done by recording pictures of the probe's

movement using a Basler scA1400-30fm camera at 30 frames per second. In a similar but uncontrolled way, micro/nano-probes after microinjection were manipulated intracellularly using a NdFeB magnet after microinjection.

3.3 Results and Discussion

3.3.1 Fabrication of micro/nano-probes

Micro/nano-rods were fabricated using ferromagnetic materials to provide wirelessly controllable intracellular probes. Their dimensions were selected to fit inside the pollen tube. All the magnetic micro/nano-probes that were fabricated and their respective fabrication methods are listed in table 3.7.

Table 3.7 Magnetic micro/nano-probes tested

Probe #	Material	Diameter (nm)	Length (nm)	Fabrication method
1.	Ni	75	1000	Self-made AAO
2.	Ni	250	2700	Commercial AAO
3.	CoNi	250	7000	Commercial AAO
4.	CoNi	400	5000	Commercial AAO
5.	CoNi	500	11000	Nanoscribe[TM]
6.	CoNi	1100	4100	Nanoscribe[TM]

To fabricate NWs with 75 nm in diameter (probe #1) the fabrication method used was the same method as reported previously in Chapter 2 (self-made AAO templates with electrodeposition). NWs and micropillars with larger diameters than probe #1 were fabricated mainly with the aim of reducing aggregation and to

increase the magnetic volume. With the increase in size, the surface to volume ratio decreases which in turn makes the electrostatic forces less dominant.

AAO provides one of the most stable and versatile templates for NW fabrication. However, AAO templates are only commercially available with pore diameters up to 400 nm because of the self-limited nature of the anodization process.[2.10] Therefore, if one wants to produce NWs with diameters larger than 400 nm, other techniques such as 2D or 3D photolithography (Nanoscribe[TM]) must to be used instead.

3D photolithography is useful to produce structures with feature sizes that are in the transition from nano to micro-scale, especially structures with a high degree of complexity. For simple structures, such as 1D structures, Nanoscribe[TM] is not a very efficient method due to multi-step preparation processes and low yield per sample. Even using a simplified geometry such as writing one line for each pillar cavity (positive resist), a sample with only a few thousand structures (template) takes some hours to produce.

a)   b)
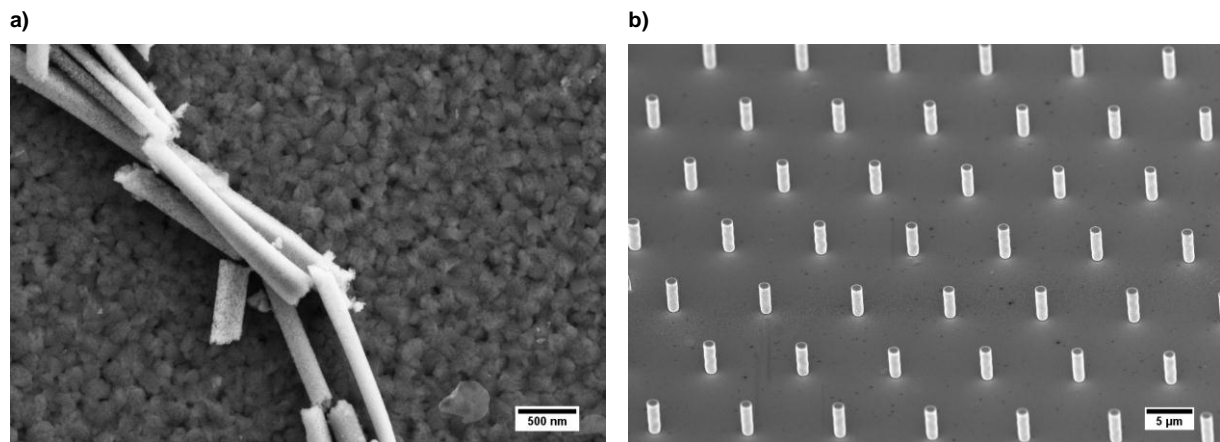
Figure 3.8 SEM pictures of fabricated micro/nano-probes. Images were taken using secondary electron (SE2) detection. a) Nickel nanowires with a size of around 250 nm x 2.7 μm (probe #2). b) Array of CoNi micropillars with a size of around 1.1 μm x 4.1 μm each (probe #6). In b) the images were taken at a 45° angle.

The core of the micro/nano-probes was produced using either AAO templates or templates fabricated using Nanoscribe[TM] (table 3.7) combined with electrodeposition. SEM pictures of some the fabricated probe types are shown in figure 3.8.

To add functionalities to the probes, two different coating approaches were developed. The first coating approach (designated as approach A) consisted of making a polymer coating using the layer-by-layer (LbL) technique. The protocol consisted of depositing a monolayer of a positive polymer (PAH) followed by a monolayer of a negative polymer (PSS), and repeating this cycle several times (fig. 3.9). The core materials used were CoNi or Ni which have negatively charged surfaces. Therefore, a monolayer of PAH (positive) was deposited as the starting point for the LbL method used. PSS and PAH were chosen because they are biocompatible as thin films.[3.79, 3.80] A similar fabrication method has been reported in Jang et al.[3.81] Furthermore, PAH was used in a FITC-conjugated form, on one hand to make the probes fluorescent (traceable) and allowing pH sensing on the other hand. The coating consisted of 4 by-layers to provide stability to the coating and ensure sufficient FITC concentration (fig. 3.9). The micro/nano-probes that were obtained using the coating approach A consisted of CoNi-(PAH:FITC-PSS)$_4$.

Approach A
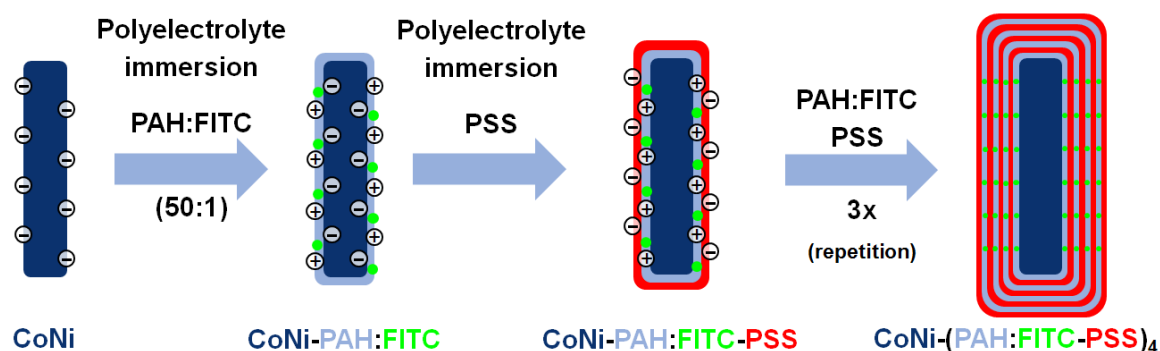
Figure 3.9 Polymer coating of CoNi micro/nano-probes using the LbL technique with FITC-embedded polymers (coating approach A). The polymers are coated by alternating between negative and positively charged polymers. The process is repeated until the desired number of layers is achieved.

The second coating approach (approach B) consisted of making an oxide coating using the sol-gel method and then using silanization together with direct conjugation (fig. 3.10). A SiO$_2$ coating was achieved on the micro/nano-probes by sol-gel according to the Stöber method. Briefly, a SiO$_2$ coating is obtained from the hydrolysis and condensation of the silicate precursor (TEOS) catalyzed by ammonium hydroxide in an ethanol/water mixture.[3.82] Precise control of the reaction components and reaction time makes possible to tune the coating thickness.

Because most metals have little affinity for silica, a surface primer such as APTES or PVP (Polyvinylpyrrolidone) is required to promote silica coating.[3.83,3.84] In coating approach B, the silica surface was further functionalized with amine functional groups (-NH_2) by silanization using APTES. This was done by self-assembly in solution.[3.85] FITC was then conjugated to the surface of the silica-coated probes by direct attachment through amine-carboxyl coupling.[3.86] The final micro/nano-probes obtained after using coating approach B were CoNi-SiO_2-FITC.
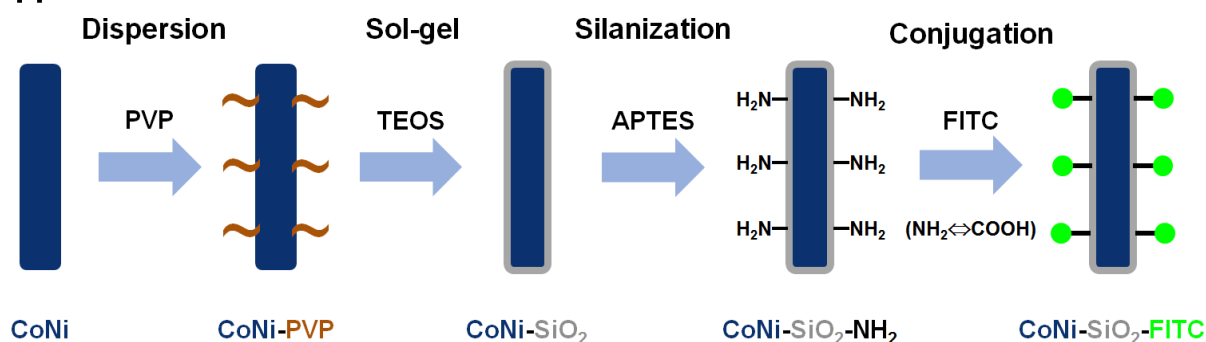
Figure 3.10 Coating of CoNi micro/nano-probes with SiO_2 using PVP functionalization, followed by the sol-gel method and conjugation of FITC by direct attachment after silanization (coating approach B). FITC is attached to the amine (-NH_2) groups by amine-carboxyl coupling.

The sol-gel method was optimized to reduce resource usage and reaction time. A coating of 50 nm was obtained after 30 min by keeping the 200:40:7.2:1 ratio of IPA:H_2O:NH_4OH:TEOS (fig. 3.11). IPA was used instead of ethanol to minimize the absorption of additional water molecules. APTES was also tested instead of PVP as a surface primer for the sol-gel process but this method produced large agglomerates. PVP was shown to promote SiO_2 coating by working as a surface primer and also demonstrated good properties as a surfactant for the CoNi nanorods. Ultrasonication did not prove to be as effective in dispersing the CoNi nanorods as low power tip sonication.

Coating approach A, using a polymer coating, is overall a faster process than approach B. However, the LbL method for polymer deposition is limited to the availability of polyelectrolytes. Commercially, for instance, PAH is limited to a few conjugated molecules and these molecules display a limited concentration. The PAH:FITC used in this work is at a 50:1 ratio. Nevertheless, differently conjugated

polyelectrolytes can be synthesized in the lab but in this case the process becomes more time consuming.
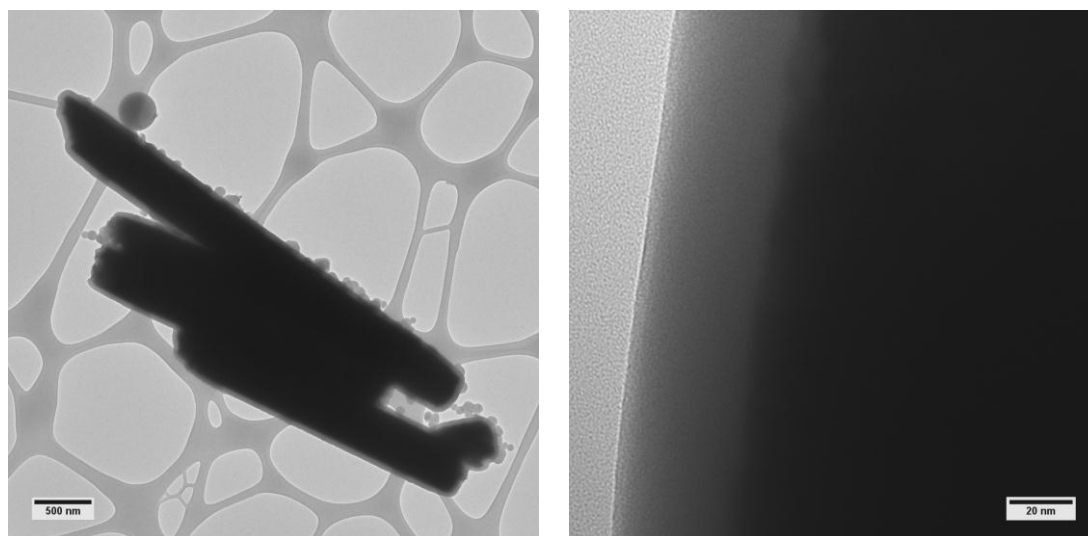
Figure 3.11 TEM images taken at 100 kV of nanoprobes (probe #4) coated with SiO_2 using coating approach B. It is possible to distinguish the SiO_2 layer (dark gray) from the CoNi core (black) by the color contrast.

In the case of coating approach B, silica was chosen because it is a chemically stable, bioinert (biocompatible) and easy to functionalize material.[3.87,3.88] The sol-gel process was chosen because it is a facile synthesis method and the SiO_2 coating allows virtually unlimited functionalization options through silanization. In this sense, the conjugation of any kind of sensing biomolecule is facilitated. The ceramic coating also provides a higher protection of the core from releasing toxic ions or from becoming degraded (e.g., by corrosion).

3.3.2 Centrifugation, magnetic spearing and poking

Particle internalization using centrifugation was briefly tested on lily pollen grains and tubes. Internalization was not achieved by centrifugation at 14.5 krpm using both NWs and micropillars (probes #2 and #6). The micro/nano-probes were not able to penetrate the cell wall, but remained attached to it (fig. 3.12a)).

Magnetic spearing was tested in pollen tubes again using probes #2 and #6. Results were similar to the ones obtained by centrifugation. This is an indication that

the magnetic forces exerted on the micro/nano-probes were not sufficient to penetrate the cell wall of the pollen tubes.

For the case of poking the cell wall from the outside only CoNi micropillars were tested (probe #5). Cell wall disruption was attempted in the apical zone, where the newly formed cell wall is less rigid. The applied magnetic force was around 1.47 pN. This force did not produce any disruption in the cell wall and thus no internalization was possible (fig. 3.12b)). A possible alternative might be to digest the cell wall partially or completely, penetrate the cell membrane and then try to reconstitute the cell wall.
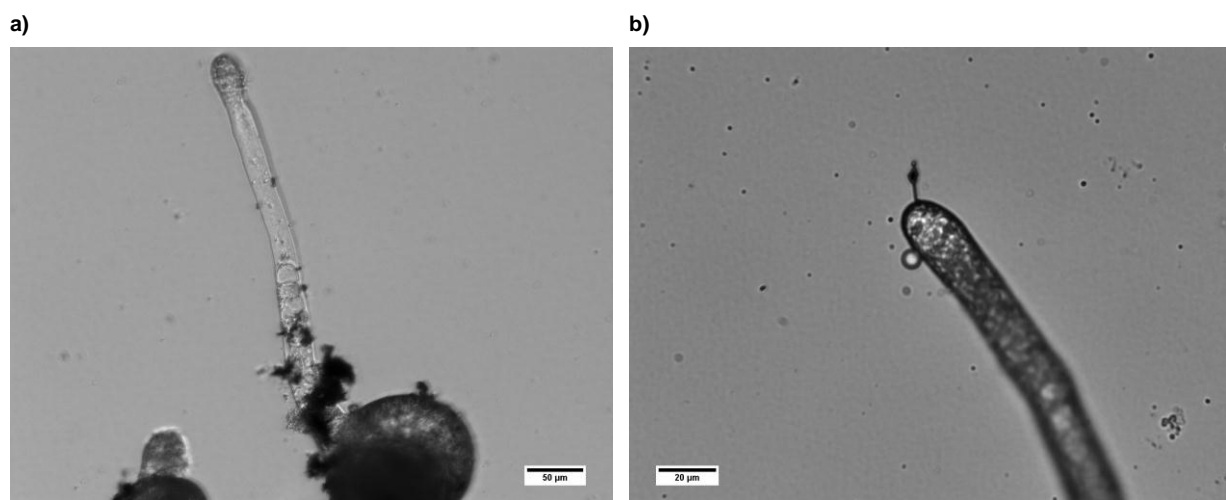
Figure 3.12 a) Bright-field images of pollen tubes and grains after centrifugation with nanoprobes (probe #2). b) Image from a pollen tube and a nanoprobe of around 500 nm x 11 μm, taken during an attempt of tip perforation using magnetic poking (probe #5).

3.3.3 Particle bombardment

Internalization by particle bombardment was tested on pollen tubes using 3 different sizes of micro/nano-probes (probes #1, #2 and #6) with 3 different gas pressures. Bombardment was tested before and after adding germination medium, but this change in the liquid volume didn't produce any difference regarding internalization results. In general, particle bombardment produced large aggregates of micro/nano-probes sticking to the outer part of cell wall of the pollen tubes and grains. Even though it was sometimes difficult to determine whether the micro/nano-

probes were internalized or not using the bright-field image (fig. 3.13), with the help of a permanent magnet it was possible to confirm in most of the cases that the micro/nano-probes were not internalized.
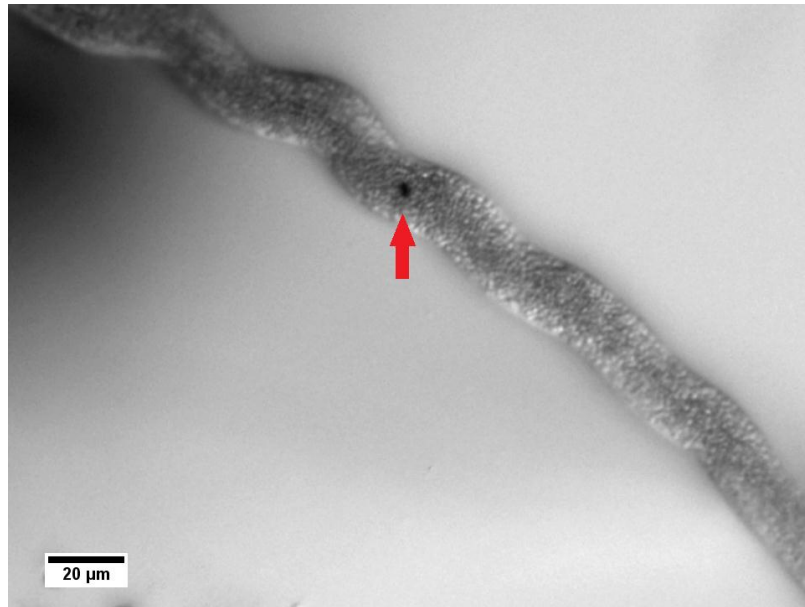
Figure 3.13 Image of a CoNi micropillar possibly inside the pollen tube (probe #6). This is one example where it was impossible to determine whether or not the probe was inside using bright-field microscopy. In this case, it was possible to rotate the micropillar using a permanent magnet and it appeared to be blocking the vesicle streaming.

To have a definitive proof whether micro/nano-probes were internalized, NWs (probe #2) carrying FITC were fabricated using coating approach A. These probes were shot at pollen tubes using particle bombardment at 1550 Psi and later analyzed with the help of a confocal microscope. The plasma membrane was stained using FM 4-64 dye. FM dyes (such as FM 4-64 and 1-43) are non-toxic water-soluble dyes and almost nonfluorescent in aqueous media. This family of dyes can be used to stain a wide variety of membranes structures (such as the plasma membrane and vesicles) that are common in eukaryotic cells, bacteria and plant cells.[3.89] By analyzing the FITC channel (fig. 3.14) it was possible to observe large bright spots inside a pollen tube. These bright spots are small agglomerates of NWs carrying FITC. At first, it looked as if the NWs were completely internalized but after obtaining and analyzing the complete Z-stack it was possible to see that, in fact, the NWs were inside the pollen tube but coming out of the cell wall (incomplete internalization). In

other pollen tubes and grains from the same experiments we only found NWs sticking to the outside of the cell wall.
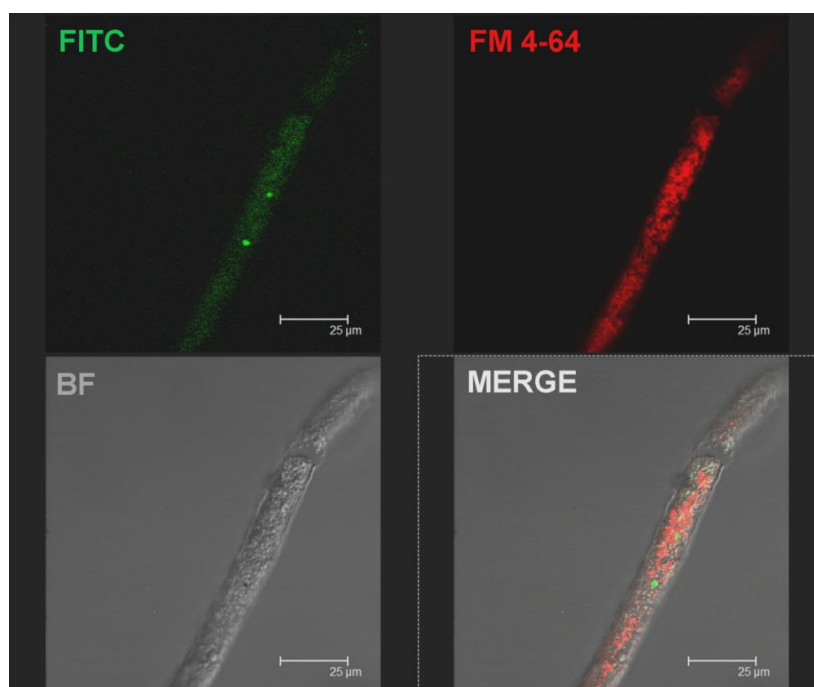
Figure 3.14 Images from a pollen tube after particle bombardment with nanoprobes coated using approach A (probe #2). These images were taken using a confocal microscope. The images shown are from the same slice (around the middle of the tube) of the Z-stack obtained. FM 4-64 (red) stains the plasma membrane as well as some vesicles. The FITC channel shows two bright spots in the middle of the auto-fluorescence background which correspond to bundles of nanoprobes inside the tube. Nevertheless, the 3D image reconstruction obtained from the Z-stack showed that the nanoprobes were not completely internalized.

The particle bombardment method turned out to be a very uncontrollable method, especially for single particle internalization. This method requires a large quantity/concentration of starting particles given its random shooting direction and low transformation yield. 1550 Psi gas pressure gave the best results but still complete internalization of the micro/nano-probes was not confirmed.

3.3.4 Microinjection

To perform microinjection, microcapillaries were produced by using a capillary puller. Different pulling parameters were tested to obtain inner and outer diameters

as small as possible to be compatible with the micro/nano-probes as well as with lily pollen dimensions. The starting point was to use the parameters from the equipment manual (P-2000, Sutter Instrument) and also information from Ergeneman et al.[3.90]

Commercially available microcapillaries were also tested, namely, the Femtotip II sterile injection capillaries with ID / OD = 0.5 / 0.7 μm (Eppendorf). These capillaries were able to poke the pollen grains without hindering their germination but, quite often they would rather bend than puncture them. Besides this, their inner diameter (0.5 μm) is too small for the NWs fabricated using the coating approach B (CoNi@SiO$_2$) and Femtotips are considerably more expensive than the capillaries that were pulled. The cost of each tip makes it a bit unpractical given the large number of tips that are used or get broken. In summary, Femtotips might be more suitable for animal cell injection than for plant cells.

Microinjection was tested on both pollen grains and tubes. Microinjection was first tested by injecting directly into the pollen tube while adherent to agarose, with normal germination medium and also with plasmolysis medium. Injection at the tube with subsequent retraction of the microcapillary led to the death of the pollen tube in some cases or bursting of the tip in a few cases. The main problem here appears to be the fragility and sensitivity of the pollen tube as opposed to the pollen grain. Literature on microinjection at the pollen tube is scarce, being mostly limited to the use of microinjection in the pressure probe technique. In Benkert et al.[3.54], as an example, using the pressure probe technique directly on the tube does not disturb growth (and turgor) simply because the microcapillary is not removed.

Microinjection of micro/nano-probes into pollen grains with posterior tube growth was accomplished successfully (figs. 3.15 and 3.16a)). The overall success rate was less than 20%. This rate is mostly due to the technical difficulties but also accounts for pollen death due to its innate sensitivity to other factors such as the germination conditions (temperature, humidity, light, medium, etc.). Pollen grains were usually injected shortly after germination was noticeable (fig. 3.16a)), since it was observed that, in general, pollen grains that were injected before germination did not to germinate afterwards. The holding and injecting microcapillaries were always placed away from the tube protrusion. Using this procedure allowed the tube

bursting to be avoided, given that the cell wall at the tube is much weaker than the cell wall at the grain.
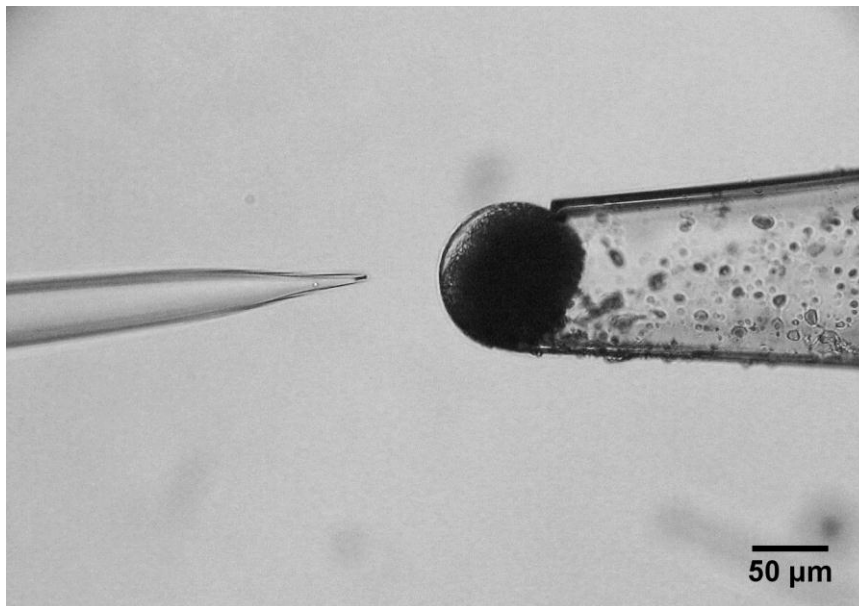
Figure 3.15 Image of the microinjection setup immediately before injection. On the right, the holding capillary is holding the pollen grain. On the left, the injection capillary carries the micro/nano-probes to be injected into the pollen grain.

After perforation, some material from the cytoplasm was ejected into the microcapillary. At that time, the micro/nano-probes were allowed to mix with this material, mostly cytosolic, before reinjection. The removal/retraction of the microcapillary from the pollen grain was also not an easy task. The method used involved dragging the injected grain against another grain until the microcapillary was released due to the friction between the two grains. In some of the experiments the microcapillary tip broke and was left inserted in the cell wall. Even after this occurrence the majority of grains were able to grow and proceed with normal cytoplasmic streaming, without little cytoplasmic material being ejected through the hole. This was presumably due to clog formation on the microcapillary tip: as long as the capillary got clogged before too much cytoplasmic material was ejected tube growth proceeded normally. Prior silanization of the microcapillary is referred in literature as a method to improve the insertion and removal of the capillary.[3.91] This approach was not tested by us but it might well improve our microinjection procedure.

For both cases (with or without microcapillary tip left inserted) tube growth was only seen after no more cytoplasmic material was ejected from the hole created in the pollen grain. This shows that turgor pressure is stabilized by some mechanism, which relies on the hole closure, before tube growth can recommence. The mechanism that leads to hole closure/turgor stabilization was not identified by us but it is possibly a consequence of clog formation or cell wall regeneration. Normal cytoplasmic streaming (vesicle flow) was visible during and after microinjection. Nevertheless, because turgor was destabilized for a certain period of time by the microinjection, in most cases it was possible to observe the formation of kinks ("elbows") and/or changes in the growth direction after microinjection.

Furthermore, it was observed that microinjection using capillaries with an outer diameter larger than 2.5-3 μm led to a premature death of the pollen (fig. 3.16b)). This phenomenon might be due to the inability of hole closure and/or turgor stabilization for holes larger than 2.5-3 μm by the pollen. This finding also presents a limitation to the diameter of the micro/nano-probes that can be used, given the maximum inner diameter of around 1.5-2 μm for the capillaries used.
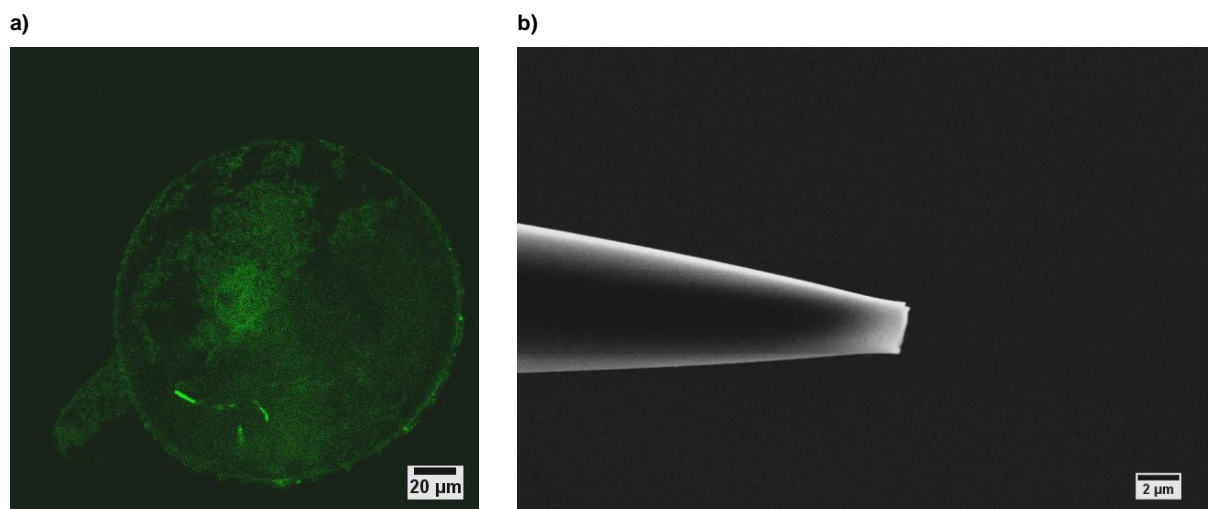
Figure 3.16 a) Image of a pollen grain and tube after injection of nanoprobes (CoNi-(PAH:FITC-PSS)$_4$). It is possible to see the nanoprobes because of the bright FITC fluorescence, even though there is a lot of auto-fluorescence. b) SEM picture of the tip of one of the fabricated injection microcapillaries. The outer diameter is around 2.5 μm.

Micro/nano-probes coated using approach A were first allowed to stream freely once they were inside the pollen tube. It was observed that the probes were

moved along with the cytoplasmic streaming from the pollen grain into the tube and the other way around, in much the same way as the larger vesicles. It was observed that NWs (probe #3) coated using approach A, were moved until the base of the clear zone (subapex) before turning backwards and moving in the direction of the grain (fig. 3.18). NWs most of the times appear to stream by being dragged by the vesicles. This was not understood by us but, one of the following hypotheses might explain this phenomenon:

i.   NWs are sticking to the vesicles: vesicles are dragging the NWs;

ii.   NWs are getting stuck between vesicles: vesicles are pushing forward the NWs;

iii.   NWs are sticking to the actin filaments: NWs are getting coated with myosin and streaming by the same mechanism as vesicles along the actin filaments.

NWs can be manipulated intracellularly to perform rotational or translational movements using the MFG-100-i magnetic manipulation system or by using a permanent magnet. However, most of the time, their movement is constrained due to the interaction with vesicles or other cell organelles.

Because the pollen tubes were allowed to grow for several hours, reaching mm long, callose plug formation was expected to occur at some point. However, no callose plug formation was observed during growth, and this was the case for both injected and non-injected pollen tubes. The absence of callose plug formation might be due to the *in vitro* germination conditions used.[3.37]

3.3.5 Intracellular pH probing

The first developed application was cytoplasmic pH probing of pollen tubes. Intracellular pH (pH_i) plays a critical role in cell function, growth and internalization (among others), in plant and animal cells.[3.61,3.92] For this purpose, the two coating approaches (A & B) were designed to attach FITC molecules to the nanoprobes (probes #3 & #4). FITC was chosen not only because it is a pH-sensitive dye but also because it allows the pH value to be determined using a ratiometric methodology: the ratio between the fluorescent emission (525 nm) measured for two

different excitation wavelengths (485 and 430 nm) has a constant value for each pH.[3.93]

To measure the pH_i value using the ratiometric methodology, a calibration using pH buffers is necessary. The results of this calibration are displayed in fig. 3.17 for micro/nano-probes with both coating approaches. The figure shows a sigmoidal variation of the emission ratio (FITC/CFP) that is dependent on the pH value for both approaches. This result is in accordance with the fluorescent response that is reported in literature for fluorescein compounds on other "carrier" probes.[3.86,3.94,3.95]
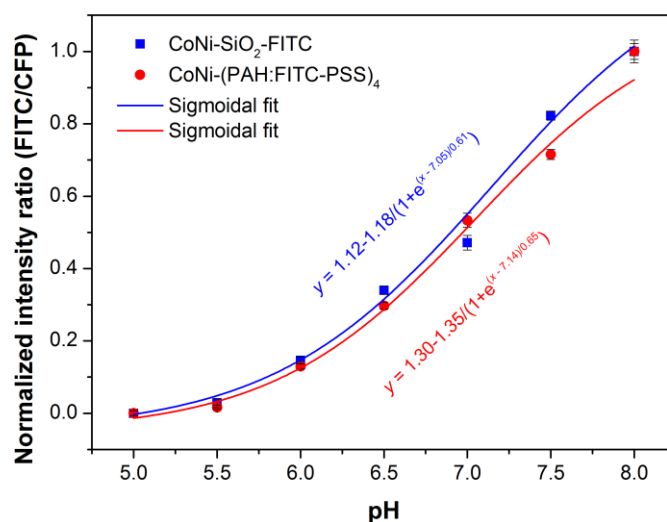
Figure 3.17 Calibration plot of the normalized ratiometric fluorescence intensity as a function of the pH measured with the nanoprobes. The probes used were probe #4 coated using approach B (CoNi-SiO$_2$-FITC) and probe #3 coated using approach A (CoNi-(PAH:FITC-PSS)$_4$).

The pH_i of pollen tubes was determined using the calibration displayed in fig. 3.17. The measurement of the pH_i was done while the probes streamed freely together with the cytoplasmic streaming without magnetic manipulation (fig. 3.18). Changing the orientation of the probe while it was moving with the cytoplasmic streaming was possible using a permanent magnet (data not shown).

The obtained pH_i values were typically between 6.5 and 8, which are in the range of what is reported in literature.[3.32,3.61] The results were obtained while the probes were in the shank and subapical region. It was observed that the pH_i of the

pollen tubes decreased sometimes when the pollen tubes were older or after several measurements were done on the same pollen tube. This cytoplasmic acidification was noticeable by a drop of the pH_i value by over 1 unit. Cytoplasmic acidification is an early sign of apoptosis[3.96] and in our case this might have occurred due to blue light-induced stress[3.97-3.99]., if other causes exist other than the pollen tube's "age". A change in the probe's local microenvironment due to its size/shape might also a possible explanation for the changes in pH_i. The blockage of cytoplasmic material by the probe, possibly independent of whether the probe changed or not its location, may as well explain the changes in pH_i observed in later experiments. It is important to study the intracellular pH because abnormal pH_i values are associated with inappropriate cell function and growth (pathological states), and are observed in some common human diseases such as cancer and Alzheimer's.[3.92]

time
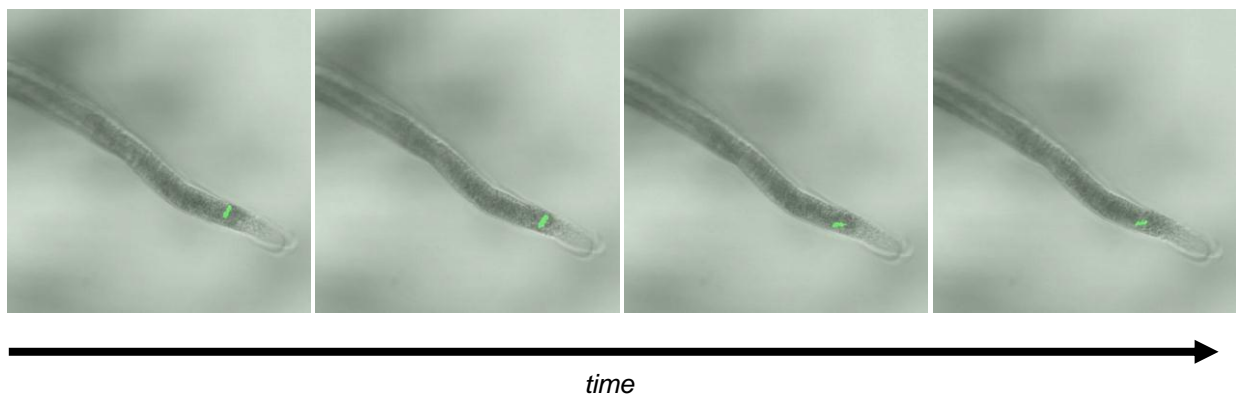
Figure 3.18 Temporal sequence of images of a nanoprobe moving freely with the cytoplasmic streaming. It is possible to observe the nanoprobe moving forward toward the tip, inverting its motion at the subapical region and moving backwards in the direction of the grain. The nanoprobe consisted of a bundle from probe #3 (3 NWs) coated using approach A (CoNi-(PAH:FITC-PSS)$_4$). The total time of this sequence was 40.6 s.

For accurate pH_i measurements, proper background subtraction is essential. Auto-fluorescence is a source of error that affects both ratiometric and non-ratiometric measurements. When using the FITC excitation filter a lot of auto-fluorescence emerges in the cytoplasm which is mostly coming from the vesicles. This means that pollen tubes display auto-fluorescence with an emission spectrum in the same region as FITC. One way to minimize this disturbance would be to use a

pH-sensitive dye that emits fluorescence in different emission wavelengths. Another way to improve the measurements would be to use filters with narrower bandwidths.

FITC is a pH-sensitive dye that allows both ratiometric as well as non-ratiometric pH determination. When using the ratiometric methodology two images must be taken using different excitation filters, which means that there is a time delay between the pictures. This delay which is caused by the filter switch lets the probe change its location in the tube and provides a small source of error in the measurement. Nevertheless, ratiometric pH measurement presents higher accuracy and has several advantages over the non-ratiometric methodology. In the non-ratiometric approach, photobleaching influences the repeatability/reproducibility of the results and also the measurement is sensitive to the size of probes and to the number of fluorophores. The only advantage of the non-ratiometric approach is in fact its measurement speed given that no filter switch is needed.

As mentioned previously, approach B was designed to enable a straightforward conjugation with any kind of sensing molecules (or other types of biomolecules). A different version of this approach can be developed to mix the pH-sensing molecules (FITC or others) in the sol-gel and therefore embed them in the SiO_2 layer. This approach would allow pH sensing[3.93] as well as the addition of a second functionality to the surface (e.g., surfactants, antibodies, etc.) to improve the probe's stability/solubility or to target specific intracellular organelles. Other strategies to measure pH_i exist and can also be tested with our micro/nano-probes using, for instance, Raman active molecules that display a pH-dependent Raman signature.[3.100]

3.3.6 Cytoplasmic nanorheology

Intracellular mechanical properties can be probed as well with our micro/nano-probes by using magnetic manipulation. After microinjection, micro/nano-probes usually get stuck to some vesicles. However, in a few cases, it was possible to release the probes "free" from the vesicles by using rotating them using magnetic fields. When this occurs, it is then possible to move the micro/nano-probes in 3D within the cytoplasm using gradient or rotational magnetic fields.

To perform nanorheological measurements nanoprobes (probe #3) coated by coating approach A were used. In this case, the presence of FITC was not necessary because the measurements were done without fluorescence excitation, using only the bright field imaging mode. Manipulation of the nanoprobes occurred close to the base of the tube, near the grain. Given that this zone is highly vacuolated there was at some point doubt whether we could possibly be doing measurements inside a vacuole. However, this was excluded because not only were the nanoprobes affected by the cytoplasmic streaming but it was also possible to interact with vesicles, which flow only in the cytoplasm.

Rheological measurements were done around the central axis of the pollen tube by manipulating the nanoprobe using gradient magnetic fields (fig. 3.19).
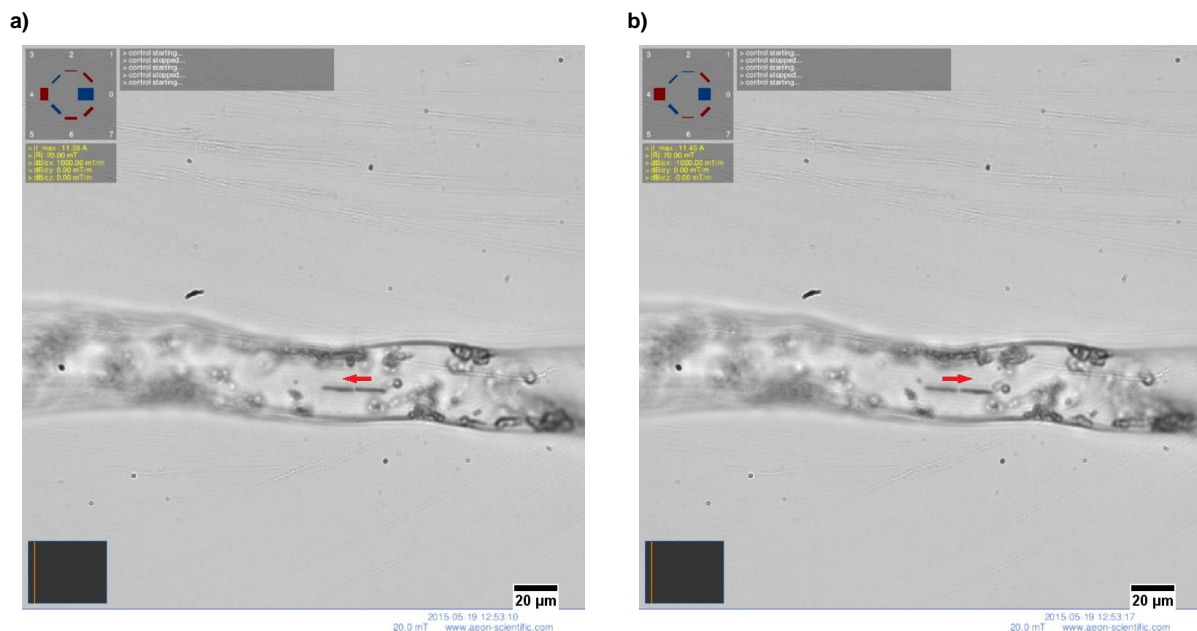
Figure 3.19 Montage of the translational motion of a nanoprobe inside a pollen tube subjected to a magnetic gradient. The nanoprobe is pulled a) backward (away from the tip) and b) forward (toward the tip) relative to the cytoplasmic streaming direction. For each montage, two images at different timepoints were merged into one. In a) there are 2 s apart, and in b) 1 s apart. The red arrow points the direction of probe's motion. $B = 20$ mT, $\nabla B = 1$ T/m, 40x objective

Although the central axis of the pollen tubes is the pathway for the backward motion of vesicles coming from the subapical region ("reverse fountain"), in the area where the measurements were done the backward streaming (toward the grain) was practically null. This was observed by the absence of vesicles moving backwards but

also by the higher velocity of the nanoprobe when moving forward (towards the tip). The measurements consisted of determining the speed of the nanoprobe while moving forward and backward under magnetic manipulation with a constant magnetic field of 20 mT and a magnetic gradient of 1 T/m (fig. 3.19).

The speed of the nanoprobe without the influence of cytoplasmic streaming (relative velocity) and the speed of the cytoplasmic streaming were calculated based on the measurements. The vesicle streaming velocity in the forward direction was also measured for comparison. The obtained values for the different velocities are displayed in table 3.8. The errors reported come from the feature detection errors inherent of the image processing. It was also observed that using a constant magnetic field of only 5 mT was enough to magnetize and move the nanoprobe.

Table 3.8 List of intracellular speeds measured from the pollen tube *in vitro*

	Velocity (μm/s)
Nanoprobe backward velocity	7.4 ± 0.5
Nanoprobe forward velocity	15.8 ± 0.3
Nanoprobe velocity (relative)	4.2 ± 0.4
Cytoplasmic streaming velocity	11.6 ± 0.4
Vesicle streaming velocity	11.7 ± 0.3

By comparing the value obtained for the cytoplasmic streaming with the value measured for the vesicle streaming it is visible that they agree with each other. This shows that the results obtained from the manipulation of the nanoprobe have a good accuracy. The vesicle streaming velocity (11.7 ± 0.3 μm/s) measured is difficult to compare with previous studies, again due to the lack of studies in plants. A study from Yokota et al.[3.101] suggests a maximum speed of 9.8 μm/s for a 170 kDa myosin type. However, this study, which was done in an *in vitro* setup, only tested one myosin type out of the more than 10 myosin types already identified in

Arabidopsis.[3.39] What is important to retain from this result is that the vesicle streaming speed is faster than the pollen growth rate observed (11.7 μm/s vs 20 μm/min). This observation confirms that the cytoplasmic streaming is able to support the fast growth rate of the pollen tube.

From the calculated relative nanoprobe velocity it is possible to extrapolate a value for the viscosity by assuming the cytoplasm as a Newtonian fluid. To make this calculation, first we assume that our nanoprobes are fully magnetized under the magnetic field (20 mT) and thus their effective magnetization has the same value as the magnetic saturation for $Co_{50}Ni_{50}$ ($M_{eff} \approx M_{sat}$ = 680 kA/m).[3.102] We also assume that our probes move in the cytoplasm in a low Reynolds number regime (Re << 1) and their speed is constant ($F = ma = 0$) so that the drag force equals the magnetic force generated ($F_{mag} = F_{drag} = 0$). The nanoprobe used in these experiments consisted on 3 NWs together (2 NWs parallel and a third one in series). Calculating the magnetic force (F_{mag}) using equation 3.5, we obtain:

$$F_{mag} = (3 \cdot V_{NW}) \cdot M_{eff} \cdot \nabla B = 0.701 \text{ pN}$$ (eq. 3.6)

$V_{NW} = 3.4361 \cdot 10^{-19} \text{ m}^3$, volume of one nanowire (probe #3: 0.250 x 7 μm)

$M_{eff} = M_s (Co_{50}Ni_{50}) = 0.680 \text{ MA/m}$, effective magnetization of the nanoprobe

$\nabla B = 1 \text{ T/m}$, applied magnetic gradient

To calculate the viscosity, we first calculate the geometric coefficient for the nanoprobe (β). By using equation 3.3 for a prolate ellipsoid, we get the following:

$$\beta = \frac{2\pi \cdot L}{\ln\left(\frac{L}{2r}\right) + \gamma_{\parallel}} = 2.7817 \cdot 10^{-5} \text{ m}$$ (eq. 3.7)

$L = 14 \mu m$, length of the nanoprobe

$r = 0.250 \mu m$, radius of the nanoprobe

$\gamma_{\parallel} = -0.17$, end correction factor (obtained from reference [3.74])

By assuming that the nanoprobe moves at constant speed (dv/dt=0) in a Newtonian fluid, the drag force equals the magnetic force[3.73] from the following equation:

$$\frac{dv}{dt} = \frac{F_{mag} - F_{drag}}{m} = 0 \Rightarrow F_{drag} = F_{mag}$$ (eq. 3.8)

The cytoplasm of the pollen tube is a complex inhomogeneous fluid. Therefore, given that we have manipulated the nanoprobe to move along the central axis of the tube, we define the obtained viscosity (η) as the viscosity in the direction parallel to the central axis and denote it as $\eta_{\parallel}$. The viscosity $\eta_{\parallel}$ is then calculated by reordering equation 3.2, as follows:

$$\eta_{\parallel} = \frac{F_{drag}}{\beta \cdot v} = 6.0 \pm 0.5 \text{ mPa·s}$$ (eq. 3.9)

$F_{drag} = F_{mag} = 0.701$ pN, drag force acting on the nanoprobe, parallel to the central axis

$\beta = 2.7817 \cdot 10^{-5}$, geometric correction factor

$v = 4.2 \pm 0.4$ µm/s, relative velocity of the nanoprobe, parallel to the central axis

Given that the calculated viscosity $\eta_{\parallel}$ was obtained by probing in the direction parallel to the central axis, this value accounts mainly for the cytosolic mechanical properties (cytosolic viscosity). The cytosolic fluid is viscous/"sticky" because it contains mainly water, ions and dissolved macromolecules.[3.46,3.103] A first glance at the value obtained for $\eta_{\parallel}$ shows that, as expected, the cytosolic viscosity is higher than the viscosity of water (η_{H2O} ~ 1 mPa·s)[3.104] but also higher than the cytoplasmic viscosity typically measured in mammalian cells (~1-3 mPa·s).[3.105-3.107] The obtained value for the cytosolic viscosity is slightly higher than the viscosity of the human blood (~3-4 mPa·s)[3.108] and butterflies' saliva (~4-5 mPa·s) and around the same value as a 35-40% sucrose solution.[3.109]

Although the cytosol behaves as a Newtonian fluid, the other components of the cytoplasm such as the cytoskeleton, organelles and ribosomes, provide an elastic matrix.[3.45] As an example, the mechanical properties of the actin and

microtubule network are determined by the amount of bundles and crosslinkers connecting the filaments. These properties make the pollen tube cytoplasm behave as a viscoelastic material which requires further research using different approaches/methods.[3.110,3.111] The nanoprobe and the manipulation approach used allowed us to probe the micro/nano-scale mechanical properties as opposed to the macroscopic/"bulk" properties.[3.107] To measure the viscoelastic properties of the cytoplasm using the same type of probes, it is necessary to move the probes in different directions, for instance using rotational fields[3.112], and/or using probes with larger sizes that interact with the whole range of cytoplasmic components. Rotational magnetic spectroscopy is unavailable if a nanoparticle-based probe is used instead of a nanowire-based one. Using the MFG-100-i magnetic manipulation system with our nanoprobe, it is possible to generate torques in the range of fN·m. Another approach to measure viscoelasticity is to use, for instance, a photoacoustic technique.[3.110] Using our micro/nano-probes it is also possible to measure viscosity, for instance, by conjugating a viscosity-sensitive dye onto a probe's surface.[3.113]

3.4 Conclusions

We have reported for the first time the development of a nanowire-based magnetically maneuverable probe, its intracellular injection and application on pH sensing and in rheological measurements inside single pollen tubes. The developed micro/nano-probes allow manipulation and measurements to be done in real time using a magnetic manipulation system.

3.4.1 Fabrication, functionalization and conjugation of the micro/nano-probes

Micro/nano-probes were developed to enable intracellular biochemical and mechanical measurements. As is described in Chapter 1, template-assisted electrodeposition is a powerful and versatile process to produce nanowires from many different materials. CoNi provided enough effective magnetization for the manipulation experiments to be successful. Both the sol-gel and layer-by-layer

methods are facile and controllable coating processes. The silanization process adds versatility to the sol-gel approach (approach B), whereas the layer-by-layer method is overall a faster method (approach A). Conjugation in approach A was achieved using a commercially FITC-conjugated polyelectrolyte (PAH:FITC). In approach B, FITC was conjugated through amine-carboxyl coupling. Using coating approach A, micro/nano-probes were fabricated as $CoNi-(PAH:FITC-PSS)_4$, whereas using coating approach B, the fabricated micro/nano-probes consisted of $CoNi-SiO_2-FITC$.

3.4.2 Internalization/transformation methods

To internalize the probes into the pollen, common plant transformation methods were tested using micro/nano-probes of different sizes. Although the particle bombardment method is widely used in plant transformation, it is not the most controllable one. Complete internalization could not be confirmed using this method. In other methods such as centrifugation, magnetic spearing and magnetic poking, internalization was not confirmed as well. Internalization was successful using the microinjection method on pollen grains immediately after germination. The microcapillary sizes that do not hinder the growth restart of the pollen tube after microinjection were found to be the ones with outer diameters (OD) smaller than 2.5-3 μm and inner diameters (ID) smaller than 1.5-2 μm, respectively. Micro/nano-probes with diameters smaller or equal to 1.1 μm could be internalized without any major adverse reaction from the pollen.

3.4.3 Applications and results

Magnetic nanoprobes were fabricated to allow intracellular pH measurements in single pollen tubes (probes #3 & #4). Both coating approaches used (approaches A & B) contained FITC as the pH-sensitive dye. By using a ratiometric methodology, the obtained pH_i ranged from 6.5 to 8, which is in agreement with the available literature. Decreased pH_i ($pH_i < 6.5$) was also detected in pollen tubes possibly due to the tube's age, blue light-induced stress or changes in the probe's local microenvironment.

The same kind of nanoprobes was used to probe the mechanical properties of the cytoplasm of the pollen tubes. Using magnetic gradients to move the nanoprobes at 4.2 ± 0.4 μm/s (relative velocity) it was possible to measure the viscosity of the cytosol, assuming a mechanical behavior as a Newtonian fluid. The value obtained for the cytosolic viscosity was 6.0 ± 0.5 mPa·s, which is higher than the value for the human blood but around the same value as a 35-40% sucrose solution. The calculated value for the cytoplasmic streaming was 11.6 ± 0.4 μm/s, which proves to be sufficient supporting the fast growth rate of the lily pollen tube (~20 μm/min). MFG-100-i provided magnetic gradients and fields that were sufficient to conduct the manipulation experiments ($\nabla B = 1$ T/m, $B = 20$ mT). Rotational fields were also effective in rotating the nanoprobes inside the pollen tube (data not shown) and thus can provide the basis for the measurement of intracellular viscoelastic properties.

3.4.4 Remarks and future work

The work reported in this chapter shows the application of functional micro/nano-probes as a proof of concept of intracellular pH probing and intracellular rheological measurements. The reported probes were developed for the application in pollen tubes. Nevertheless, these probes can be used in other type of plant cells or even in cells from different kingdoms or domains. The developed micro/nano-probes are good candidates for real time *in vivo* experiments because they can be used as a diagnostic tool or as a wirelessly controllable robot capable of tissue actuation/repair, drug delivery or other biomedical applications.

The developed micro/nano-probes constitute a versatile framework that allows biomolecules to be conjugated in a straightforward way. Using magnetic nanowire-based probes instead of magnetic nanoparticles has several advantages. Magnetic nanowires provide the possibility of performing rheological measurements using gradient fields but also using rotational fields. Nanowires can block the movement of intracellular components (e.g., vesicles) or disturb the cytoplasmic streaming due to their shape, which would be very difficult to do using nanoparticles.

Measuring intracellular mechanical properties has similar importance than determining intracellular biochemical properties. Only by combining information from these two domains it is possible to fully understand cell function, growth and

pathology. The developed micro/nano-probes allow measurements to be performed with minimal disturbance of the cell function. This technique presents advantages for rheological measurements, for instance, because it does not require contact with the cell surface, as opposed to what occurs in other rheological methods such as using AFM or parallel plate rheometers. The size of the probes is another advantage that enables rheological measurements to be done with a finer accuracy when compared to other techniques which only assess macro/"bulk" properties.

The micro/nano-probes presented in this chapter have an immense potential for studying plant cells as well as for other applications. One question that is still under debate, where these probes can play an important part, is regarding the role of microtubules in pollen tubes. These micro/nano-probes can be conjugated with antibodies to interact with specific intracellular components such as actin, microtubules, etc., and uncover unknown features by doing localized manipulation. Regarding the rheological measurements, these should be confirmed by using other methodologies such as magnetic rotational spectroscopy and/or using, for instance, viscosity-sensitive fluorophores. The micro/nano-probes can also be used to probe intracellular changes while the pollen tube is subjected to external actuation (e.g. indentations at the cell wall). In an opposite manner, the pollen tube can be actuated intracellularly using the micro/nano-probes while measuring changes in tube growth (e.g. using a force sensor). These probes are ideal for blocking certain cellular mechanisms, such as ionic gradients or disturbing the cytoplasmic streaming, and observing the effects on tube growth. Owing to their size and versatility, the micro/nano-probes can be used to mimic plant pathogens and study their interactions with the host. Other internalization/transformation methods could also be tested such as the cell wall digestion using enzymes attached to the surface of the micro/nano-probes.

3.5 Bibliography

[3.1] P.H. Raven, R.F. Evert and S.E. Eichhorn, 1992, "Biology of Plants", New York: Worth Publishers, ISBN: 9780879015329;

[3.2] E.M. Meyerowitz, 2002, "Plants Compared to Animals: The Broadest Comparative Study of Development", *Science*, 295, 1482-1485;

[3.3] J. Yablonski, 2005, "Plant and Animal Cells: Understanding the Differences Between Plant and Animal Cells", The Rosen Publishing Group, ISBN: 9781404203242;

[3.4] W.P. Armstrong, 2001, "Wayne's Word: An Online Textbook of Natural History", available at http://waynesword.palomar.edu/index.htm;

[3.5] a) J.T. Connelly et al., 2010, "Actin and serum response factor transduce physical cues from the microenvironment to regulate epidermal stem cell fate decisions", *Nature Cell Biology*, 12(7), 711-718. b) C.S. Chen et al., 1997, "Geometric Control of Cell Life and Death", *Science*, 276, 1425;

[3.6] G.C. Gurtner et al., 2007, "Progress and potential for regenerative medicine". *Annu. Rev. Med.*, 58, 299–312;

[3.7] J.D. Humphrey et al., 2014, "Mechanotransduction and extracellular matrix homeostasis", *Molecular Cell Biology*, 15, 802-812;

[3.8] C. Bechinger et al., 1999, "Optical Measurements of Invasive Forces Exerted by Appressoria of a Plant Pathogenic Fungus", *Science*, 285(5435), 1896-1899;

[3.9] F. Arai et al., 1999, "Micro Tripaxial Force Sensor for 3D Bio-Micromanipulation", *Proceedings of the 1999 IEEE International Conference on Robotics & Automation,* 2744-2749;

[3.10] S. Gus-Mayer et al., 1998, "Local mechanical stimulation induces components of the pathogen defense response in parsley", *Proc. Natl. Acad. Sci. USA*, 95, 8398–8403;

[3.11] S. Suresh, 2007, "Nanomedicine: Elastic clues in cancer detection", *Nat. Nanotechnol.*, 2, 748-749;

[3.12] D. Felekis et al., 2015, "Real-time automated characterization of 3D morphology and mechanics of developing plant cells", *The International Journal of Robotics Research*, 34(8), 1136-1146;

[3.13] A. Menciassi et al., 2003, "Force Sensing Microinstrument for Measuring Tissue Properties and Pulse in Microsurgery", *IEEE/ASME Transactions on Mechatronics*, 8(1), 10-17;

[3.14] H. Wang et al., 2014, "3D Assembly of Cellular Structures with Coordinated Manipulation by Rail-guided Multi-microrobotic System", *2014 IEEE International Conference on Robotics and Automation (ICRA)*, 2813-2818;

[3.15] Y. Sun et al., 2003, "Mechanical Property Characterization of Mouse Zona Pellucida", *IEEE Transactions on NanoBioscience*, 2(4), 279-186;

[3.16] S. Schuerle et al., 2013, "Three-Dimensional Magnetic Manipulation of Micro- and Nanostructures for Applications in Life Sciences", *IEEE Transactions on Magnetics*, 49(1), 321-330;

[3.17] N.L. Rosi et al., 2006, "Oligonucleotide-Modified Gold Nanoparticles for Intracellular Gene Regulation", *Science*, 312, 1027-1030;

[3.18] J. Gao et al., 2008, "Intracellular Spatial Control of Fluorescent Magnetic Nanoparticles", *J. Am. Chem. Soc.*, 130, 3710-3711;

[3.19] S. Deka et al., 2009, "CdSe/CdS/ZnS Double Shell Nanorods with High Photoluminescence Efficiency and Their Exploitation As Biolabeling Probes", *J. Am. Chem. Soc.*, 131(8), 2948-2958;

[3.20] B. van den Broek et al., 2013, "Parallel Nanometric 3D Tracking of Intracellular Gold Nanorods Using Multifocal Two-Photon Microscopy", *Nano Lett.*, 13, 980−986;

[3.21] J.H.F. Bothwell et al., 2006, "Biolistic delivery of Ca^{2+} dyes into plant and algal cells", *The Plant Journal*, 46, 327–335;

[3.22] J.L. Vivero-Escoto et al., 2010, "Mesoporous Silica Nanoparticles for Intracellular Controlled Drug Delivery", *Small*, 6(18), 1952–1967;

[3.23] H. Wang and L. Jiang, 2011, "Transient expression and analysis of fluorescent reporter proteins in plant pollen tubes", *Nature Protocols*, 6(4), 419-426;

[3.24] E. Corredor et al., 2009, "Nanoparticle penetration and transport in living pumpkin plants: in situ subcellular identification", *BMC Plant Biology*, 9, 45;

[3.25] F. Torney et al., 2007, "Mesoporous silica nanoparticles deliver DNA and chemicals into plants", *Nature Nanotechnology*, 2, 295-300;

[3.26] A.Y. Cheung, 2001, "Imaging elongating pollen tubes by green fluorescent protein", *Sex Plant Reprod*, 14, 9-14;

[3.27] L. Vidali and P.K. Hepler, 2001, "Actin and pollen tube growth", *Protoplasma*, 215, 64-76;

[3.28] Ö. Dalgiç and F. Dane, 2005, "Some of the Molecular Mechanisms of Pollen Tube Growth and Guidance", *Asian Journal of Plant Sciences*, 4(6), 702-710;

[3.29] A.Y. Cheung and H. Wu, 2008, "Structural and Signaling Networks for the Polar Cell Growth Machinery in Pollen Tubes", *Annu. Rev. Plant Biol.*, 59, 547–72;

[3.30] A. Krichevsky et al., 2007, "How pollen tubes grow", *Developmental Biology*, 303, 405–420;

[3.31] C.M. Rounds and M. Bezanilla, 2013, "Growth Mechanisms in Tip-Growing Plant Cells", *Annu. Rev. Plant Biol.*, 64,243–65;

[3.32] H.-J. Wang et al., 2010, "Pollen Germination and Tube Growth", *Advances in Botanical Research*, 54, 1-52;

[3.33] T. Dresselhaus and S. Sprunck, 2012, "Plant Fertilization: Maximizing Reproductive Success", *Current Biology*, 22(12), R487-R489;

[3.34] N. Eckardt, 2005, "VANGUARD1-At the Forefront of Pollen Tube Growth", *Plant Cell*, 17, 327-329;

[3.35] H. Takeuchi and T. Higashiyama, 2011, "Attraction of tip-growing pollen tubes by the female gametophyte", *Current Opinion in Plant Biology*, 14, 614–621;

[3.36] P.K. Hepler et al., 2001, "Polarized Cell Growth in Higher Plants", *Annu. Rev. Cell Dev. Biol.*, 17, 159-87;

[3.37] S. Kim et al., 2004, "Pollen Tube Guidance: The Role of Adhesion and Chemotropic Molecules", *Current Topics in Developmental Biology*, 61, 61-79;

[3.38] L.P. Taylor and P.K. Hepler, 1997, "Pollen Germination and Growth", *Annu. Rev. Plant Physiol. Plant Mol. Biol.*, 48, 461–91;

[3.39] P.K. Hepler and L.J. Winship, 2015, "The pollen tube clear zone: Clues to the mechanism of polarized growth", *Journal of Integrative Plant Biology*, 57(1), 79-92;

[3.40] J. Bove et al., 2008, "Magnitude and Direction of Vesicle Dynamics in Growing Pollen Tubes Using Spatiotemporal Image Correlation Spectroscopy and Fluorescence Recovery after Photobleaching", *Plant Physiol.*, 147, 1646-1658;

[3.41] G. Cai and M. Cresti, 2009, "Organelle motility in the pollen tube: a tale of 20 years", *Journal of Experimental Botany*, 60(2), 495–508;

[3.42] E.R. Rojas et al., 2011, "Chemically Mediated Mechanical Expansion of the Pollen Tube Cell Wall", *Biophysical Journal*, 101, 1844-1853;

[3.43] L. Zonia and T. Munnik, 2008, "Vesicle trafficking dynamics and visualization of zones of exocytosis and endocytosis in tobacco pollen tubes", *Journal of Experimental Botany*, 59(4), 861–873;

[3.44] J. Derksen et al., 1995, "Regulation of pollen tube growth", *Acta Bot. Neerl.*, 44(2), 93-119;

[3.45] L. Zonia et al., 2006, "Hydrodynamics and Cell Volume Oscillations in the Pollen Tube Apical Region are Integral Components of the Biomechanics of Nicotiana tabacum Pollen Tube Growth", *Cell Biochemistry and Biophysics*, 46, 209-232;

[3.46] A.B. Fulton, 1982, "How Crowded Is the Cytoplasm?", *Cell*, 30, 345-347;

[3.47] K. Luby-Phelps, 1999, "Cytoarchitecture and Physical Properties of Cytoplasm: Volume, Viscosity, Diffusion, Intracellular Surface Area", *International Review of Cytology*, 192, 189-221;

[3.48] G. Cai and M. Cresti, 2010, "Microtubule motors and pollen tube growth - still an open question", *Protoplasma*, 247, 131-143;

[3.49] J.-C. Mollet et al., 2013, "Cell Wall Composition, Biosynthesis and Remodeling during Pollen Tube Growth", *Plants*, 2, 107-147;

[3.50] E. Onelli and A. Moscatelli, 2013, "Endocytic Pathways and Recycling in Growing Pollen Tubes", *Plants*, 2, 211-229;

[3.51] S.T. McKenna et al., 2009, "Exocytosis Precedes and Predicts the Increase in Growth in Oscillating Pollen Tubes", *The Plant Cell*, 21, 3026–3040;

[3.52] D.S. Domozych et al., 2013, "Polar Expansion Dynamics in the Plant Kingdom: A Diverse and Multifunctional Journey on the Path to Pollen Tubes", *Plants*, 2, 148-173;

[3.53] R. Malhó (ed.), 2006, "The Pollen Tube – A Cellular and Molecular Perspective", Springer Berlin Heidelberg, ISBN: 9783540342762;

[3.54] R. Benkert et al., 1997, "The turgor pressure of growing lily pollen tubes", *Protoplasma*, 198, 1-8;

[3.55] H. Vogler et al., 2013, "The pollen tube: a soft shell with a hard core", *The Plant Journal*, 73, 617–627;

[3.56] E. Lord, 2000, "Adhesion and cell movement during pollination: cherchez la femme", *Trends in Plant Science*, 5(9), 368-373;

[3.57] J.H. Kroeger et al., 2011, "Regulator or Driving Force? The Role of Turgor Pressure in Oscillatory Plant Cell Growth", PloS ONE, 6(4), e18549;

[3.58] Y. Qin and Z. Yang, 2011, "Rapid tip growth: Insights from pollen tubes", *Seminars in Cell & Developmental Biology*, 22, 816– 824;

[3.59] S. Romagnoliet al., 2003, "*In vitro* assays demonstrate that pollen tube organelles use kinesin-related motor proteins to move along microtubules", *Plant Cell*, 15, 251–269;

[3.60] F.B. Daher and A. Geitmann, 2011, "Actin is Involved in Pollen Tube Tropism Through Redefining the Spatial Targeting of Secretory Vesicles", *Traffic*, 12, 1537-1551;

[3.61] J.A. Feijó et al., 2001, "Cellular oscillations and the regulation of growth: the pollen tube paradigm", *BioEssays*, 23, 86-94;

[3.62] S. Eapen, 2011, "Pollen grains as a target for introduction of foreign genes into plants: an assessment", *Physiol Mol Biol Plants*, 17(1), 1-8;

[3.63] D.D. Songstad et al., 1995, "Advances in alternative DNA delivery techniques", *Plant Cell, Tissue and Organ Culture*, 40, 1-15;

[3.64] B. Huang, 1992, "Genetic Manipulation of Microspores and Microspore-derived Embryos", *In Vitro Cell. Dev. Biol.*, 28P, 53-58;

[3.65] K.H. Khan, 2010, "Gene Transfer Technologies and their Applications: Roles in Human Diseases", *Asian J. Exp. Biol. Sci.*, 1(1), 208-218;

[3.66] A.M. Husaini et al., 2010, "Vehicles and ways for efficient nuclear transformation in plants", *GM Crops*, 1:5, 276-287;

[3.67] P.-H. Wu et al., 2012, "High-throughput ballistic injection nanorheology to measure cell mechanics", *Nature Protocols*, 7(1), 155-170;

[3.68] Y. Shen and T. Fukuda, 2014, "State of the art: micro-nanorobotic manipulation in single cell analysis", *Robotics and Biomimetics*, 1:21;

[3.69] K.J. Oparka et al., 1991, "Modification of the pressure-probe technique permits controlled intracellular microinjection of fluorescent probes", *Journal of Cell Science*, 98, 539-544;

[3.70] E. Lauga and T.R. Powers, 2009, "The hydrodynamics of swimming Microorganisms", *Rep. Prog. Phys.*, 72, 096601;

[3.71] E.M. Purcell,1977, "Life at low Reynolds number", *Am. J. Phys.*, 45, 3–11;

[3.72] P. Fischer and A. Ghosh, 2011, "Magnetically actuated propulsion at low Reynolds numbers: towards nanoscale control", *Nanoscale*, 3, 557–563;

[3.73] J.A. Cribb et al., 2010, "Cylinders vs. Spheres: Biofluid Shear Thinning in Driven Nanoparticle Transport", *Annals of Biomedical Engineering*, 38(11), 3311-3322;

[3.74] M.M. Tirado and J.G. de la Torre, 1979, "Translational friction coefficients of rigid, symmetric top macromolecules. Application to circular cylinders", *The Journal of Chemical Physics*, 71, 2581;

[3.75] M.P. Kummer et al., 2010, "OctoMag: An Electromagnetic System for 5-DOF Wireless Micromanipulation", IEEE Transactions on Robotics, 26(6), 1006-1017;

[3.76] T.H. Boyer, 1988, "The force on a magnetic dipole," *Amer. J. Phys.*, 56(8), 688–692;

[3.77] D. Cai et al., 2005, "Highly efficient molecular delivery into mammalian cells using carbon nanotube spearing", *Nature Methods*, 2(6), 449-454;

[3.78] J. Schindelin et al., 2012, ""Fiji: an open-source platform for biological-image analysis", *Nature methods*, 9(7), 676-682;

[3.79] Y. Furukawa et al., 2013, "Monitoring neural stem cell differentiation using PEDOT–PSS based MEA", *Biochimica et Biophysica Acta*, 1830,4329-4333;

[3.80] J.S. Martinez et al., 2011, "Cytotoxicity of Free versus Multilayered Polyelectrolytes", *Biomacromolecules*, 12, 4063−4070;

[3.81] B. Jang et al., 2015, "Undulatory Locomotion of Magnetic Multilink Nanoswimmers", *Nano Lett.*, 15(7), 4829–4833;

[3.82] a) Q. Liu et al., 1998, "A Novel Two-Step Silica-Coating Process for Engineering Magnetic Nanocomposites", *Chem. Mater.*,10, 3936-3940. b) B. Korzeniowska et al., 2013, "Silica nanoparticles for cell imaging and intracellular sensing", *Nanotechnology*, 24, 442002;

[3.83] W. Fu et al., 2005, "Preparation and characteristics of core–shell structure nickel/silica nanoparticles", *Colloids and Surfaces A: Physicochem. Eng. Aspects*, 262, 71–75;

[3.84] I. Pastoriza-Santos et al., 2006, "Silica-Coating and Hydrophobation of CTAB-Stabilized Gold Nanorods", *Chem. Mater.*, 18, 2465-2467;

[3.85] J.A. Howarter and J.P. Youngblood, 2006, "Optimization of Silica Silanization by 3-Aminopropyltriethoxysilane", *Langmuir*, 22, 11142-11147;

[3.86] Y. Zhang et al., 2009, "Magnetic nanocomposites of Fe_3O_4/SiO_2-FITC with pH-dependent fluorescence emission", *Chinese Chemical Letters*, 20, 969–972;

[3.87] M.F. Morks and A. Kobayashi, 2008, "Development of ZrO_2/SiO_2 bioinert ceramic coatings for biomedical application", Journal of the Mechanical Behavior of Biomedical Materials, 1, 165-171;

[3.88] P. Huang et al., 2011, "Folic acid-conjugated Silica-modified gold nanorods for X-ray/CT imaging-guided dual-mode radiation and photo-thermal therapy", *Biomaterials*, 32, 9796-9809;

[3.89] S. Bolte et al., 2004, "FM-dyes as experimental probes for dissecting vesicle trafficking in living plant cells", *Journal of Microscopy*, 214(2), 159-173;

[3.90] O. Ergeneman et al., 2011, "Characterization of Puncture Forces for Retinal Vein Cannulation", *J. Med. Devices*, 5(4), 044504;

[3.91] P. Scherp and K.H. Hasenstein, 2003, "Microinjection – A Tool to Study Gravitropism", *Adv. Space Res.*, 31(10), 2221-2227;

[3.92] J. Han and K. Burgess, 2009, "Fluorescent Indicators for Intracellular pH", *Chemical Reviews*, 110(5), 2709-2728;

[3.93] J. Asselin et al., 2014, "Supported core–shell nanobiosensors for quantitative fluorescence imaging of extracellular pH", *Chem. Commun.*, 50, 13746;

[3.94] E. Lanz et al., 1997, "Use of FITC as a Fluorescent Probe for Intracellular pH Measurement", *Journal of Fluorescence,* 7(4), 317-319;

[3.95] R.V. Benjaminsen et al., 2011, "Evaluating Nanoparticle Sensor Design for Intracellular pH Measurements", *ACS Nano*, 5(7), 5864-5873;

[3.96] M. Bosch and V.E. Franklin-Tong, 2007, "Temporal and spatial activation of caspase-like enzymes induced by self-incompatibility in Papaver pollen", *PNAS*, 104(46), 18327-18332;

[3.97] F. Wen et al., 2012, "A Protein Phosphatase 2A Catalytic Subunit Modulates Blue Light-Induced Chloroplast Avoidance Movements through Regulating Actin Cytoskeleton in Arabidopsis", *Plant Cell Physiol.*, 53(8); 1366–1379;

[3.98] D.I. Lytvyn et al., 2010, "UV-B overexposure induces programmed cell death in a BY-2 tobacco cell line", *Environmental and Experimental Botany*, 68, 51-57;

[3.99] W.R. Briggs and E. Huala, 1999, "Blue-light photoreceptors in higher plants", *Annu. Rev. Cell Dev. Biol.*, 15, 33-62;

[3.100] S. Zong et al., 2011, "Intracellular pH Sensing Using p-Aminothiophenol Functionalized Gold Nanorods with Low Cytotoxicity", *Anal. Chem.*, 83, 4178-4183;

[3.101] E. Yokota and T. Shimmen, 1994, "Isolation and characterization of plant myosin from pollen tubes of lily", *Protoplasma*, 177, 153-162;

[3.102] O. Ergeneman et al., 2013, "Cobalt-nickel microcantilevers for biosensing", *Journal of intelligent material systems and structures*, 24(18), 2215-2220;

[3.103] G. Késmárky et al., 2008, "Plasma viscosity: A forgotten variable", *Clinical Hemorheology and Microcirculation*, 39, 243–246;

[3.104] M.J. Holmes et al., 2011, "Temperature dependence of bulk viscosity in water using acoustic spectroscopy", *Journal of Physics: Conference Series*, 269, 012011;

[3.105] K. Fushimi and A.S. Verkman, 1991, "Low Viscosity in the Aqueous Domain of Cell Cytoplasm Measured by Picosecond Polarization Microfluorimetry", *The Journal of Cell Biology*, 112(4), 719-725;

[3.106] A.M. Mastro et al., 1984, "Diffusion of a small molecule in the cytoplasm of mammalian cells", *Proc. Natl. Acad. Sci. USA*, 81, 3414-3418;

[3.107] T. Kalwarczyk et al., 2011, "Comparative Analysis of Viscosity of Complex Liquids and Cytoplasm of Mammalian Cells at the Nanoscale", *Nano Lett.*, 11, 2157-2163;

[3.108] R.S. Rosenson et al., 1996, "Distribution of blood viscosity values and biochemical correlates in healthy adults", *Clinical Chemistry*, 42(8), 1189-1195;

[3.109] A. Tokarev et al., 2013, "Probing viscosity of nanoliter droplets of butterfly saliva by magnetic rotational spectroscopy", *Appl. Phys. Lett.*, 102, 033701;

[3.110] J. Li et al., 2008, "Cell viscoelastic characterization using photoacoustic measurement", *Journal of Applied Physics*, 104, 034702;

[3.111] G.B. Thurston and N.M. Henderson, 2006, "Effects of flow geometry on blood viscoelasticity", *Biorheology*, 43, 729-746;

[3.112] A. Tokarev et al., 2012, "Magnetic Rotational Spectroscopy with Nanorods to Probe Time-Dependent Rheology of Microdroplets", *Langmuir*, 28(26), 10064-10071;

[3.113] K. Luby-Phelps et al., 1993, "A Novel Fluorescence Ratiometric Method Confirms the Low Solvent Viscosity of the Cytoplasm", *Biophysical Journal*, 65, 236-242.

Chapter 4

Summary and Outlook

This dissertation reports the research done on magnetic micro/nano-structures with the objectives of the development of biomedical applications and the acquisition of biomechanical parameters in plant cells.

One of the major contributions of this thesis was the exploration of the properties of porous alumina that enable this material to be used in different biomedical applications. It is well known that alumina is a bioinert material. On the other hand, the bioactive properties of porous alumina *per se* (as-produced) are greatly unexplored in literature. In this thesis, fibroblast cultures helped to highlight the non-cytotoxic and biocompatible features of porous alumina templates as-produced and in the form of Fe@C NWs / AAO nanocomposites. As future work, the reported devices should be tested with tissue material *ex vivo*, for instance, and later *in vivo* using animal models. These devices can be tested for biocompatibility as an implant as well as for drug release and biosensing.

By using porous alumina as templates for nanofabrication it was also reported the fabrication of Fe@C magnetic nanocarriers that were functionalized and loaded with drugs (e.g., Doxorubicin, as an anti-cancer drug). The next step towards a drug delivery application to humans would be to test the nanocarriers in a human tumor xenograft, for instance, using transplantable tumors in mice.

Another major contribution of this thesis was the measurement of cell properties using a novel way to probe intracellularly single plant cells. It was demonstrated that it is possible to inject micro/nano-probes in pollen tubes without hindering their growth. Moreover, real-time magnetic manipulation of these probes was achieved and biochemical and mechanical parameters can be acquired at the

same time (pH, viscosity, etc.). The reported work opens the door to new and exciting research possibilities in plant biology. More interestingly is the fact that the developed methods have the potential to be also applied in the study of animal cells. The developed micro/nano-probes consisted on core-shell structures, with a magnetic core (CoNi) and a functional coating (silanized silica or polymer coating). This structure provides a framework that is stable and that has facile biomolecule conjugation possibilities. Future work should involve exploring other intracellular properties. As referred before, using rotational motion of the probes can help deciphering the non-Newtonian behavior of the cytoplasm. Using different biomolecules at the probe's surface (e.g., antibodies and enzymes) can facilitate the manipulation of certain targets, such as the actin or microtubule network, calcium levels or intracellular organelles, and thus provide a deeper understanding of pollen's growth mechanisms. The different zones of the pollen tube should be taken into account and individual conclusions shall be made for each zone separately. Using these probes to simulate plant pathogens would also be a great achievement in order to shed some light on the host-pathogen interactions in plants. As mentioned before, the developed probes can be used in other plant species as well as in animal models such as the fruit fly (*D. melanogaster*) or the zebrafish *(D. rerio)*.

Curriculum Vitae

ANDRÉ LINDO

PERSONAL DETAILS

Date of birth: 26th of October, 1985
Citizenship: Portuguese (EU)

EDUCATION

01/2011-present   **PhD in Basic and Applied Biology (GABBA program)**
                    University of Porto (Portugal) and ETH Zürich (Switzerland)

09/2003-12/2010   **BSc and MEng in Physics Engineering**
                    University of Aveiro (Portugal)

EXPERIENCE

10/2011-06/2015   **Research Assistant**
                    Multi-Scale Robotics Lab (MSRL)
                    ETH Zürich (Switzerland)

01/2010-12/2010   **Research Affiliate**
                    Bio-Inspired Physics Group
                    University of Aveiro (Portugal)

SCHOLARSHIPS

01/2011-12/2014   **GABBA Program 4-year PhD scholarship**
                     ICBAS – University of Porto (Portugal)
                     http://gabba.up.pt

SKILLS

Technical   Micro/nano-fabrication (3D Laser Lithography, Electrochemical and deposition methods), Light and Electron Microscopy, Spectroscopy techniques, cell culture of pathogenic microorganisms, sample preparation for electron microscopy, biofilm growth, plant transformation methods

IT   Programming and mathematical modeling (MATLAB, C, etc.)
               Statistics and Data analysis (SPSS, Origin, MS Excel)
               Web design and Image processing (Dreamweaver, Photoshop, ImageJ, HTML)
               3D modeling (AutoCAD)

Language   Portuguese (native), English (fluent), Spanish (intermediate), French (intermediate), German (basic)

LIST OF PUBLICATIONS

A.M. Lindo, N. Shamsudhin, T. Yamilov, G. Chatzipirpiridis, R. Grisch, B.J. Nelson and S. Pané, "CuNi segmented helices for biomedical applications", *in preparation*.

I.A. Vizcarra, S. Schuerle, **A.M. Lindo**, P. Kollmannsberger, I. Schön, M.S. Sakar, S. Pané, B.J. Nelson and V. Vogel, "Wiggling and arm-twisting between bacteria-mimetic magnetic particles and macrophages: how can the prey escape?", *in preparation*.

S. Schürle, I.A. Vizcarra, J. Moeller, M.S. Sakar, B. Özkale, **A.M. Lindo**, F. Mushtaq, I. Schön, S. Pané, V. Vogel and B.J. Nelson, "3D magnetic micromanipulation of spherical and non-spherical prey resolves mechanical transition from phagocytic migration to engulfment", *in preparation.*

F. Mushtaq, M. Guerrero, M.S. Sakar, M. Hoop, **A.M. Lindo**, J. Sort, X. Chen, B.J. Nelson, E. Pellicer and S. Pané, "Magnetically Driven $BiOCl/Bi_2O_3$-Based Hybrid Microrobots for Photocatalytic Water Remediation", *in preparation.*

A.M. Lindo, E. Pellicer, M.A. Zeeshan, R. Grisch, F. Qiu, J. Sort, M.S. Sakar, B.J. Nelson and S. Pané, 2015, "The biocompatibility and anti-biofouling properties of magnetic core-multishell Fe@C NWs/AAO nanocomposites", *Physical Chemistry Chemical Physics*, 17, 13274-13279;[1]

M.A. Zeeshan, S. Pané, S.K. Youn, E. Pellicer, S. Schuerle, J. Sort, S. Fusco, **A.M. Lindo**, H.G. Park and B.J. Nelson, 2013, "Graphite coating of iron nanowires for nanorobotic applications: synthesis, characterization and magnetic wireless manipulation", *Advanced Functional Materials*, 23(7), 823-831;[1]

A.M. Lindo, B.F. Faria and F.V. Abreu, 2011, "Tunable kinetic proofreading in a model with molecular frustration", *Theory in Biosciences*, 131(2), 77-84.

25.08.2015

---

[1] published based on work conducted under the scope of this thesis